Multiscale Understanding of Anion Exchange Membrane Fuel Cells: Mechanisms, Electrocatalysts, Polymers, and Cell Management

Huiyu Lei, Xiaohua Yang, Zhangsen Chen, Diane Rawach, Lei Du, Zhenxing Liang, Dong-Sheng Li, Gaixia Zhang,* Ana C. Tavares,* and Shuhui Sun*

Anion exchange membrane fuel cells (AEMFCs) are among the most promising sustainable electrochemical technologies to help solve energy challenges. Compared to proton exchange membrane fuel cells (PEMFCs), AEMFCs offer a broader choice of catalyst materials and a less corrosive operating environment for the bipolar plates and the membrane. This can lead to potentially lower costs and longer operational life than PEMFCs. These significant advantages have made AEMFCs highly competitive in the future fuel cell market, particularly after advancements in developing non-platinum-group-metal anode electrocatalysts, anion exchange membranes and ionomers, and in understanding the relationships between cell operating conditions and mass transport in AEMFCs. This review aims to compile recent literature to provide a comprehensive understanding of AEMFCs in three key areas: i) the mechanisms of the hydrogen oxidation reaction (HOR) and the oxygen reduction reaction (ORR) in alkaline media; ii) recent advancements in the synthesis routes and structure-property relationships of cutting-edge HOR and ORR electrocatalysts, as well as anion exchange membranes and ionomers; and iii) fuel cell operating conditions, including water management and impact of CO_2. Finally, based on these aspects, the future development and perspectives of AEMFCs are proposed.

1. Introduction

Global concerns over fossil fuels and CO_2 emissions are gaining extensive attention. Hence, sustainable energy conversion and storage systems have been developed to maximize the use of renewable energy. Among these systems, low-temperature fuel cells stand out as a promising technology on account of their inherent high energy efficiency and zero greenhouse gas emission when powered by H_2 generated from renewable sources. Low-temperature fuel cells with solid polymer electrolyte membranes can be classified into two types based on their ionic charge carriers (H^+ or OH^-): i) proton exchange membrane fuel cells (PEMFCs, **Figure 1a**) and ii) anion exchange membrane fuel cells (AEMFCs, Figure 1b).[1]

Over the past few decades, PEMFCs have made significant progress. Toyota FCHV and Honda FCX, which began leasing in December 2002, became the world's first government-certified commercial hydrogen fuel cell vehicles. In 2014, Toyota launched the Mirai as the world's first mass-production commercial FCEV.[1b,2] Nowadays, PEMFCs are widely applied in the application of fuel cell vehicles (FCV), such as Toyota Mirai, Hyundai Nexo, and Xcient heavy-duty trucks, as well as Honda Clarity FCVs.[3] Nevertheless, further development of PEMFCs is hindered by platinum-group metal (PGM) catalysts, which are rare and unevenly distributed on a geological scale. For instance, the total cost of a

H. Lei, Z. Chen, D. Rawach, L. Du, A. C. Tavares, S. Sun
Institut National de la Recherche Scientifique (INRS)
Centre Énergie Matériaux Télécommunications
Varennes, Québec J3×1P7, Canada
E-mail: ana.tavares@inrs.ca; shuhui.sun@inrs.ca

X. Yang, G. Zhang
Department of Electrical Engineering
École de Technologie Supérieure (ÉTS)
Montréal, Québec H3C 1K3, Canada
E-mail: gaixia.zhang@etsmtl.ca

Z. Liang
Key Laboratory on Fuel Cell Technology of Guangdong Province
School of Chemistry and Chemical Engineering
South China University of Technology
Guangzhou 510641, P. R. China

D.-S. Li
College of Materials and Chemical Engineering
Key Laboratory of Inorganic Nonmetallic Crystalline and Energy Conversion Materials
China Three Gorges University
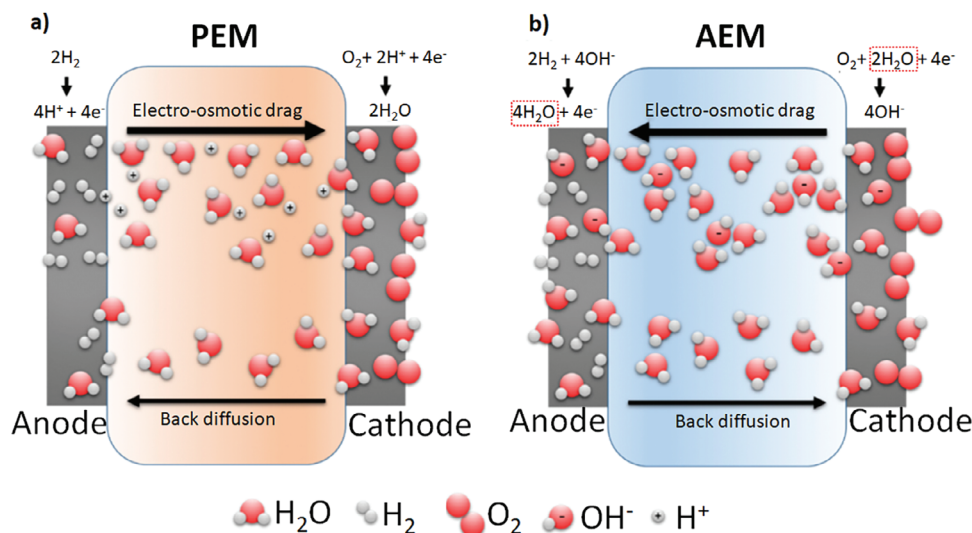Yichang 443002, P. R. China

Figure 1. Schematics of a) PEM fuel cell and b) AEM fuel cell; Reproduced with permission.[1a] Copyright 2018, Elsevier.

typical PEMFC is largely related to the use of the PGM catalyst on the cathode and the expensive proton exchange membrane.[4] Hence, PGM-free catalysts are the ideal alternatives. However, their stability in PEMFCs is yet to meet the standard requirements.[5]
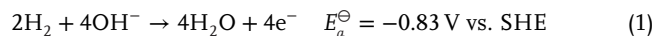
Alkaline fuel cells (AFCs) have a long history dating back to NASA's Apollo missions from 1968 to 1972 and continue to be used in Space Shuttle missions.[6] The recent successful development of highly conductive and durable anion exchange membranes contributes to the renaissance of AEMFCs in the renewable energy community.[7] AEMFCs have several advantages over PEMFCs. Since they operate in an alkaline environment, the overpotential for the oxygen reduction reaction (ORR) in AEM-FCs is lower than that of PEMFCs, which will be discussed in Section 2.[8] This enables a broader range of affordable materials to be used as cathode catalysts. Moreover, the alkaline environment of AEMFCs is less corrosive than the acidic environment of PEMFCs. This allows inexpensive materials, such as stainless steel, to be used as bipolar plates in AEMFCs instead of the expensive high-grade carbon plates or titanium alloys used in the PEMFCs.

Following their potential advantages, the AEMFCs are widely studied for application to aircraft, submarines, and vehicles. Because of these possible applications, the U.S. Department of Energy (DOE) set targets for the AEMFCs from 2020 to 2030.[9] The first goal is to achieve an initial power density of AEMFCs as ≥1.0 W cm^{-2}, under the cell conditions of $T \geq 80$ °C, $P \leq 0.25$ MPa, with a PGM-free membrane assembly electrode, under H$_2$/air. The second goal is to improve the catalyst's durability to obtain a loss in performance of ≤40% after 10 000 square-wave cycles during 0.6–0.95 V under H$_2$/air (CO$_2$-free) with a PGM loading of ≤0.125 mg cm^{-2}. The third goal is achieving membrane durability at H$_2$ crossover of ≤15 mA cm^{-2} after holding the open-circuit voltage for 1000 h under 70% relative humidity (RH), ≥80 °C, and H$_2$/N$_2$.
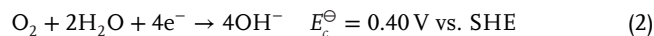
Before discussing the challenges of AEMFCs in achieving the DOE's targets, the general operation of AEMFCs should be presented. As in any type of fuel cell, three main components, namely, an anode, a membrane, and a cathode, are assembled as a membrane assembly electrode (MEA). The electrochemical half-cell and overall reactions in the MEA are listed below:
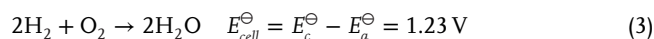
Anode reaction:

$$2H_2 + 4OH^- \rightarrow 4H_2O + 4e^- \quad E_a^\ominus = -0.83 \text{ V vs. SHE} \tag{1}$$

Cathode reaction:

$$O_2 + 2H_2O + 4e^- \rightarrow 4OH^- \quad E_c^\ominus = 0.40 \text{ V vs. SHE} \tag{2}$$

Net reaction:

$$2H_2 + O_2 \rightarrow 2H_2O \quad E_{cell}^\ominus = E_c^\ominus - E_a^\ominus = 1.23 \text{ V} \tag{3}$$

As shown in Figure 1b, at the anode, humidified H$_2$ gas is pumped into the reaction chamber and diffuses through the gas diffusion layer (GDL) to the catalyst layer (CL), where the hydrogen oxidation reaction (HOR) occurs and generates H$_2$O by consuming OH$^-$. Similarly, mass transport of O$_2$ takes place at the cathode chamber to trigger the oxygen reduction reaction (ORR), which consumes O$_2$ and H$_2$O to release OH$^-$ as a product. During the reactions, the H$_2$O and OH$^-$ must be transported through the membrane to maintain the mass and charge balance between the two electrodes. Meanwhile, the electrons (e$^-$) flow through the external circuit, from anode to cathode, to produce electricity.

Developing novel catalysts, particularly anode catalysts, to minimize the HOR overpotential is the first challenge of AEMFC since they are heavily dependent on PGM materials to obtain comparable performances to other fuel cell counterparts. Besides, as for the anion exchange membrane, ionic conductivity, and membrane stability, in both mechanical and chemical aspects, are the main concerning points, particularly when the cell is operated under high temperatures, e.g., 80 °C or above, extreme humidity conditions, and long operation time.[7d] Besides developing new materials, cell operation management is crucial in achieving high-performance AEMFCs. As demonstrated above, water-related mass transport is complicated because four

H_2O are generated at the anode; meanwhile, two H_2O are consumed at the cathode. To reach the optimized water balance inside the cell, managing water transport and content at cell components, including the electrodes and membranes, is essential to ensure the maximum output and stability of AEMFCs. In addition to water management, AEMFCs face other obstacles in cell operation. When the cell is fed with air at the cathode, CO_2 in inlet gas reacts with OH^- to produce CO_3^{2-} and HCO_3^-. This results in a decrease in the conductivity of the anion exchange membrane, which, in turn, lowers the overall power output of the AEMFC.[10]

To overcome these challenges in developing AEMFC, substantial efforts have been devoted in recent years. Some milestone works are highlighted in a timeline in **Figure 2** to illustrate the development of AEMFCs according to their three major aspects: HOR and ORR catalysts, anion exchange polymers (AEPs), including membranes (AEMs) and ionomers (AEIs), and cell system development for water management and CO_2 limitations.

The H_2/O_2 AEMFC, a subcategory of AFC, was first reviewed and proposed as an emerging fuel cell technology by Varcoe and Slade in 2005.[11] The first fully PGM-free AEMFC was reported by Lu et al. in 2008, utilizing a Ni-Cr anode and an Ag cathode, which demonstrated the potential of AEMFC with PGM-free catalysts.[12] As AEMFC technology progressed, AEPs with more stable backbones were developed using the radiation grafting method, and microphase-segregated AEMs were synthesized to enhance membrane properties. This progress in AEP development stimulated further interest in the design of electrocatalysts and the mechanisms of the HOR in alkaline media. During this period, two primary HOR mechanisms were investigated: the H binding energy mechanism and the H and OH bifunctional mechanism.[13] Following advancements in electrocatalysts, researchers also explored water management strategies to further enhance AEMFC performance through various electrode structures, asymmetric ionomers, optimized dew points, and so on.[1a,14] The impact of CO_2 on AEMFC was also explored by quantifying its effects under different operation conditions and membrane types.[15] Since 2020, combining insights from novel membranes and electrocatalysts has led to significant improvements in AEMFC performance. Currently, AEMFC development is focused on low-PGM and PGM-free electrocatalysts that exhibit high activity, stability, and durability, along with the advancement of stable AEPs capable of operating at temperatures of 80 °C and above. There is also a continued focus on in-depth investigations into water management and the effects of CO_2 on AEMFCs.

In the following sections, the recent advancement of AEMFCs will be thoroughly discussed: i) electrode reaction mechanisms in Section 2, ii) HOR and ORR catalysts in Section 3, iii) anion exchange polymers in Section 4, and iv) cell system management in Section 5.

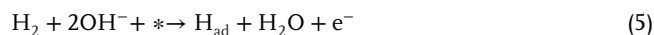## 2. The Reaction Mechanisms of AEMFCs

2.1. Hydrogen Oxidation Reaction Mechanisms in AEMFCs

At the anode of AEMFCs, the primary reaction is HOR, as shown in Equation (1). Two mechanisms describe the HOR in alkaline media: i) the Tafel–Volmer pathway and ii) the Heyrosvsky–Volmer pathway:[35]

Tafel step:

$$H_2 + 2* \rightarrow 2H_{ad} \tag{4}$$

Heyrovsky step:

$$H_2 + 2OH^- + * \rightarrow H_{ad} + H_2O + e^- \tag{5}$$

Volmer step:

$$H_{ad} + OH^- \rightarrow H_2O + e^- + * \tag{6}$$

Generally, hydrogen molecules are adsorbed on the active sites (*) to generate the adsorbed hydrogen (H_{ad} or $H_{2,ad}$), which then reacts with the hydroxide anions (OH^-) to form the water molecules (H_2O). For example, the HOR primarily occurs on the Pt surface via the Tafel-Volmer pathway, for which the rate-determining step (RDS) is the Volmer step.[36] As the reacting media changes from acid to base, the activation energy for the Volmer step increases from 17.1 to 34.0 kJ mol^{-1}.[36a] Hence, in contrast to the acidic environment of PEMFCs, the HOR kinetics of AEMFCs in the alkaline environment are much more sluggish, which leads to a significant cell voltage drop.[37]

The surface composition of the electrode plays a crucial role in determining the activation energy and the mechanism of HOR in alkaline media. The electrode-electrolyte double-layer structure in a monometallic system (e.g., Pt) is depicted in scheme 1 of **Figure 3a**, where the electrode potential is lower than the potential of the double-layer region ($E < E_{dl}$).[8a] First, H_2 molecules are dissociatively adsorbed on the electrode surface to form H_{ad} via the Tafel step. Following that, the OH^- anions carrying negative charge need to be drawn to the plane of the negatively charged Pt surface where the intermediate H_{ad} is covered. This step leads to a voltage penalty, and the reaction requires additional energy to proceed. Consequently, a transition state of $H_{ad}...OH$ cluster is formed before the generation of H_2O molecules.

Aiming to accelerate the sluggish HOR kinetics in alkaline media, several bimetallic or composite catalysts are proposed, which will be discussed in Section 3. For instance, the double-layer structure changes after introducing heteroatoms, as depicted in schemes 2 and 3 of Figure 3a.[8a] Besides, adding a second metal, e.g., Ru, shows the ability to promote hydrogen underpotential deposition (H_{upd}). The AEMFC performance can also be significantly improved by using Pt-based alloys compared to monometallic Pt catalysts.[8a] In the diagram of scheme 2 in Figure 3a, M_1 represents the metal offering the hydrogen adsorption sites, and M_p represents the provider of the H_{upd} sites in the catalysts via the one-electron H_2O reduction reaction (Equation 7). The H_{upd} can stabilize the OH^- anions via the hydrogen bond in a quasi-absorbed state in the outer Helmholtz plane (OHP) to form the $H_{upd}...OH_{q-ad}$ cluster. Finally, the H_{ad} reacts with the quasi-absorbed OH_{q-ad} in the OHP to generate the final product (i.e., H_2O molecules).

$$M_p + H_2O + e^- \rightarrow Mp - H_{upd} + HO^- \tag{7}$$
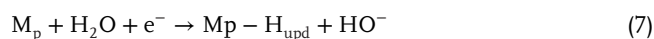
The other solution is alloying Pt with d-block metals in the periodic table, such as Ni and Cu, which are passivated by oxi/hydroxide layers on the surfaces.[38] An example of this
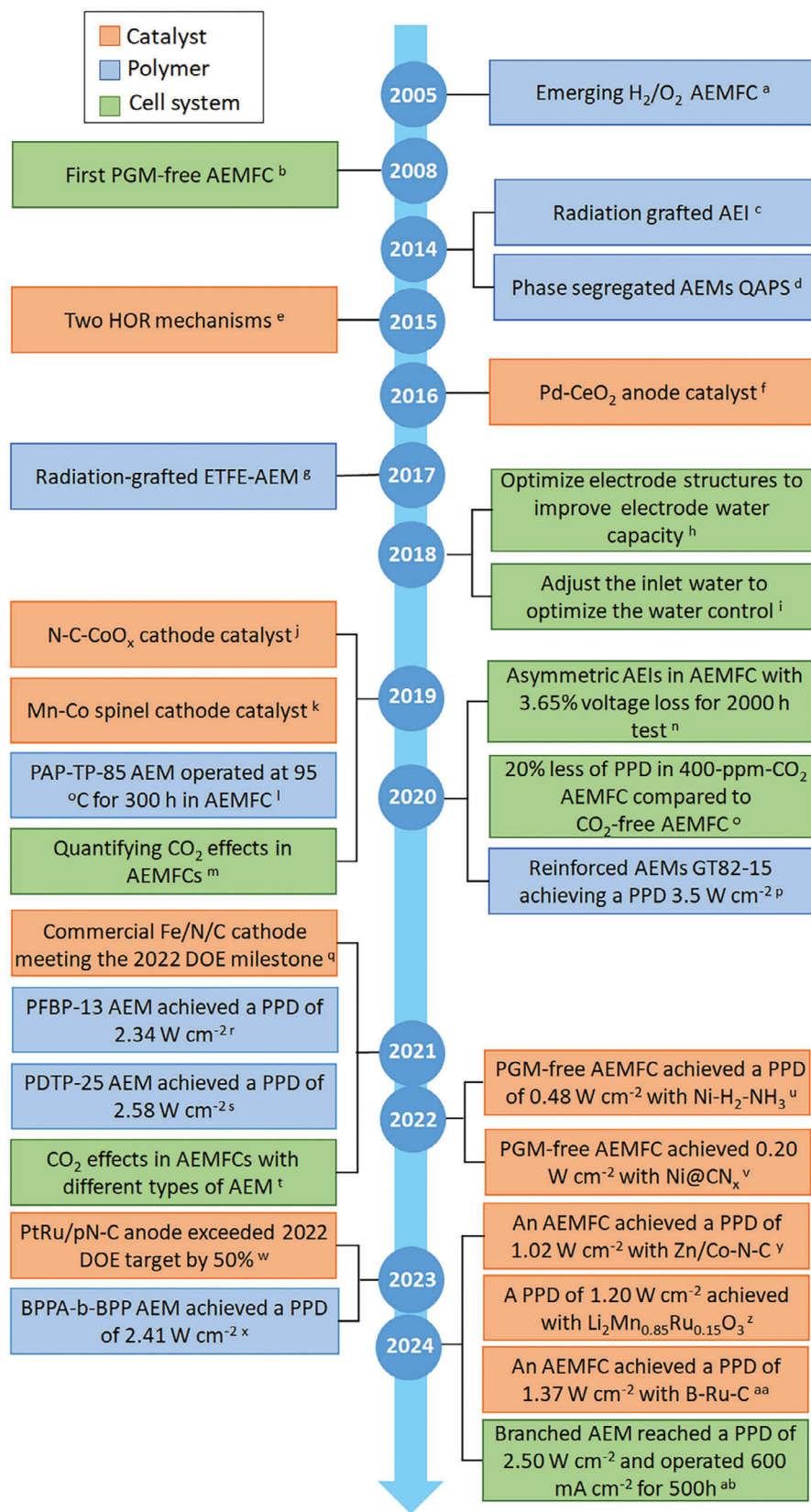
Figure 2. The timeline of the development of anion exchange membrane fuel cells. References: a,[11] b,[12] c,[16] d,[17] e,[13] f,[18] g,[14a] h,[19] i,[1a] j,[20] k,[21,22] m,[15a] n,[14b] o,[15b] p,[23] q,[24] r,[25] s,[26] t,[15c] u,[27] v,[28] w,[29] x,[30] y,[31] z,[32] aa,[33] ab.[34] PPD: peak power density.

**ADVANCED
SCIENCE NEWS**

www.advancedsciencenews.com

**ADVANCED
MATERIALS**

www.advmat.de

Figure 3. a) The schematics of the double-layer structures involved in the HOR in alkaline media; Reproduced with permission.[8a] Copyright 2019, American Chemical Society. b) The reaction descriptors of the catalysis activity of the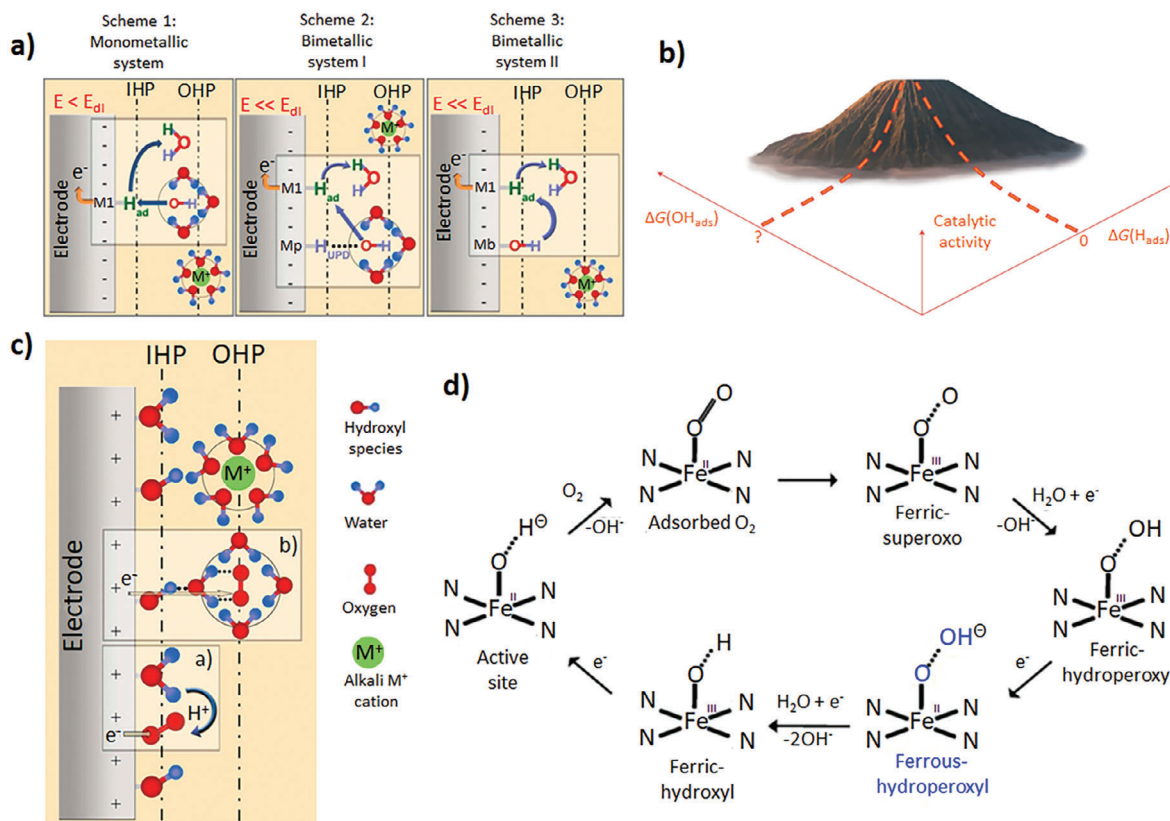 HOR; Reproduced with permission.[39] Copyright 2013, Springer Nature. c) The schematics of the double-layer structures involved in the ORR in alkaline media; Reproduced with permission.[8a] Copyright 2019, American Chemical Society. d) The oxygen reduction reaction routes of the Fe/N/C-based catalysts in alkaline media; Reproduced with permission.[47b] Copyright 2013, American Chemical Society.

kind of double-layer structure is illustrated in scheme 3 of Figure 3a.[8a] On the bimetallic catalyst surface, the reactive OH⁻ anions can specifically be adsorbed on the alloying metal elements (M_b) to form the M_b-OH_{ad} structure, which further reacts with H_{ad} to complete the HOR process.

Although the metal alloy catalysts have been studied for a long time, the enhancement mechanisms of M_p and M_b are still under debate (Figure 3b).[39] In one scenario, it is suggested that the hydrogen binding energy (HBE) to metal, namely $\Delta G(H_{ad})$, is the only descriptor for HOR, and the metal electron states of heteroatoms can be tuned to optimize the HBE.[13,37d,40] A second scenario considers the OH⁻ anions as one of the reactants for which their adsorption energy can be optimized and activated. The HOR reaction kinetics can be improved by adjusting the $\Delta G(OH_{ad})$ through the alloying elements, for instance, the "oxophilic" elements (e.g., Ru or Ni).[38b,39,41]

2.2. Oxygen Reduction Reaction Mechanisms in AEMFCs

As depicted in Equation (2), the cathode reaction of AEMFCs is the ORR, which is the most challenging in PEMFCs due to the requirement of precious metals to achieve acceptable kinetic activities and durability.[42] Fortunately, the existence of a much

broader library of affordable materials as ORR catalysts in alkaline media allows the wider promising options for AEMFC catalysts. This is because as the pH changes from 0 to 14, the equilibrium potential of the O_2 reduction to H_2O/OH⁻ reduces by 0.83 V from 1.23 to 0.40 V versus SHE (i.e., 59 mV pH⁻¹), and the required potential of the first electron transfer step decreases by 0.83 V from 1.53 V to 0.70 V as well.[8,43] These are the thermodynamic reasons for which ORR can occur at lower overpotentials in alkaline media compared to acidic media.

The ORR can occur by both two-plus-two-electrons and four-electrons pathways in alkaline media:

Four electrons pathway:

$$O_2 + 2H_2O + 4e^- \rightarrow 4OH^- \quad E^\ominus = 0.40 \, \text{V vs. SHE} \tag{8}$$

Two-plus-two electrons pathway:

$$O_2 + H_2O + 2e^- \rightarrow HO_2^- + OH^- \quad E^\ominus = -0.076 \, \text{V vs. SHE} \tag{9}$$

$$HO_2^- + H_2O + 2e^- \rightarrow 3OH^- \quad E^\ominus = 0.87 \, \text{V vs. SHE} \tag{10}$$
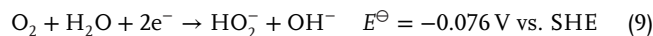
ORR in alkaline electrolytes may involve two types of electron transfer: the inner-sphere electron transfer (ISET) and the outer-sphere electron transfer (OSET).[8b]

**ADVANCED
SCIENCE NEWS**

www.advancedsciencenews.com

**ADVANCED
MATERIALS**

www.advmat.de

The double-layer structure for the ISET mechanism is shown in Figure 3c (insert a). From the schematic, the inner Helmholtz plane (IHP) is occupied by specifically adsorbed hydroxyl species (OH_{ad}), water dipoles, and chemisorbed oxygen molecules, which affect the adsorption configuration of O_2 via the H-bonding network. The OHP is populated by the solvated alkali metal ions. The ISET mechanism involves the direct absorption of O_2 on the electrode surface, such as the oxide-free Pt surface, via a chemical bond in either dissociative or associative forms. This leads to the four-electron pathway and generates OH^- anions directly as shown in Equation 8. In this mechanism, either the initial adsorption of O_2 or the first electron transfer to the absorbed O_2 is widely recognized as the RDS.[8b]

Contrarily, the OSET mechanism is that the reactant (i.e., solvated molecular O_2 cluster) does not directly be chemisorbed on the catalyst surface. Thus, the mechanism enables the two-plus-two-electron pathway involved HO_2^- as the intermediate product (Equation 9 and 10).

The double-layer structure of the OSET mechanism is depicted in Figure 3c (insert b). The solvated O_2 cluster ($O_2 \cdot (H_2O)_n$) interacts with the electrode surface hydroxyl species (OH_{ad}) with hydrogen bonds forming between the H atoms in OH_{ad} and the O atoms in the H_2O molecules. The binding energy of the hydrogen bond is lower than that of the O_2 chemisorption on the catalyst surface and can stabilize the solvated O_2 molecule in the OHP. Afterward, the electron can be transferred (or tunneled) to O_2 to produce a solvated superoxide anion ($O_2^{\bullet-}$), because of the low first-electron-transfer energy in alkaline media. Thereupon, the second electron transfer coupling with proton transfer occurs to produce the product (HO_2^-) via the OSET mechanism. This proton transfer process is regarded as the RDS of the OSET mechanism.

The OSET mechanism only involves the interaction between the $O_2 \cdot (H_2O)_n$ and the OH_{ad}, which causes a certain non-specificity to the electrode material. This non-specificity widens the choices of the catalyst materials from precious metals to non-PGM materials and the metal oxides for ORR in an alkaline medium.[8a,44]

Not only does the electrode specificity change but also the stability of the intermediates, such as hydrogen peroxide (H_2O_2), changes as the electrolyte is switched from acid to base. As the pH increases, the rate of H_2O_2 disproportionation/reduction increases and the maximum rate appears in the pH range of 11–13 due to the deprotonation of H_2O_2 to form the HO_2^- anion in the base catalysis process.[45] With the formation of HO_2^-, the Lewis acid-base transition state structure (M^{n+}-HO_2^-) is formed to increase the disproportionation kinetics.[8a]

Experimental evidence for the OSET mechanism can be obtained by using a rotating ring-disk electrode (RRDE) test to study the hydrogen peroxide oxidation current in the ring during the ORR.[46] Briefly, the interaction between absorbed O_2 and OH^- species (i.e., the OSET mechanism) on the catalyst surface can be proposed by employing the RRDE test. The ring current of H_2O_2 intermediate oxidation can be detected, typically, on the Pt surface in its metal oxide/hydroxide formation region.

Heterogeneous electrocatalysts are one kind of catalyst that can stabilize the high-energy intermediates on the electrode surface and continuously reduce them to HO^-, via the reaction as shown in Equation 10. The ideal electrode catalyst contains metal cation centers where the oxidation states can be adjusted with a lower oxidation state ligand. In other words, the metal cation centers can be chemically oxidized by the intermediate HO_2^-, and then the higher oxidation state of the metal cation centers can be reduced when a certain potential is applied to reverse back to the lower oxidation state.[8a]

Fe/N/C-based materials are the ideal catalysts meeting the abovementioned features as heterogeneous electrochemical catalysts. There is a Fe metal cation center with N coordinating atoms formed as an active moiety in Fe/N/C-based materials, which proved to be one of the most efficient catalysts for ORR in both acidic and alkaline media.[47] Figure 3d represents the ORR routes of the Fe/N/C-based catalysts in alkaline media. It is worth noting that the stability of the hydroperoxyl molecules on the active sites determines the distribution of the products (H_2O or H_2O_2) and the overall electrocatalytic ORR activity. In Fe/N/C-based catalysts, hydrogen peroxide is transformed into HO_2^- under high pH conditions, and it can stably interact with the Fe^{2+} active site via Lewis acid-base interaction.[47b] The interaction ensures that the catalytic cycle can follow the four-electron pathway. Besides, according to the hydrogen peroxide reduction reaction in alkaline media on the Fe/N/C surface, the catalyst kinetically favors the four-electron pathway to generate H_2O.[47b]

3. Electrochemical Catalysts

3.1. Anode Catalysts

The slow kinetics of HOR is one of the major obstacles in the development of AEMFCs.[37c,d,48] Hence, developing new highly active materials for HOR is essential. PGM and their alloys, including Pt,[49] Ru,[13,50] and Pd,[18,51] are studied extensively as HOR catalysts. Besides, PGM-free Ni-based catalysts have also been gaining attention in recent years.[12,52] The HOR catalysts have been summarized in **Table 1** with AEMFC tests done in recent years.

3.1.1. Platinum-Group-Metal-Based HOR Catalysts

Pt is the most widely used and benchmark catalyst for HOR in fuel cells,[53] owing to its excellent electrocatalytic performance, even with a very low catalyst loading (0.05 mg_{Pt} cm^{-2}) in the electrode.[54] However, its performance is insufficient in alkaline media or AEMFCs due to the unique double-layer structure, as discussed in Section 2. To enhance the performance of Pt, the PtRu alloy (0.4 mg_{metal} cm^{-2}) was put forward as a promising anode catalyst by Zhuang and co-workers. A peak power density of 1.00 W cm^{-2} was observed for the PtRu/C anode at a cell temperature of 60 °C, which is higher than that of the Pt/C anode (0.60 W cm^{-2}).[13]

It was suggested that an optimized binding energy of hydrogen to the Pt active sites, instead of the "oxophilic" effect, was the main reason for the enhancement in HOR activity in PtRu/C, which was confirmed by the CO stripping test for Pt/C and PtRu/C.[13] By comparing these two CO stripping curves, the author found that after alloying with Ru, the stripping peaks negatively shift by 0.3 V in the H_2SO_4 electrolyte, demonstrating

Table 1. Performance of typical HOR catalysts in AEMFCs.

HOR Catalyst	HOR Catalyst Loading [mg_{metal} cm^{-2}]	ORR Catalyst	ORR Catalyst Loading [mg_{metal} cm^{-2}]	Membrane and ionomer	Feed gas	T_{Cell} [°C]	T_{DP} of Anode/Cathode [°C]	Back-pressure of Anode/Cathode [MPa]	PPD[a] [W cm^{-2}]	Refs.
PGM-based catalysts for HOR										
PtRu/C	0.40	Pt/C	0.40	aQAPS-S_8-AEM, aQAPS-S_{14} AEI	H_2/O_2	60	60/60	0.10/0.10	1.00	[13]
PtRu/C	0.40	Pt/C	0.40	QAPPT-AEM, QAPPT-AEI	H_2/O_2	80	80/80	0.20/0.20	1.92	[70]
PtRu/C	0.40	Pt/C	0.40	HDPE-AEM, ETFE-AEI	H_2/O_2	80	74/74	0/0	2.55	[68a]
PtRu/pN-C	0.18[b]	Pt/C	0.55[b]	PGT-73, PTG-73-AEI	H_2/O_2	80	71/73	0/0	2.15	[29]
CST-PtRu/NC	0.05[b]	CST-Pt/NC	0.05[b]	GT series AEM and AEI	H_2/O_2	80	70/75	0.10/0.10	1.40	[55]
Pt/C	0.40	Pt/C	0.40	aQAPS-S_8-AEM, aQAPS-S_{14}-AEI	H_2/O_2	60	60/60	0.10/0.10	0.60	[13]
Pt/C	0.40	Pt/C	0.40	QAPPT-AEM, QAPPT-AEI	H_2/O_2	80	80/80	0.10/0.10	1.45	[68b]
Pt/C	0.40	Pt/C	0.40	QAPPT-AEM, QAPPT-AEI	H_2/O_2	80	80/80	0.20/0.20	2.08	[70]
Ru/Meso C	0.10	Pt/C	0.45	QAPPT-AEM, QAPPT-AEI	H_2/O_2	80	80/80	0.10/0.10	1.02	[50b]
Ru_2P/C	0.40	Pt/C	0.40	QAPPT-AEM, QAPPT-AEI	H_2/O_2	80	80/80	0.10/0.10	1.30	[56]
B-Ru/C	0.42	Pt/C	0.48	PiperION-A20, PiperION-A5	H_2/O_2	95.5	89/97	0.25/0.25	1.37	[33]
Ru_7Ni_3/C	0.29	Pt/C	0.40	PAP-TP-85, AP-TP-100	H_2/O_2	95	88/97	0.25/0.25	2.03	[57]
RuCr	0.40	Pt/C	0.40	QAPPT-AEM, QAPPT-AEI	H_2/O_2	80	–	0.20/0.20	1.04	[58]
$(RuCo)_{NC+SAs}$/N-CNT	0.10_{Ru}	Pt/C	0.40	PAP-TP-100, PAP-TP-100	H_2/O_2	80	80/80	0.20/0.20	1.98	[59]
Pd/C-CeO_2	NG	Ag/C	3.0	Not specified AEM and AEI	H_2/Air[c]	73	73/73	0.10/0.30	0.50	[18]
Pd-CeO_2/C	0.25	Pt/C	0.40	ETFE-AEM, ETFE-AEI	H_2/O_2	80	76/76	0/0	2.00	[62]
Pd-CeO_2/C	0.25	Pd/C	0.25	ETFE-AEM, ETFE-AEI	H_2/O_2	80	76/76	0/0	1.30	[62]
Pd-CeO_2/C	0.25	Ag-Co/C	0.75_{Ag}	ETFE-AEM, ETFE-AEI	H_2/O_2	80	76/76	0/0	1.00	[62]
PGM-free catalysts for HOR										
CDN	5.00	Ag	1.00	QAPS-AEM, QAPS-AEI	H_2/O_2	60	60/60	0.13/0.13	0.05	[12]
NiMo/KB	4.00	Pd/C	0.20	A201-AEM, AS4-AEI	H_2/O_2	70	49/49	0.14/0.14	0.12	[52c]
NiCu/KB	4.00	Pd/C	0.20	A201-AEM, AS4-AEI	H_2/O_2	80	80/80	0.14/0.14	0.35	[52d]
Ni@C-500 °C	5.00	Pt/C	0.40	QAPPT-AEM, QAPPT-AEI	H_2/O_2	80	80/80	0.20/0.20	0.16	[52g]
Ni@C-1%	2.40	Pt/C	0.40	QAPPT-AEM, QAPPT-AEI	H_2/O_2	80	80/80	0.20/0.20	0.67	[64b]
Ni@CN_x	15	Pt/C	0.40	QAPPT-AEM, QAPPT-AEI	H_2/O_2	80	80/80	0.20/0.20	0.48	[28]
Ni_4Mo/TiO_2	1.35_{Ni}	Pt/C	0.40	QAPPT-AEM, QAPPT-AEI	H_2/O_2	80	80/80	0.20/0.20	0.52	[65]
NiN_3	4.00	Pt/C	0.40	Alkymer W-25, Alkymer I-250	H_2/O_2	90	90/90	0.20/0.20	0.53	[66f]
Ni-H_2-NH_3	6.00	Pt/C	0.20	PAP-TP-85-AEM, PAP-TP-100-AEI	H_2/O_2	95	88/96	0.25/0.25	0.63	[27]

a) PPD: peak power density; b) in the unit of mg cm^{-2}; c) Air: CO_2-free.

ADVANCED
SCIENCE NEWS
www.advancedsciencenews.com
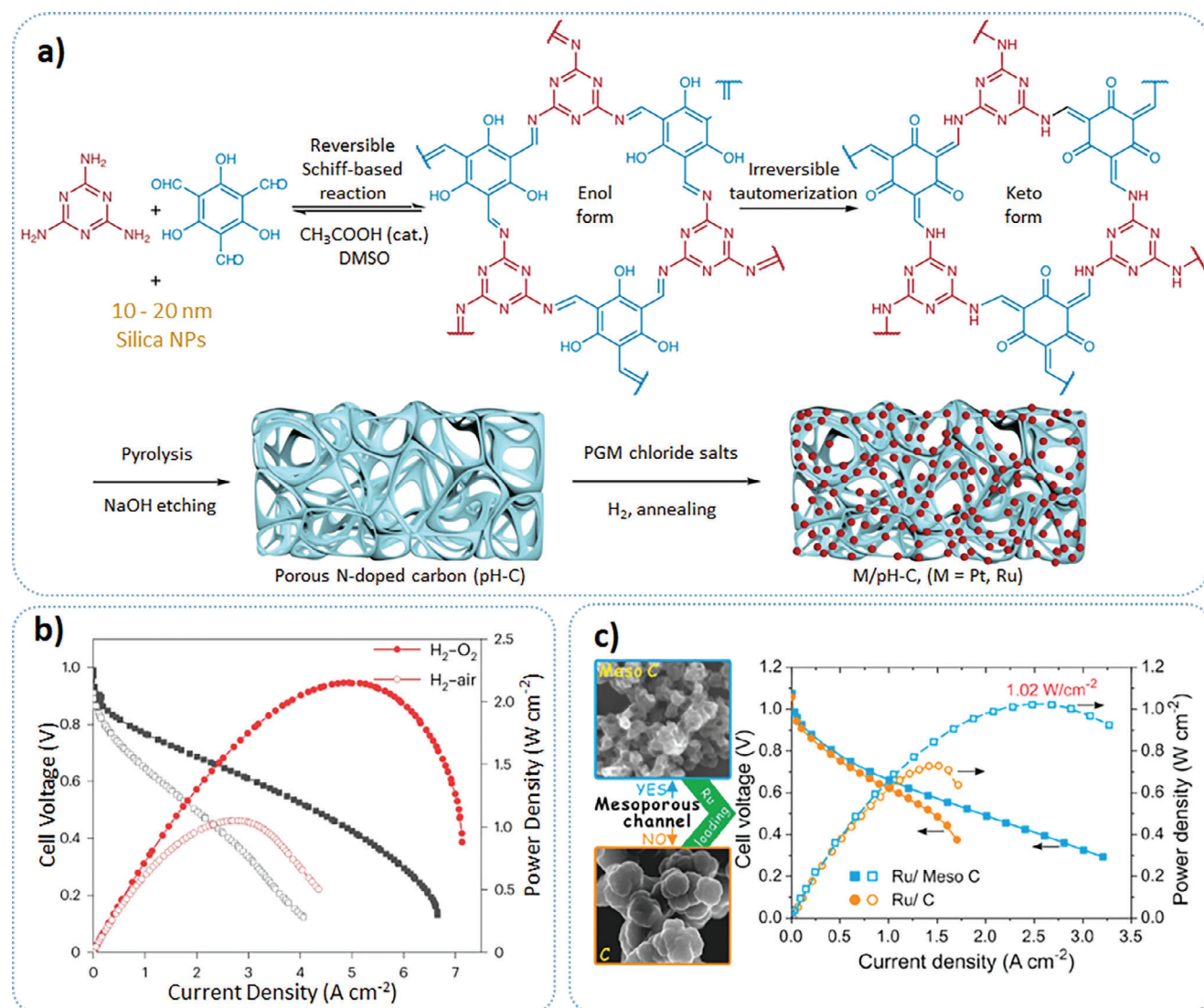
ADVANCED
MATERIALS
www.advmat.de

Figure 4. a) The synthetic procedure of PtRu/pN-C catalyst; Reproduced with permission.[29] Copyright 2023, Springer Nature. b) Fuel cell performances of PtRu/pN-C catalyst as anode catalyst paired with commercial Pt/C cathodes; Test conditions: PtRu/pN-C anode (0.18 mg cm^{-2}) and Pt/C cathode (0.55 mg cm^{-2}); cell temperature at 80 °C; dew points of anode and cathode at 71/73 °C with no backpressure; Reproduced with permission.[29] Copyright 2023, Springer Nature. c) Scanning electron microscope (SEM) images of carbon-supported Ru with/without mesoporous features, and H$_2$/O$_2$ AEMFCs curves with Ru/Meso C and Ru/C as anode catalysts, and 60% Pt/C as a cathode catalyst; Test conditions: Ru/Meso C and Ru/C anode (0.10 mg$_{metal}$ cm^{-2}) and Pt/C cathode (0.45 mg$_{metal}$ cm^{-2}); cell temperature at 80 °C; dew points of anode and cathode both at 80 °C with 0.10 MPa backpressure; Reproduced with permission.[50b] Copyright 2020, Elsevier.

that Ru has a positive effect on forming the OH$_{ad}$ in the acidic media.[13]

However, this effect disappeared when KOH was used as the electrolyte. In the CO stripping tests, after introducing Ru, the stripping peaks were weakened in the potential range of 0–0.35 V vs RHE (reversible hydrogen electrode). The peak at ca. 0.58 V vs RHE was enhanced, indicating that the reactive hydroxyl species (OH$_{ad}$) are more favorably generated on the Pt surface than on the PtRu surface in alkaline media.[13] Further, the hydrogen bonding interaction to the Pt surface was studied in 0.1 mol L^{-1} KOH solution. The cyclic voltammetry (CV) curves showed that the hydrogen underpotential deposition (H$_{UPD}$) peak for PtRu/C was mainly a weak H$_{ad}$ peak, whereas the Pt/C H$_{UPD}$ peak was

a strong H$_{ad}$ peak, which firmly supported the presence of HBE optimization.[13]

The PtRu-based catalyst, with 25 wt.% Pt and 75 wt.% Ru was further studied by Hu and co-workers by loading the PtRu catalyst on nitrogen-doped carbon support (denoted as PtRu/pN-C, **Figure 4a**).[29] The HBEs of Pt and Ru decreased, which was caused by alloying Ru and transferring the charge from Ru to pN-C support, respectively. The decreased HBEs of Pt and Ru were beneficial to the HOR activity by optimizing the binding strength of Pt and Ru with adsorbates. The lower HBE of Ru also turned Ru into active sites, as proposed by the authors. Besides, the nitrogen dopants of pN-C support served as anchors to form the Pt single atoms, which served as optimizing the interfacial

**ADVANCED
SCIENCE NEWS**

www.advancedsciencenews.com

**ADVANCED
MATERIALS**

www.advmat.de

water structure and enhancing the water binding strength confirmed by the in-situ attenuated total reflection surface-enhanced infrared absorption spectroscopy. Thanks to these synergistic effects between PtRu alloy and pN-C support, the PtRu/pN-C anode in H_2/O_2 AEMFCs achieved a peak power density of 1.46 W cm^{-2} paired with commercial Fe/N/C catalyst at the cathode, and a peak power density of 2.15 W cm^{-2} assembled with commercial Pt/C catalyst (Figure 4b).

Adabi et al. also synthesized the PtRu catalyst using the controlled surface tension (CST) method by adding acetone to water to lower the surface tension of the solvent.[55] The reduced surface tension of solvent can minimize the capillary effect, turning out in a higher number of smaller solvent droplets, which can create ultra-small clusters of loading metals. With this method, Pt and Ru were deposited successfully in atomically mixed clusters on N-doped mesoporous carbon, denoted as CST-PtRu/NC. The CST-PtRu/NC was then employed as an anode catalyst in an H_2/O_2 AEMFC with CST-Pt/NC, which was also synthesized with the same CST method to reach a peak power density of 1.40 W cm^{-2} and with Fe/N/C catalyst a 1.20 W cm^{-2}.

Recently, size-controlled Ru nanoparticle catalysts supported by different kinds of carbon materials were investigated for HOR (Figure 4c).[50b] This study used two carbon materials, mesoporous carbon with a ravine-like channel (Meso C) and carbon black (C), as the supports. The Ru/Meso C outperformed Ru/C in exchange current density (9.23 vs 4.06 mA cm^{-2}), specific mass activity (0.54 vs 0.19 mA μg_{Ru}^{-1}) and peak power density (1.02 vs 0.76 W cm^{-2}). The peak power density of the Ru/Meso C catalyst is even comparable to commercial Pt/C (20 wt.%) anode catalyst with the same loading. The differences between these two materials were further studied by using Cu-UPD and CO-stripping experiments. From the experiments, the authors found that the mesoporous structure enables the formation of an inner hydrophobic and an outer hydrophilic surface in the microporous structure. The relatively hydrophobic channels promote H_2 diffusion. Besides, thanks to the space confinement effect, the mesoporous structure prevents the immobilization of Ru nanoparticles and decreases the degree of exposure to air during the synthesis, so a higher proportion of metallic Ru nanoparticles was gained.

Ruthenium phosphides were also adopted as HOR catalysts because of their effective electrocatalytic ability towards hydrogen evolution. Zhao et al. loaded Ru_2P on carbon supports (Ru_2P/C) as an HOR catalyst.[56] The Ru_2P/C anode catalyst reached a peak power density of 1.3 W cm^{-2} in an H_2/O_2 AEMFC at 80 °C. The Ru_2P/C catalyst showed a Pt-like HOR activity in alkaline media because of the optimized hydrogen adsorption energy and the OH binding energy.

Interstitial boron alloyed ruthenium supported on carbon (B-Ru/C) was synthesized by Han et al.[33] The inserting boron atoms into octahedral interstitial sites of Ru, supported by the X-ray diffraction (XRD) and transmission electron microscopy (TEM) data, induced the d-band center of Ru was upshifted to the Fermi level, which was supported by the ultraviolet photoelectron spectroscopy. The HOR intermediates, like OH and H_2O, adsorption abilities were enhanced, which was caused by the electron transfer from Ru to interstitial boron. As a result, the mass activity of B-Ru/C was 13.4-fold higher than that of Ru/C. In the H_2/O_2 AEMFC test, the fuel cell with B-Ru/C as anode catalyst

achieved a peak power density of 1.37 W cm^{-2} at 95.5 °C under a backpressure of 0.25 MPa.

The d-band structure of Ru can be tuned by alloying the other transition metals. Xue et al. showed the alloying of Ru with Ni to construct a Ru_7Ni_3/C HOR catalyst by solvothermal and calcination methods.[57] The HBE of Ru was weakened by alloying Ni and the Ni oxides, which could enhance water adsorption. This bifunctional Ru_7Ni_3/C HOR catalyst showed 3 and 5 times higher mass activity and specific activity in the rotating disk electrode (RDE) test, respectively, when compared with the PtRu/C catalyst. The AEMFC employed with Ru_7Ni_3/C as the anode catalyst reached a power density of 2.03 W cm^{-2} in H_2/O_2 and 1.23 W cm^{-2} in H_2/air (CO_2-free) at 95 °C. The stability test showed that the Ru_7Ni_3/C catalyst maintained the current density of 500 mA cm^{-2} for 100 h with less than 5% voltage loss in H_2/air (CO_2-free) at 80 °C.

Yang et al. reported RuCr nanosheets as HOR catalysts under alkaline electrolytes.[58] The authors optimized the molar ratio between Ru and Cr as 0.05, 0.1, and 0.2. The authors found that when the Ru and Cr molar ratio was 0.1, the RuCr catalyst achieved the highest exchange current density of 0.399 mA cm^{-2} among these three RuCr catalysts. In the H_2/O_2 AEMFC test, the RuCr catalyst with the molar ratio 0.1 achieved a peak power density of 1.04 W cm^{-2} at 80 °C, ascribed to the optimized hydroxide binding energy.

Cui et al. synthesized a dilute RuCo alloy consisting of single Ru and Co atoms supported on N-doped carbon nanotube, designated as $(RuCo)_{NC+SAs}$/N-CNT.[59] The incorporation of Co atoms modulated the electron structure of the Ru host, leading to reduced absorption energies for both H and OH species. These lower absorption energies enhanced the HOR activity and improved resistance to CO. In H_2/O_2 AEMFC tests, the $(RuCO)_{NC+SAs}$/N-CNT HOR catalyst achieved a peak power density of 1.98 W cm^{-2} at 80 °C.

Compounding CeO_2 with Pd is another strategy to improve the HOR performance in AEMFCs using different synthetic methods.[18,51b,d,60] CeO_2 is an oxygen-deficient compound with a fast OH^- saturation and has high oxophilic properties.[18,61] In addition, a catalyst consisting of Pd (10 wt.%) embedded on a mixed support of CeO_2 (50 wt.%) and Vulcan XC-72 carbon (50 wt.%) (denoted as Pd-CeO_2/C) was synthesized by Miller and co-workers.[18] The authors found that when using CeO_2-carbon supports, the Pt-H desorption peak is significantly enhanced and negatively shifted by ca. 90 mV compared to the sole carbon support. The linear sweep voltammetry (LSV) curves also show that when introducing CeO_2 into the carbon support, the HOR activity in alkaline media is drastically improved, as evidenced by the beginning of the diffusion-limited current plateaus at 0.25 V for Pd-CeO_2/C vs 0.5 V for Pd/C.

The reasons for those improvements in HOR activity were investigated regarding Pd distribution and its oxidation state. From TEM images and energy dispersive X-ray analysis (EDX), the author found that Pd mainly accumulated in the ceria regions.[51b] Further, the X-ray absorption spectroscopy analysis showed that the oxidation state of Pd was mostly oxidized in Pd/C-CeO_2 compared to Pd/C, which indicates that the Pd has a strong interaction with CeO_2. Based on the above analysis, the authors proposed a synergy effect and a catalyst structure to account for the activity enhancement, and the corresponding schematic
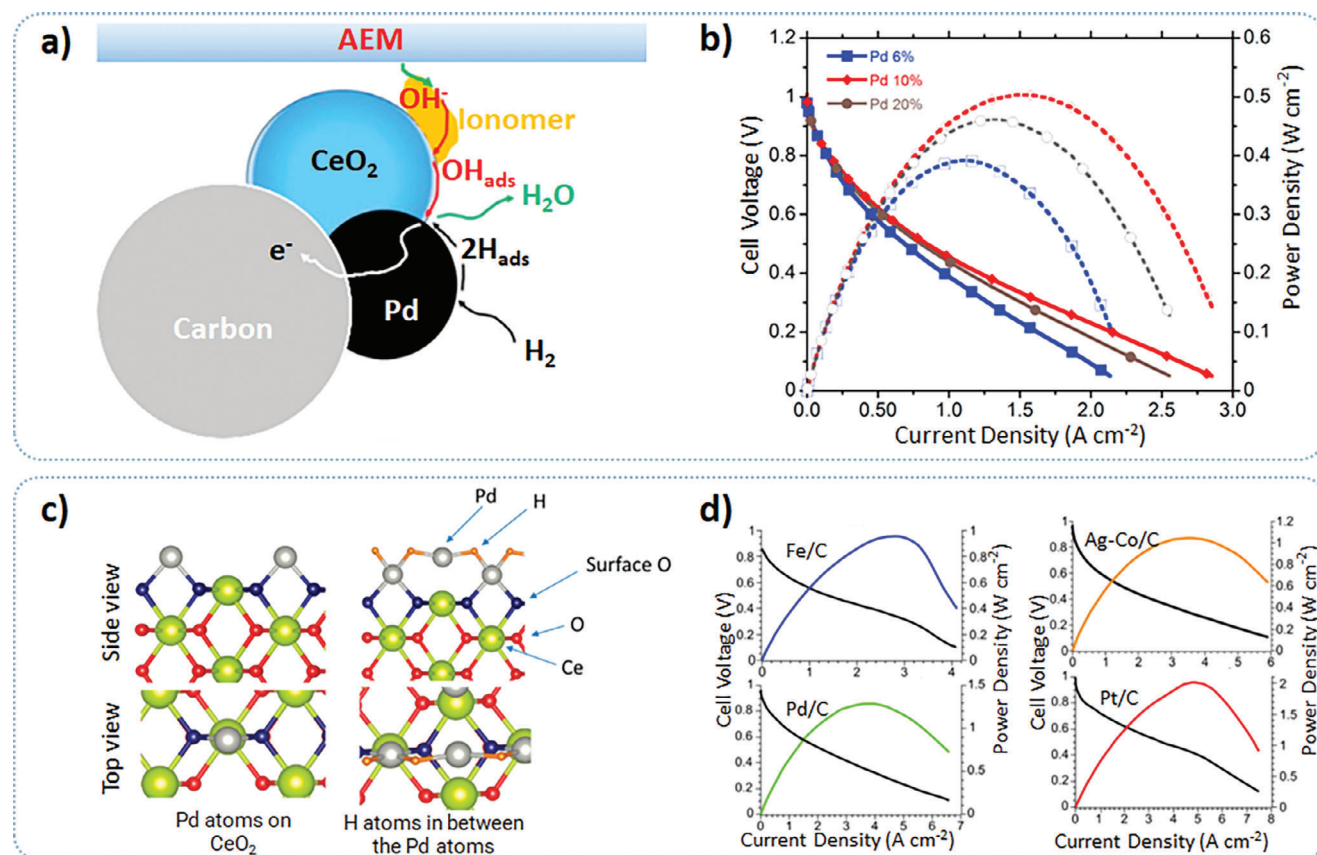
ADVANCED
SCIENCE NEWS

www.advancedsciencenews.com

ADVANCED
MATERIALS

www.advmat.de

Figure 5. a) Schematic representation of Pd/C-CeO$_2$ synergistic effect; Reproduced with permission.[51b] Copyright 2017, Elsevier. b) The H$_2$/air AEMFC polarization and power density curves of Pd/C-CeO$_2$ catalyst with different Pd contents of 6 wt.%, 10 wt.% and 20 wt.%; Test conditions: Pd/C-CeO$_2$ anode (0.15-0.30 mg$_{Pd}$ cm^{-2}) and Ag-based cathode catalyst (3.0 mg$_{Ag}$ cm^{-2}); cell temperature at 73 °C; dew points of anode and cathode both at 73 °C with a backpressure of 0.10 MPa; Reproduced with permission.[51b] Copyright 2017, Elsevier. c) The activity moiety and the adsorption of Pd on the bridge site between the O atoms of the CeO$_2$; Reproduced with permission.[51d] Copyright 2019, American Chemical Society. d) The H$_2$/O$_2$ AEMFC performances with Pd-CeO$_2$/C anode and four different catalysts at cathode. Test conditions: Pd-CeO$_2$/C anode (0.25 mg$_{Pd}$ cm^{-2}) and 1.0, 1.8, 2.5, and 1.0 mg cm^{-2} for Fe/C, Ag-Co/C, Pd/C and Pt/C cathode catalysts, respectively; cell temperature at 80 °C (apart from the Fe/C, which was at 60 °C); dew points of anode and cathode both at 76 °C with no backpressure; Reproduced with permission.[62] Copyright 2020, American Chemical Society.

illustration is shown in **Figure 5a**. This unique structure can weaken the Pd-H$_{ad}$ bonds and assist in supplying OH$_{ad}$ from oxophilic CeO$_2$ to the Pd-H$_{ad}$, thus accelerating the HOR kinetic rate during catalysis.

Then, AEMFC tests (Figure 5b) using Pd/C-CeO$_2$ catalysts with various Pd contents from 6 wt.% to 20 wt.% were carried out at 73 °C with dry H$_2$ and purified air (ca. 10 ppm CO$_2$) as reactants. The best fuel cell performance with a peak power density of 0.50 W cm^{-2} was achieved for the Pd/C-CeO$_2$ catalyst with 10 wt.% Pd. This was attributed to a maximum coverage of CeO$_2$ by Pd. When the Pd content is increased to 20 wt.%, the exceeding Pd was located on carbon nanoparticles and did not contribute to the enhanced activity since they are in the form of Pd/C.[51b] The stability of the Pd/C-CeO$_2$ catalyst was also studied by identical-location TEM, and the results showed that the strong interaction between Pd and CeO$_2$ suppressed the aggregation of Pd nanoparticles. The Pd/C-CeO$_2$ anode catalyst was coupled with a PdCu/C cathode catalyst in a Pt-free catalyst H$_2$/O$_2$ AEMFC that reached a peak power density of 1.00 W cm^{-2}.[51b]

Recently, the same research group of Miller and co-workers developed an atom-scale dispersed Pd-CeO$_2$/C catalyst by replacing

the Ce(NO$_3$)$_3$·6H$_2$O with the novel organometallic cerium-based cerium(IV) tetrakis(decyloxide) as the Ce precursor.[51d] Through density functional theory (DFT) calculations, the authors proposed a model with Pd atoms deposited on the CeO$_2$ (110) surface (Figure 5c). As shown in the model, Pd is bonded on the CeO$_2$ (110) surface in a bridge configuration through surface oxygen. An H atom as reactant adsorbed on the catalyst surface to two CeO$_2$-bonded Pd atoms in a bridge configuration. The calculated HBE changed from −0.80 eV on Pd (111) to -0.46 eV on the Pd-CeO$_2$ (110) surface. In H$_2$/O$_2$ AEMFC tests, the optimized Pd-CeO$_2$ interface catalyst (Pd-CeO$_2$/C) obtained a maximum power density of up to 1.40 W cm^{-2} with the same loading (0.25 mg$_{Pd}$ cm^{-2}) as the Pd/C-CeO$_2$ catalyst. Further, compared to Pd/C-CeO$_2$, in AEMFC tests, the Pd-CeO$_2$/C catalyst showed higher current density at the electro-kinetic region between 0.90 and 0.85 V and lower ohmic and mass transport losses, which implied that an enhanced catalyst-ionomer dispersion within the catalyst layer was fabricated because of the atom-scale dispersed Pd-CeO$_2$. This conclusion was also supported by the lower ohmic resistance of an MEA containing the Pd-CeO$_2$/C compared to that of Pd/C-CeO$_2$.

**ADVANCED
SCIENCE NEWS**

www.advancedsciencenews.com

**ADVANCED
MATERIALS**

www.advmat.de

Miller et al. further investigated the Pd-CeO$_2$/C as anode catalyst paired with Fe/C, Ag-Co/C, Pd/C, and Fe/C as cathodes in AEMFCs (Figure 5d).[62] With Pd-CeO$_2$/C anode, the H$_2$/O$_2$ AEMFC attained a peak power density of 0.96 W cm^{-2} with Fe/C cathode catalyst at 60 °C, while peak power densities of 1.00, 1.30, and 2.00 W cm^{-2} with Ag-Co/C, Pd/C, and Pt/C cathode catalysts, respectively, at 80 °C were reached.

Dekel and co-workers synthesized n-CeO$_x$-Pd/C HOR catalysts with different Ce/Pd bulk atomic ratios (n) of 0.24, 0.38, and 0.59 by using a deposition method based on controlled surface reactions (CSR).[60d] After analyzing the scanning transmission electron microscope (STEM) data, the authors found that the average percentage of interfacial contact area between CeO$_x$ and Pd reaches a maximum of 20.8% in the 0.38-CeO$_x$-Pd/C catalyst. The CV and CO-stripping tests evidenced the relationship between higher contact area and weaker Pd-H interaction. Thanks to the decoration of Pd nanoparticles on CeO$_x$, 0.38-CeO$_x$-Pd/C shows a HOR half-wave potential of 75 mV in 0.1 mol L^{-1} KOH, which is 20 mV lower than that of Pd/C (95 mV) and the lowest among the other three n-CeO$_x$-Pd/C HOR catalysts. The HOR-specific exchange current ($I_{0,m}$) of 0.38-CeO$_x$-Pd/C is 51.5 mA mg$_{Pd}^{-1}$, the highest $I_{0,m}$ among all the previously reported Pd-CeO$_2$ catalysts.[18,51b,d,60a,b] The H$_2$/O$_2$ AEMFC using the 0.38-CeO$_x$-Pd/C as the anode catalyst displayed a peak power density of 1.17 W cm^{-2} mg$_{Pd}^{-1}$ at 60 °C, and was tested at a constant current density of 200 mA cm^{-2} for 24 h with a stable voltage output.[60d]

3.1.2. Platinum-Group-Metal-Free HOR Catalysts

A PGM-free AEMFC having a Cr-decorated Ni (CND) anode catalyst was first fabricated in 2008 by Zhuang's group.[12] The H$_2$/O$_2$ AEMFC, employed with CND as the anode and Ag as the cathode catalysts, attained a peak power density of 50 mW cm^{-2} at 60 °C.[12] DFT calculations showed that the impacts of H and O adsorption on the local density of states (LDOS) for the Ni(111) surface were found to be different. The H adsorption altered almost only the bottom of the *sp*-band, and the O adsorption predominantly changed the *d*-band of the Ni(111) surface.[12] The surface electronic properties of Ni can be tuned by CrO and the changes of LDOS. The density of states at the Fermi level of the *d*-band of Ni(111) decreased, but the bottom part of the *sp*-band remained mostly unaffected. This resulted in a notable weakening of the Ni-O bond but had little impact on the Ni-H bond, supported by the peak temperature of O$_{ad}$ desorption on CND, which was negatively shifted by 130 °C compared to the bare Ni catalyst.[12]

Inspired by this advanced CND catalyst, a series of Ni-based HOR catalysts using other elements were studied,[63] including Ni-W,[52a] Ni-Mo,[52c] and Ni-Cu.[52d] Atanassov's group studied the Ni-Cu nanoparticles supported on Ketjenblack EC-600JD (denoted as NiCu/KB) as the HOR catalyst for the AEMFC.[52d] The NiCu/KB had an atomic ratio of 95:5 for Ni to Cu with alloy features, constituting a bifunctional catalyst surface for HOR. Ni was considered the active site for H$_{ad}$ adsorption, and Cu was a base metal used to form the passivation layer for the adsorption of the OH species. Nano- and micro-X-ray computed tomography (CT) studies suggested the NiCu surface was isostructural with *β*-Ni(OH)$_2$. Their hydrophobicity improved the water distribution in the catalyst layer. The AEMFC data showed that the NiCu/KB achieved a peak power density of ca. 0.35 W cm^{-2} at 80 °C.[52d]

Ni-C core-shell structured HOR catalysts are the emerging HOR catalysts for AEMFCs that optimize the binding energy of Ni and protect the Ni core with a carbon shell.[28,52g,64] Gao et al. synthesized Ni@C catalyst via a vacuum pyrolysis method.[52g] The authors optimized the pyrolysis temperature and tested the series of catalysts in AEMFCs. A trade-off between the activity and stability was achieved with a Ni@C catalyst using a pyrolysis temperature of 500 °C (Ni@C-500 °C). The Ni@C-500 °C-based AEMFC exhibited a stable performance at 0.7 V for 120 h at 70 °C (**Figure 6**a). The highest power density achieved was 0.16 W cm^{-2} at 80 °C under a backpressure of 0.20 MPa.[52g] The origin of this enhanced stability was ascribed to the carbon shell's high graphitization degree, which protects the Ni-core from oxidation.

A similar Ni@C structure was synthesized by Ren et al. with H$_2$ etching the carbon shell to obtain the Ni-based HOR catalyst.[64b] The Ni@C catalysts were pyrolyzed in H$_2$/Ar atmosphere with a series of H$_2$ concentrations of 1%, 2%, and 3%. The authors found that the proper H$_2$ concentration (1%) during pyrolysis made the as-synthesized catalyst, denoted as Ni@C-1%, with the lowest HBE, smallest particle size, and lowest graphitization degree of the carbon shell among the H$_2$-treated Ni@C catalysts. Since the lowest HBE of Ni@C-1% and best HOR activity during the RDE test, H$_2$/O$_2$ AEFMC assembled with Ni@C-1% as anode catalyst was tested with Pt/C cathode to achieve a peak power density of 0.67 W cm^{-2}.

Recently, Gao et al. synthesized Ni core with a nitrogen-doped carbon shell structure catalyst (Ni@CN$_x$), and the CN$_x$ shell was ca. 2 nm confirmed by electron energy loss spectroscopy line profile.[28] The nitrogen-doped carbon shell served as the protection layer against the nickel passivation under high polarization potential compared to Ni NPs and lowered the HBE to Ni to be closer to the optimal value for HOR. Because of these two positive effects introduced by the nitrogen-doped carbon shell, the peak power density of AEMFC using Ni@CN$_x$ anode catalyst achieved 0.48 W cm^{-2} paired with Pt/C cathode while Ni nanoparticles catalyst cathode was 0.13 W cm^{-2}, and 0.21 W cm^{-2} with MnCo$_2$O$_4$/C cathode, at 80 °C under backpressure of 0.20 MPa with H$_2$ and O$_2$ as feed gases at anode and cathode respectively. The Ni@CN$_x$ also remained stable current density at a constant voltage of 0.6 V for 20 h. In the CO tolerance AEMFC test, which added 100 ppm CO into the anode feed gas, the Ni@CN$_x$ catalyst showed more remarkable CO-tolerate ability than the Pt/C catalyst thanks to the nitrogen-doped carbon layer.

Tian et al. synthesized a Ni$_4$Mo alloy supported on TiO$_2$ (Ni$_4$Mo/TiO$_2$).[65] The charge transfer from TiO$_2$ to Ni shifted the Ni *d*-band center to lower energy, which weakened the binding energy of oxygen species. The Ni$_4$Mo/TiO$_2$ showed a higher surface passivation potential for Ni, reaching up to 1.2 V. In H$_2$/O$_2$ AEMFC testing, Ni$_4$Mo/TiO$_2$ as the anode catalyst achieved a peak power density of 0.52 W cm^{-2} at 80 °C and maintained stable operation for nearly 100 h. This stability was attributed to the reduced absorption strength of H, O/OH, and CO species on the Ni$_4$Mo surface, which enhanced its resistance to oxidation.

Transition metal nitrides (TMNs) have emerged as electrocatalysts thanks to their exceptional electrical conductivity, corrosion resistance, and mechanical robustness.[66] And they were
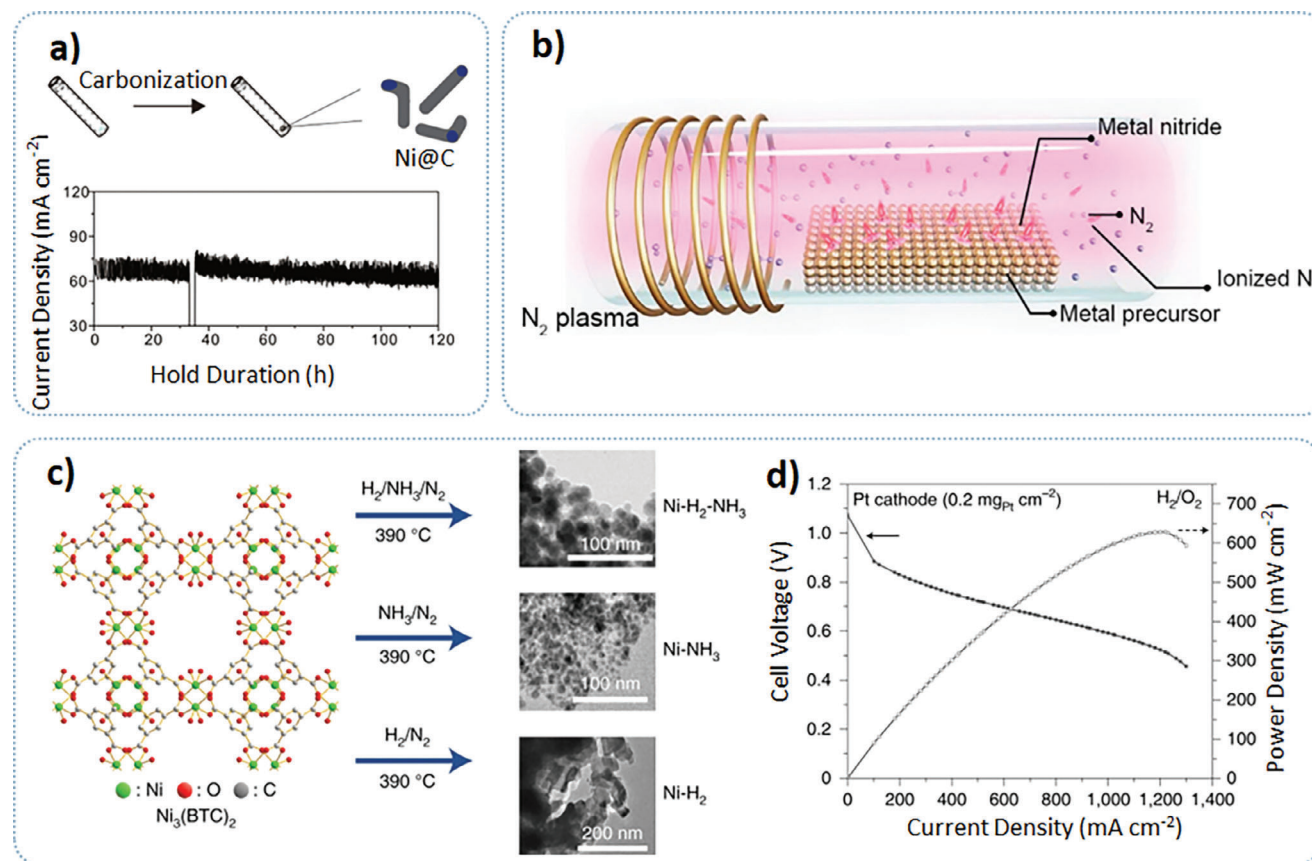
2410106 (11 of 52)

**ADVANCED
SCIENCE NEWS**

www.advancedsciencenews.com

**ADVANCED
MATERIALS**

www.advmat.de

Figure 6. a) Schematic representation of the synthesis of Ni@C-500 °C and the stability test curve; Test conditions: Ni@C-500 °C anode (5.0 mg$_{Ni}$ cm^{-2}) and 60 wt.% Pt/C cathode (0.40 mg$_{Pt}$ cm^{-2}); cell temperature at 70 °C; dew points of H$_2$/O$_2$ both at 70 °C with 0.10 MPa backpressure; stability test was at a constant potential of 0.7 V; Reproduced with permission.[52g] Copyright 2020, American Chemical Society. b) Schematic illustration of plasma-assisted synthesis of metal nitrides; Reproduced with permission.[66f] Copyright 2023, American Chemical Society. c) Schematic illustration of the Ni-based catalysts and the corresponding TEM images; Reproduced with permission.[27] Copyright 2022, Springer Nature. d) The H$_2$/O$_2$ AEMFC performance of Ni-H$_2$-NH$_3$ as anode and Pt/C as cathode; Test conditions: Ni-H$_2$-NH$_3$ anode catalyst (6.0 mg$_{Ni}$ cm^{-2}) and Pt/C cathode catalyst (0.20 mg$_{Pt}$ cm^{-2}); cell temperature at 95 °C; dew points of H$_2$/O$_2$ at 88/96 °C with 0.25 MPa backpressure; Reproduced with permission.[27] Copyright 2022, Springer Nature.

employed as anode and cathode catalysts in AEMFCs.[66e,f] Gao and co-workers used the plasma-enhanced chemical vapor deposition (PECVD) method to synthesize TMNs at room temperature (Figure 6b).[66f] With the PECVD method, nickel nitride (NiN$_3$) was obtained as an HOR catalyst. The as-obtained NiN$_3$ was assembled with Pt/C cathode in an H$_2$/O$_2$ AEMFC, which achieved a peak power density of 0.53 W cm^{-2} at 90 °C. The HOR activity of NiN$_3$(111) originated from the decreased HBE by 90 meV compared to Ni(111). The NiN$_3$ was also paired with zirconium nitride (ZrN), which was synthesized with the same PECVD method, to be demonstrated as the sole TMNs AEMFC, in which the NiN$_3$ and the ZrN were at anode and cathode as catalysts respectively. The sole TMNs AEMFC showed a peak power density of 0.26 W cm^{-2} at 90 °C with H$_2$/O$_2$ feed gases.

Heat-decomposition of metal-organic framework (MOF) was widely used as a preparation method for non-PGM catalysts.[2b,67] Ni et al. heat-decomposed Ni-based MOF Ni$_3$(BTC)$_2$ (BTC, benzene-1,3,5-tricarboxylate) in three different gas atmospheres, i.e., H$_2$/N$_2$, NH$_3$/N$_2$, and H$_2$/NH$_3$/N$_2$ (Figure 6c).[27] During the heat decomposition, NH$_3$ was used to dope nitrogen to regulate

the electronic structure of Ni, while H$_2$ was employed as a reducing agent to obtain metallic Ni nanoparticles. The Ni$_3$(BTC)$_2$ was treated at 390 °C under an H$_2$/NH$_3$/N$_2$ atmosphere, producing an HOR catalyst, denoted as Ni-H$_2$-NH$_3$, with optimal HOR activity resulting from a balance between low HBE and low OHBE. The H$_2$/O$_2$ AEMFC assembled with Ni-H$_2$-NH$_3$ achieved a peak power density of 0.44 W cm^{-2} with a non-PGM CoMn spinel cathode catalyst and a peak power density of 0.56 W cm^{-2} with a Pt/C cathode catalyst at 95 °C under backpressures of 0.25 MPa (Figure 6d).

3.1.3. Stability of Anode Catalysts

The stability of anode catalysts in AEMFCs is typically evaluated using galvanostatic (constant current) or potentiostatic (constant voltage) methods, with tests conducted under H$_2$/O$_2$ or H$_2$/air (CO$_2$-free) conditions at cell temperatures ranging from 60–80 °C. Among PGM-based catalysts, Pt/C is widely employed as HOR catalysts, demonstrating a stable cell performance.[68]

**ADVANCED
SCIENCE NEWS**

www.advancedsciencenews.com

**ADVANCED
MATERIALS**

www.advmat.de

Ni-based catalysts are the most extensively studied low-PGM and PGM-free HOR catalysts, exhibiting acceptable stability in AEMFCs.[28,52c,g,57,64b,65] Metal nitrides and metallic glasses have emerged as promising, stable HOR catalysts in AEMFCs.[66f,69]

Pt/C serves as the benchmark for anode catalyst stability in AEMFCs. Wang et al. reported that Pt/C maintained stable performance at a current density of 600 mA cm^{-2} at 70 °C in the H$_2$/air (CO$_2$-free) AEMFC for over 440 h, with a 7% voltage degradation (from initial 0.70V to 0.67 V).[68a] Similarly, Peng et al. demonstrated Pt/C stability as a HOR catalyst in a H$_2$/air (CO$_2$-free) AEMFC for 120 h at a constant current density of 200 mA cm^{-2} at 80 °C, where the voltage remained at 0.62 V, showing only a 62 mV of voltage decline within the first 80 h.[68b]

Ni-based catalysts, prominent among low-PGM and PGM-free options, have also shown robust stability. For example, in an H$_2$/air (CO$_2$-free) AEMFC, a Ru$_7$Ni$_3$/C HOR catalyst maintained less than 5% voltage loss after 100 hours at 500 mA cm^{-2} and 80 °C in H$_2$/air (CO$_2$-free).[57] NiMo/KB showed stability at a constant voltage of 0.7 V for 120 hours at 60 °C in H$_2$/O$_2$ with a slow current decline beginning after 80 h.[52c] To enhance the oxidation resistance, Gao et al. developed a Ni-core carbon-shell catalyst (Ni@C-500 °C) that demonstrated stable performance at 0.7 V for 120 hours at 70 °C in an H$_2$/O$_2$ AEMFC.[52g] A similar Ni@C structure, with 1% H$_2$ etching (Ni-1%), operated for 100 h at a constant current density of 200 mA cm^{-2} at 80 °C with a voltage loss of 16.2% in the H$_2$/air (CO$_2$-free) AEMFC stability test.[64b] Further, a Ni-core catalyst with an N-doped carbon shell (Ni@CNx) demonstrated a stable operation at a constant voltage of 0.6 V with a current density of ca. 600 mA cm^{-2} for 20 h at 80 °C in an H$_2$/O$_2$ AEMFC.[28]

A recent development by Tian et al. involved a NiMo alloy supported on TiO$_2$ (Ni$_4$Mo/TiO$_2$), showing strong metal-support interaction and enhanced anti-oxidation properties of Ni$_4$Mo.[65] This catalyst demonstrated a stable operation for 100 h at a constant current density of 400 mA cm^{-2} at 80 °C in an H$_2$/O$_2$ AEMFC, maintaining a cell voltage above 0.65 V for the first 80 h. Ni nitrides (Ni$_3$N) were adopted as HOR catalysts in H$_2$/O$_2$ AEMFCs, showing a negligible voltage decay at a current density of 100 mA cm^{-2} for 25 h.[66f]

3.1.4. Summary and Outlook of Anode Catalysts

Anode catalysts for AEMFCs can be broadly categorized into two categories: PGM-based and PGM-free. PGM-based anode catalysts, particularly those based on Pt, Ru, and Pd, are the most extensively studied for AEMFCs due to the high HOR activity of Pt and the oxophilic capacity of Ru. Pd-based catalysts, especially those combined with CeO$_2$, exhibit excellent HOR activity and improved kinetics. While PGM-based catalysts achieve high performance, demonstrating peak power densities of 2.00 W cm^{-2} or higher under H$_2$/O$_2$ and long operation times of up to 440 h in H$_2$/air (CO$_2$-free) AEMFCs, the high cost of PGM materials drives the need for alternative PGM-free options.

PGM-free anode catalysts, primarily based on Ni, use abundant and cost-effective elements as precursors, significantly reducing the overall cost of AEMFCs. These catalysts have been developed in various forms, including Ni nanoparticles, alloys, carbides, and MOF-derived carbons. However, even the

most advanced PGM-free HOR catalyst tested at 95 °C—higher than the typical operating temperature range of most AEMFCs (60–80 °C)—achieved only a peak power density of 0.63 W cm^{-2} in the H$_2$/O$_2$ AEMFCs. Improving the HOR activity of Ni-based catalysts is essential for their broader application in AEMFCs. Nevertheless, Ni-based HOR catalysts have high stability, often maintaining performance for 100 hours, likely due to a passivation layer formed at oxidation potentials around 0.3 V vs RHE.[65]

Various methods have been used to prepare HOR catalysts, including precursor impregnation followed by H$_2$ reduction,[29,52c,d,55,59,64b] heat-decomposition method,[27] template-assisted heat-decomposition method,[50b] oleylamine method,[56,57] wet reduction method,[12,18,28,33,65] metal vapor synthesis,[62] vacuum pyrolysis method,[52g] and plasma-assisted synthesis.[66f] The heat-decomposition method is particularly important for synthesizing atomically dispersed electrocatalysts, while the wet reduction method is also frequently employed.

The development of hybrid catalysts with low-PGM content offers a promising approach to enhance HOR activity and stability. These catalysts can improve HOR activity by lowering the d-band center of non-PGM metal, thereby optimizing the absorption energy of HOR intermediates.[59] Additionally, metal-support interactions can fine-tune the d-band of the non-PGM metal through the electron transfer from the supports, further enhancing HOR activity.[65] Single-atom catalysts (SACs), which offer high atom utilization, have shown promise in optimizing interfacial water structures and improving HOR kinetics.[29] The effects of SACs and metal clusters on HOR activity and stability are worthy of further investigation. Moreover, gas-phase synthesis methods, including chemical vapor deposition, atomic layer deposition, and molecular layer deposition, are highly desirable for synthesizing HOR catalysts due to their precise control and self-limitation nature.

3.2. Cathode Catalysts

The overpotential of ORR in alkaline media is lower than in acidic media, which is the most significant advantage of AEMFCs over PEMFCs. As a result, earth-abundant PGM-free materials can be used as ORR catalysts. Currently, the carbon-supported nanoparticle materials,[14a,20,21,71] atomic level dispersed materials,[72] and carbon-based metal-free materials[73] have primarily been studied as Pt-free ORR catalysts in AEMFCs (**Table 2**).

3.2.1. Carbon-Supported Nanoparticle Catalysts

Ag-nanoparticle-supported carbon (Ag/C) is one of the precious metals used for ORR catalysts that helped H$_2$/O$_2$ AEMFCs to attain a power density of 1.10 W cm^{-2}.[14a] When the cathode feed gas was switched to CO$_2$-free air, the peak power density could still reach 0.70 W cm^{-2}.

Palladium (Pd) was also studied as the ORR catalyst in AEMFC to elucidate the oxidative stability of Pd by Abruña and co-workers.[74] A carbon-supported PdH$_x$ nanosheet (PdH$_x$NS) was synthesized and displayed a peak power density of 1.23 W cm^{-2} as a cathode catalyst at 80 °C under a backpressure of 0.20 MPa with H$_2$ and O$_2$ as feed gases at anode and cathode respectively in

Table 2. Performance of typical Pt-free ORR catalysts in AEMFCs.

ORR Catalyst	ORR Catalyst Loading [mg cm^{-2}]	HOR Catalyst	HOR Catalyst Loading [mg$_{metal}$ cm^{-2}]	Membrane and ionomer	Feed gas	T_{Cell} [°C]	T_{DP} of Anode/Cathode [°C]	Back-pressure of Anode/Cathode [MPa]	PPD[a] [W cm^{-2}]	Refs.
Carbon-supported nanoparticle catalysts for ORR										
Ag/C	1.00[b]	PtRu/C	0.60	ETFE-AEM, ETFE-AEI	H$_2$/O$_2$	70	66/66	0/0	1.11	[14a]
PdH$_x$NS	0.40[b]	PtRu/C	0.40	QAPPT-AEM, QAPPT-AEI	H$_2$/O$_2$	80	80/80	0.20/0.20	1.23	[74]
BMOF-Pd$_2$CO	0.04[c]	PtRu/C	0.40	QAPPT-AEM, QAPPT-AEI	H$_2$/O$_2$	80	80/80	0.20/0.20	1.10	[75]
Li$_2$Mn$_{0.85}$Ru$_{0.15}$O$_3$	0.60	PtRu/C	0.40	QAPPT-AEM, QAPPT-AEI	H$_2$/O$_2$	80	–	0.20/0.20	1.20	[32]
CF-VC	2.40	PtRu/C	0.70	LDPE-AEM, ETFE-AEI	H$_2$/O$_2$	70	51/63	0/0	1.35	[71c]
MnCo$_2$O$_4$/C	0.80[d]	PtRu/C	0.40	QAPPT-AEM, QAPPT-AEI	H$_2$/O$_2$	80	80/80	0.10/0.10	1.20	[21]
CoMn$_2$O$_4$/C	0.80[d]	PtRu/C	0.40	QAPPT-AEM, QAPPT-AEI	H$_2$/O$_2$	80	80/80	0.10/0.10	1.10	[21]
MCS	0.58[b]	PtRu/C	0.40	aQAPS-S$_8$-AEM, aQAPS-S$_{14}$-AEI	H$_2$/O$_2$	60	60/60	0.10/0.10	1.10	[71d]
CoMnO$_2$/C	0.60[d]	PtRu/C	0.40	QAPPT-AEM, QAPPT-AEI	H$_2$/O$_2$	80	79/79	0.20/0.20	1.20	[78]
N-C-CoO$_x$	2.40	PtRu/C	0.70	LDPE-AEM, ETFE-AEI	H$_2$/O$_2$	65	–	0.12/0.08	1.05	[20]
α-Mn$_2$O$_3$/Fe$_{0.5}$-NH$_3$	0.30[e]	PtRu/C	0.90	ETFE-AEM, ETFE-AEI	H$_2$/O$_2$	60	–	0/0	0.98	[79]
Atom-level dispersed catalysts for ORR										
Fe-S-Phen/CNT	1.50	Pt/C	0.50	VBTAC-AEM, Commercial I2-AEI	H$_2$/O$_2$	80	80/80	0/0	0.64	[72f]
Fe0.5-dry	0.91	PtRu/C	0.60	HDPE-AEM, ETFE-AEI	H$_2$/O$_2$	80	71/77	0.05/0.10	1.80	[85]
Fe-NMCSs	4.00	Pt/C	0.30	aQAPS-S$_8$-AEM, aQAPS-S$_{14}$-AEI	H$_2$/O$_2$	80	80/80	0.10/0.10	0.51	[72a]
Fe/N/C PMF11904	1.00	PtRu/C	0.60	HDPE-AEM, ETFE-AEI	H$_2$/O$_2$	80	70/75	0.20/0.20	2.05	[24]
FeN-SiCDC-0.5-400-PVP	2.00	Pt/Ru/C	0.80	HMT-PMBI-AEM, HMT-PMBI-AEI	H$_2$/O$_2$	60	56/60	0.20/0.20	0.31	[87]
FeCoNC-MgOAc	0.96	PtRu/C	0.56	LDPE-AEM, Fumatech-AEI	H$_2$/O$_2$	55	55/55	0/0	0.92	[88]
Fe-N-PDC-HA	1.00	PtRu/C	1.00	Xion Pention, Xion Pention	H$_2$/O$_2$	80	71/77	0.10/0.10	1.06	[89]
Fe/N/C_CNT	2.00	Pt/C	0.40	aQAPS-S$_8$-AEM, aQAPS-S$_{14}$-AEI	H$_2$/O$_2$	60	60/60	0.10/0.10	0.45	[72d]
Co-N-CDC/CNT	2.00	PtRu/C	0.60	HMT-PMBI-AEM, HMT-PMBI-AEI	H$_2$/O$_2$	60	60/60	0.20/0.20	0.58	[72j]
HT800-FeP	1.25	PtRu/C	0.71	ETFE-AEM, Not specified AEI	H$_2$/O$_2$	80	75/77	0.10/0.10	0.58	[91d]
Fe$_{0.5}$-NH$_3$	1.50	PtRu/C	0.90	ETFE-AEM, ETFE-AEI	H$_2$/O$_2$	60	–	0/0	1.04	[79]
CNT/PC	2.00	Pt/C	0.50	VBTAC-AEM, Commercial I2-AEI	H$_2$/O$_2$	80	80/80	0/0	0.38	[72c]
BMOF-Zn$_{20}$Co	0.50	PtRu/C	0.40	QAPPT-AEM, QAPPT-AEI	H$_2$/O$_2$	80	80/80	0.20/0.20	1.02	[31]
Carbon-based metal-free catalysts for ORR										
GU	1.00	PtRu/C	0.60	ETFE -AEM, ETFE-AEI	H$_2$/O$_2$	60	50/50	0/0	0.40	[73d]
FU	1.00	PtRu/C	0.60	ETFE-AEM, ETFE-AEI	H$_2$/O$_2$	60	50/50	0/0	0.70	[73d]
NHC	2.00	Pt/C	1.00	FAA-3-AEM, FAA-3-AEI	H$_2$/O$_2$	70	–	–	0.23	[73c]
CNT/HDC-1000	2.00	Pt/C	0.50	VBTAC- AEM, Commercial I2-AEI	H$_2$/O$_2$	50	50/50	0/0	0.22	[73a]

a) PPD: peak power density; b) in the unit of mg$_{metal}$ cm^{-2}; c) in the unit of mg$_{Pd}$ cm^{-2}; d) in the unit of mg$_{metal}$ cm^{-2}; e) in the unit of mg$_{metal\ oxide}$ cm^{-2}.
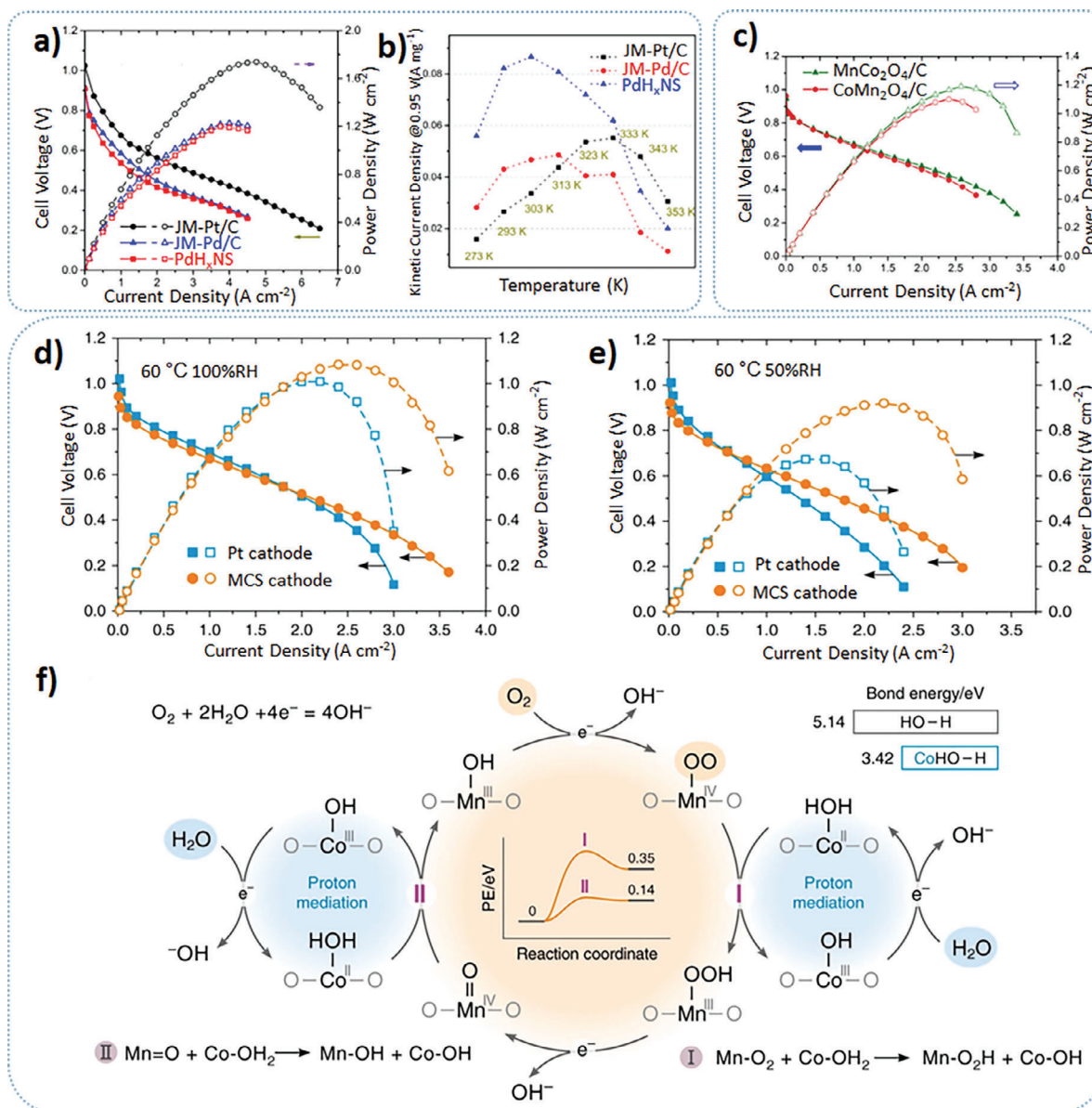
Figure 7. a) H_2/O_2 AEMFC test performances of 60 wt.% Pt/C, Pd/C, and PdH$_x$NS catalysts; Test conditions: PtRu/C anode (0.40 mg$_{PtRu}$ cm^{-2}), and Pt/C, Pd/C, or PdH$_x$NS catalysts (0.40 mg$_{metal}$ cm^{-2}) cathode; cell temperature at 80 °C; dew points of H_2/O_2 both at 80 °C with 0.20 MPa backpressure; Reproduced with permission.[74] Copyright 2022, American Chemical Society. b) Effect of temperature on the ORR mass activities of 60 wt.% Pt/C, Pd/C, and PdH$_x$NS catalysts; Reproduced with permission.[74] Copyright 2022, American Chemical Society. c) Two Co-Mn spinel oxides, MnCo$_2$O$_4$/C and CoMn$_2$O$_4$/C, tested in H_2/O_2 AEMFC; Test conditions: PtRu/C anode (0.40 mg$_{PtRu}$ cm^{-2}) and Co-Mn spinel oxides cathode (0.80 mg cm^{-2}); cell temperature at 80 °C; dew points of H_2/O_2 both at 80 °C with 0.10 MPa backpressure; Reproduced with permission.[21] Copyright 2019, American Chemical Society. d–f) H_2/O_2 AEMFCs test performances of MCS and Pt cathode catalysts under different relative humidity (RH) and schematic illustration: d) 100% RH and e) 60% RH; and f) Schematic representation of the synergistic mechanism of MCS with dissociative reduction of O$_2$ at Mn sites, and Co sites for the proton mediation; Test conditions: PtRu/C anode (0.40 mg$_{PtRu}$ cm^{-2}); MCS/C cathode (0.58 mg$_{metal}$ cm^{-2}) and Pt/C cathode (0.40 mg$_{Pt}$ cm^{-2}); cell temperature at 60 °C; dew points of H_2/O_2 both at 60 °C (100% RH) and 49 °C (60% RH) with 0.10 MPa backpressure; Reproduced under terms of the CC-BY license.[71d] Copyright 2019, The Authors, published by Springer Nature.

AEMFC (**Figure** 7a). However, the peak power density of PdH$_x$NS was inferior to that of Pt/C (1.74 W cm^{-2}) as a cathode catalyst due to the poor oxidative stability of PdH$_x$NS under the conditions of high O$_2$-concentration (100% O$_2$) and high temperature (80 °C), supported by the RDE test in 1 mol L^{-1} KOH electrolyte showing the temperature effects on the ORR performances of three differ-

ent catalysts. The tests showed that PdH$_x$NS and Pd/C reached their maximum at 30 °C (303 K) and 40 °C (313 K), respectively, while at 80 °C (353 K), Pt/C surpassed those of PdH$_x$NS and Pd/C (Figure 7b).

A catalyst of palladium alloyed with cobalt embedded in bimetallic MOF-derived carbon support (BMOF-Pd$_3$Co) was

**ADVANCED
SCIENCE NEWS**

www.advancedsciencenews.com

**ADVANCED
MATERIALS**

www.advmat.de

synthesized by Xu et al. and employed as a cathode catalyst in AEMFC.[75] By synthesizing the BMOF-Pd$_3$Co, two heat-decomposition processes were adopted. The first heat decomposition at 300 °C for 2 h, followed by 400 °C for an extra 2 h. The atomic ratio was also optimized to Pd/Co of 1/3. The BMOF-Pd$_3$Co exhibited a peak power density of 1.10 W cm^{-2} with an ultra-low loading of 0.04 mg$_{Pd}$ cm^{-2} at 80 °C under a backpressure of 0.20 MPa with H$_2$ and O$_2$ as feed gases at anode and cathode respectively in AEMFC.

A layered lithium-rich manganese oxide stabled by controlling the orbital hybridization of *3d* (Mn) and *4d* (Ru) metals was synthesized by Zhong et al.[32] The Li$_2$Mn$_{0.85}$Ru$_{0.15}$O$_3$ ORR catalyst was synthesized with the strategy of changing the metal-O covalency with partial substitution of the *3d* Mn to the more delocalized *4d* Ru to reduce the O *2p* holes surrounding the Mn. The operando XAS test indicated that the active sites were the Mn ions in the Li$_2$Mn$_{0.85}$Ru$_{0.15}$O$_3$. In the half-cell durability test, the Li$_2$Mn$_{0.85}$Ru$_{0.15}$O$_3$ showed a slight voltage loss of 3 mV after 10 000 potential cycles. In the H$_2$/O$_2$ AEMFC test, the fuel cell with Li$_2$Mn$_{0.85}$Ru$_{0.15}$O$_3$ as cathode catalyst reached a peak power density of 1.20 W cm^{-2} at 80 °C under a backpressure of 0.20 MPa.

Additionally, earth-abundant elements, especially Fe and Co, are the other ideal metal-based catalysts for the ORR in AEMFC instead of precious metals. A catalyst based on cobalt ferrite nanoparticles supported on Vulcan XC-72 carbon (CF-VC) was synthesized and characterized by Mustain and co-workers.[71c] The CF-VC showed a half-wave potential of 0.71 V vs RHE in 0.1 mol L^{-1} KOH in RDE measurements. Also, the AEMFC, which employed the CF-VC, achieved peak power densities of 1.66 W cm^{-2} with H$_2$/O$_2$ gases and 0.73 W cm^{-2} under H$_2$/air (CO$_2$-free) feed gases.

Abruña and co-workers proposed Bimetallic Co-Mn catalysts.[21,76] Various combinations of Co-Mn spinel oxide electrocatalysts supported on carbon black were tested with the RDE and AEMFC tests. In the RDE tests, CoMn$_2$O$_4$/C and MnCo$_2$O$_4$ catalysts both showed a similar trend of a half-wave potential shift as the loadings increased.[21] The CoMn$_2$O$_4$/C exhibited a half-wave potential of ca. 0.84 V vs RHE with loadings from 40% to 80%. The MnCo$_2$O$_4$ also displayed a similar half-wave potential with identical loading percentages. The H$_2$/O$_2$ AEMFC test results of CoMn$_2$O$_4$/C and MnCo$_2$O$_4$/C showed peak power densities of 1.10 W cm^{-2} and 1.20 W cm^{-2} respectively (Figure 7c).[21]

Further studies on the bimetallic Co and Mn electrocatalyst were performed by Wang et al., in which the authors found an unusual phenomenon.[71d] In the RDE test, the Mn-Co spinel (MCS) catalyst possessed a half-wave potential of 50 mV inferior to that of the commercial Pt/C. However, in the AEMFC tests under 100% RH, the MCS cathode yielded a peak power density of 1.10 W cm^{-2}, comparable to that of the fuel cell using a Pt cathode (1.00 W cm^{-2}, Figure 7d). When the RH decreased to 50%, the MCS cathode showed much better catalytic performance than the Pt/C cathode, i.e., 0.92 W cm^{-2} and 0.67 W cm^{-2}, respectively (Figure 7e). It is worth noting that in the tests of different RH conditions, the loadings of the anodes (PtRu/C, 0.4 mg$_{metal}$ cm^{-2}) and cathodes (Pt/C, 0.4 mg$_{metal}$ cm^{-2} and MCS, 0.58 mg$_{metal}$ cm^{-2}) were kept constant. After the detailed analysis, the mechanism revealed that H$_2$O was a minority species in the gaseous phase during the AEMFC tests compared to the RDE tests. The MCS catalyst had dual active sites (Mn and Co) to activate O$_2$ and particularly H$_2$O, which made the MCS catalyst less sensitive to the decreasing H$_2$O and proton transfer processes than the Pt/C catalyst.[71d,77] A synergistic mechanism operating with the MCS catalysts was proposed based on the above mechanism and the in-situ attenuated total reflection Fourier transform infrared spectroscopy data (Figure 7f). In detail, the Mn sites promoted the binding and cleaving of O$_2$ molecules to generate Mn-O$_2$. The Co sites enriched H$_2$O on the surface and activated it to generate Co-OH$_2$, which facilitated the proton-coupled electron transfer processes of ORR (Equation 2).

Further, Co and Mn bimetallic oxides were studied by Zhuang and co-workers.[78] A rock-salt-type Co-Mn composite oxides were deposited on Vulcan XC-72 (CoMnO$_2$/C). The CoMnO$_2$/C catalyst reached peak power densities of 1.2 W cm^{-2} in an H$_2$/O$_2$ AEMFC and 0.83 W cm^{-2} in an H$_2$/air (CO$_2$-free) AEMFC. The degradation test of the CoMnO$_2$/C catalyst after the operating of 40 h in AEMFC at a constant current density of 200 mA cm^{-2} was performed. The degradation test results showed that the Co/Mn ratio increased from 0.95 to 1.97, and the valence of Mn changed from +3 to +3.6 on the surface of CoMnO$_2$/C, indicating that Mn dissolved and the regeneration of active sites Mn^{III} were hindered respectively.

The morphology of carbon supports also influences the activity of ORR catalysts in AEMFCs. A 2D planar electrocatalyst with CoO$_x$ embedded with nitrogen-doped graphitic carbon (N-C-CoO$_x$) was synthesized by Mustain's group.[20] The N-C-CoO$_x$ catalysts were synthesized using the direct pyrolysis of a metal-organic complex on a NaCl template (**Figure 8a**). The RDE measurements were performed in O$_2$-saturated 0.1 mol L^{-1} KOH to compare the N-C-CoO$_x$ catalyst with other analogous catalysts. The N-C-CoO$_x$ catalyst exhibited a half-wave potential of 0.84 V vs RHE (Figure 8b). This improved activity was reproduced in the AEMFC performance where the N-C-CoO$_x$ was used as the cathodic catalyst, and the performance reached peak power densities of 1.05 W cm^{-2} under H$_2$/O$_2$ and 0.66 W cm^{-2} under H$_2$/air (CO$_2$-free) at 65 °C (Figure 8c). The catalyst also underwent a stability test at 600 mA cm^{-2} for 100 h under H$_2$/air (CO$_2$-free), with a voltage loss of ca. 15% observed after the test.

Series of MnO$_x$ materials, namely α-MnO$_2$, β-MnO$_2$, δ-MnO$_2$, and α-Mn$_2$O$_3$, supported on Fe/N/C catalysts (denoted as MnO$_x$/Fe$_{0.5}$-NH$_3$) were studied by Jaouen and co-workers.[79] The authors investigated the activity of MnO$_x$ towards hydrogen peroxide reduction reaction (HPRR) and the activity of MnO$_x$/Fe$_{0.5}$-NH$_3$ towards ORR in alkaline electrolytes. Further, the application of MnO$_x$/Fe$_{0.5}$-NH$_3$ in AEMFC as cathode catalysts was also studied. In the HPRR activity test, α-Mn$_2$O$_3$ showed the highest intrinsic HPRR activity in alkaline media among the as-synthesized MnO$_x$ materials, which could compensate for the poor HPRR activity of Fe$_{0.5}$-NH$_3$ catalyst.[80] In RRDE tests, the α-Mn$_2$O$_3$/Fe$_{0.5}$-NH$_3$ catalyst displayed higher selectivity for ORR than the Fe$_{0.5}$-NH$_3$ catalyst. In H$_2$/O$_2$ AEMFC tests at 60 °C, a peak power density with the α-Mn$_2$O$_3$/Fe$_{0.5}$-NH$_3$ catalyst reached 0.98 W cm^{-2}, which was comparable to that with the Fe$_{0.5}$-NH$_3$ catalyst (1.04 W cm^{-2}).

As shown in Section 3.1.2, TMNs have emerged as promising PGM-free catalysts in AEMFCs as anode catalysts. Additionally, TMNs were also employed as ORR catalysts in alkaline media.[81]
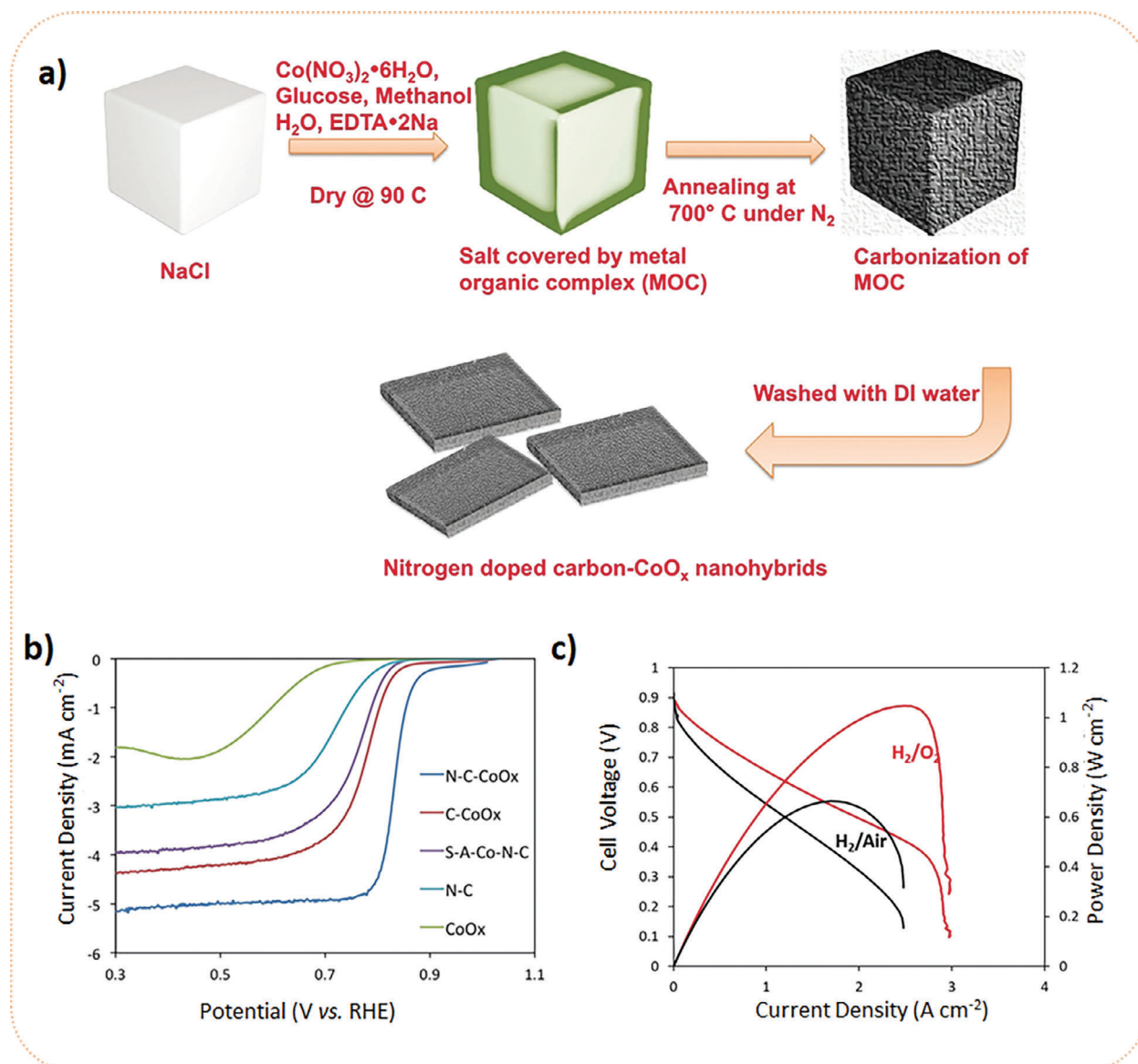
**ADVANCED
SCIENCE NEWS**

www.advancedsciencenews.com

**ADVANCED
MATERIALS**

www.advmat.de

Figure 8. a) Schematic representation of the synthesis of N-C-CoO$_x$ catalyst via direct pyrolysis of the metal-organic complex with the NaCl template; Reproduced under terms of the CC-BY license.[20] Copyright 2019, The Authors, published by John Wiley and Sons. b) ORR polarization curves of different catalysts in 0.1 mol L^{-1} oxygen-saturated KOH; Reproduced under terms of the CC-BY license.[20] Copyright 2019, The Authors, published by John Wiley and Sons. c) Polarization curves and power density of an AEMFCs equipped with a N-C-CoO$_x$ cathode catalyst under H$_2$/O$_2$ and H$_2$/air (CO$_2$-free); Test conditions: PtRu/C anode (0.70 mg cm^{-2}) and N-C-CoO$_x$ cathode (2.40 mg cm^{-2}); cell temperature at 65 °C with backpressure of anode/cathode at 0.08/0.12 MPa; Reproduced under terms of the CC-BY license.[20] Copyright 2019, The Authors, published by John Wiley and Sons.

Zeng et al. synthesized a family of carbon-supported metal nitrides (M$_x$N/C, M = Ti, V, Cr, Mn, Fe, Co, Ni, x = 1 or 3) with a nitride-core-oxide-shell structure.[66e] Among these M$_x$N/C catalysts, Co$_3$N/C exhibited the highest ORR performance in 1 mol L^{-1} KOH with half-wave potential of 0.862 vs RHE. The H$_2$/O$_2$ AEMFC with Co$_3$N/C as a cathode catalyst achieved a peak power density of 0.70 W cm^{-2} at 80 °C. The Co$_3$N/C was also analyzed by the operando synchrotron-based XAS experiments to understand the changes of both the valence of Co and the coordination environment of Co under the potentials among 0.2 to 1.6 V vs RHE. The operando XAS experiment displayed the increased valences of Co from 0.82 to 2.39, yet the decreased Co-N/O bond from 1.5

Å to 1.4 Å when the potential was increased from 1.0 to 1.6 V vs RHE. Nevertheless, those of Co were stable during the potential decrease from 1.0 to 0.2 V vs RHE. The results of operando XAS demonstrated that the oxidizing potential, from 1.0 to 1.6 V vs RHE, destroyed the original structure of Co$_3$N.

3.2.2. Atomic Level Dispersed Catalysts

Atomic-level dispersed materials are in the transition stage from nanoparticle-embedded materials to metal-free materials. Owing to their high metal atom utilization efficiency and

2410106 (17 of 52)

prominent quantum size effects, more and more attention has been gained in this research field recently.[82] Those single-atom catalysts (SACs), which have a metal mass loading usually below 1.5 wt.%, have recently gained much attention for both electrocatalysts and AEMFCs thanks to their high activity originating from the maximum utilization of active sites and high activity site density (SD). Various active sites comprised different central metal atoms and a uniquely coordinated chemical structure.[82a,b,83]

Iron- and nitrogen-co-doped carbon catalysts, denoted as Fe/N/C catalysts, show high intrinsic activity in RDE tests. Generally, a half-wave potential of 0.85 V can be obtained for Fe/N/C catalysts versus RHE in alkaline media, comparable to Pt-based catalysts.[24,84] However, in AEMFC, a cathode PGM-free catalyst loading is 10 folds higher than that of commercial Pt/C to achieve comparable performance. This urges us to develop PGM-free catalysts further to lower the catalyst loading in AEMFCs.

The SiO_2-coating-mediated strategy is a synthetic method to prepare Fe-N-doped single-atom catalysts.[72c,f] This method can enrich the catalyst with Fe-N_x active sites and mitigate the formation of less active Fe, Fe_3C, and FeS particles on carbon nanotube (CNT) during the pyrolysis. As a result, the Fe-Phen/CNT catalyst attained a kinetic current density of 5.5 mA cm^{-2} at 0.9 V in ORR LSV curves in 0.1 mol L^{-1} KOH compared to that of 0.7 mA cm^{-2} for Fe-Phen/CNT_w/o SiO_2 catalyst.[72f] The most active Fe-S-Phen/CNT catalyst exhibited a half-wave potential of 0.91 V versus RHE, a kinetic current density of 11.8 mA cm^{-2} at 0.9 V in 0.1 mol L^{-1} KOH, and a peak power density of 0.64 W cm^{-2} at 80 °C in an H_2/O_2 AEMFC.

Another CNT with FeN_x active sites catalyst was synthesized from $FeCl_3 \cdot 6H_2O$ and adenosine as the carbon and nitrogen sources via a solvothermal process followed by pyrolysis, denoted as Fe/N/C_CNT.[72d] In the LSV tests, the resulting catalyst presented a half-wave potential of 0.93 V versus RHE in alkaline media, comparable to the half-wave potential of Pt/C (0.93 V versus RHE) tested under identical testing conditions. The AEMFC with the prepared material as the cathode catalyst achieved a peak power density of 0.45 W cm^{-2} under H_2/O_2. This was attributed to the high N–doping level of 8% and the dispersion of atomic Fe sites on the walls of the nanotubes.

The states of Fe(II) acetate, a widely used Fe precursor during the syntheses of Fe/N/C catalysts, were proved to change the Fe speciation in Fe/N/C catalysts by Adabi et al.[85] The Fe(II) acetate changed from anhydrous Fe(II) acetate to Fe(III) acetate hydrate after storing in ambient air, confirmed by XRD, Mössbauer spectrum, and XAS. The authors used fresh anhydrous Fe(II) acetate and the aged Fe(III) acetate hydrate to synthesize two catalysts, $Fe_{0.5}$-dry and $Fe_{0.5}$-hydrate, respectively. It was shown that Fe mainly existed as FeN_4 active sites in $Fe_{0.5}$-dry, while Fe particles with few FeN_4 active sites existed in $Fe_{0.5}$-hydrate. The authors suggested that the Fe(II) acetate states were the key reason for the amounts of Fe particles in Fe/N/C catalysts. In H_2/O_2 AEMFC tests, when the current density increased, the inferiority of the current density of $Fe_{0.5}$-hydrate became more pronounced because of the fewer FeN_4 active sites compared to $Fe_{0.5}$-dry. The $Fe_{0.5}$-dry as cathode catalyst in H_2/O_2 AEMFC tests achieved a peak power density of 1.80 W cm^{-2} while 1.10 W cm^{-2} with $Fe_{0.5}$-hydrate.

Mass transport is always challenging when non-PGM catalysts are used at the cathode rather than Pt-based catalysts. Ma-

nipulating the structure of catalysts is a practical way to facilitate mass transport. Fe-N-doped mesoporous carbon microsphere (Fe-NMCSs) catalyst was synthesized via an in-situ replication and polymerization strategy on the Fe_3O_4 microspheres template.[72a] The RDE tests showed a half-wave potential of 0.86 V vs RHE in O_2-saturated 0.1 mol L^{-1} KOH, comparable to the Pt/C catalyst. The high activity of the catalyst was attributed to the Fe species (0.50 at.%), as confirmed by the cyanide ions (CN^-) experiment, in which after adding 50 nM CN^- ions to the electrolyte, the ORR half-wave potential decreased by more than 100 mV. The H_2/O_2 AEMFC tests were conducted at 80 °C, and a peak power density of 0.51 W cm^{-2} was obtained.

Zhang's group synthesized another Fe-N-doped catalyst (denoted as EFGC) via anchoring an iron-EDTA (ethylenediaminetetraacetic acid) complex on graphene followed by acid leaching.[86] The EFGC in the H_2/O_2 AEMFC test at 80 °C yielded a peak power density of 0.33 W cm^{-2}, attributed to the sheet-shaped morphology and the Fe-N_x active sites.

Two strategies were adopted by Adabi et al. to increase the mass transport in the catalyst.[24] The first one was enlarging the average pore size of the catalyst to the mesopore range using silica templates. The second one was decreasing the hydrophilicity of the catalyst by increasing its graphitization level (**Figure 9**a). The as-synthesized Fe/N/C catalyst (PMF11904) had a specific surface area of 550 m^2 g^{-1} and 5–30 nm pore diameters. From the STEM images, Fe was majorly dispersed as single atoms in the PMF11904. In the RRDE tests, the half-wave potential of the as-synthesized Fe/N/C was 0.846 V vs RHE with an electron transfer number of 3.967 and less than 1% H_2O_2 yield in 0.1 mol L^{-1} KOH, which was comparable to the commercial 40 wt.% Pt/C. In H_2/O_2 AEMFC tests, the as-synthesized Fe/N/C catalyst achieved a peak power density of 2.05 W cm^{-2} at 80 °C under 0.20 MPa backpressure (Figure 9b). In H_2/air (CO_2-free) AEMFC tests, PMF11904 reached 1.00 W cm^{-2} at 80 °C under 0.15 MPa backpressure. In the stability test, the PMF11904 catalyst maintained a current density of 600 mA cm^{-2} for 150 h with a voltage decay rate of 0.46 mV h^{-1}. Finally, the PMF11904 catalyst was paired with a low-loading PtRu/C anode (0.125 mgPtRu cm^{-2}) electrode to achieve a peak power density of 1.30 W cm^{-2} at 80 °C with 0.10 MPa under H_2/O_2, which equaled to 10.4 W mg$_{PGM}$$^{-1}$.

Ratso et al. decreased the carbon particle size by optimizing the ball milling conditions to synthesize the 1,10-phenanthroline-and-iron(II) acetate-functionalized silicon carbide-derived carbon catalyst (denoted as FeN-SiCDC-0.5-400-PVP).[87] In this work, the precursors were mixed with ethanol, polyvinylpyrrolidone (PVP), and 20 g of ZrO_2 beads with a diameter of 0.5 mm. Then, the ball milling process was carried out at 400 rpm for 2 h. The size of FeN-SiCDC-0.5-400-PVP decreased from above 1 μm to 200 nm without negatively affecting the BET surface area, which was 865 m^2 g^{-1}. The N content in the prepared catalyst was 4.5 at.% and Fe is mainly presented as FeN_x (92%). FeN-SiCDC-0.5-400-PVP delivered a peak power density of 0.36 W cm^{-2} at 60 °C in an H_2/O_2 AEMFC.

Kisand et al. also used the sacrificed template method.[88] The authors used MgO-based inorganic templates to increase the mesoporosity of the N-doped carbon-based catalyst with automatically dispersed Fe and Co moieties (denoted as FeCoNC-MgOAc, Figure 9c). With the MgO template assisting, the specific surface area (505 m^2 g^{-1}), the total pore volume (0.87 cm^3 g^{-1}), and

ADVANCED
SCIENCE NEWS

www.advancedsciencenews.com

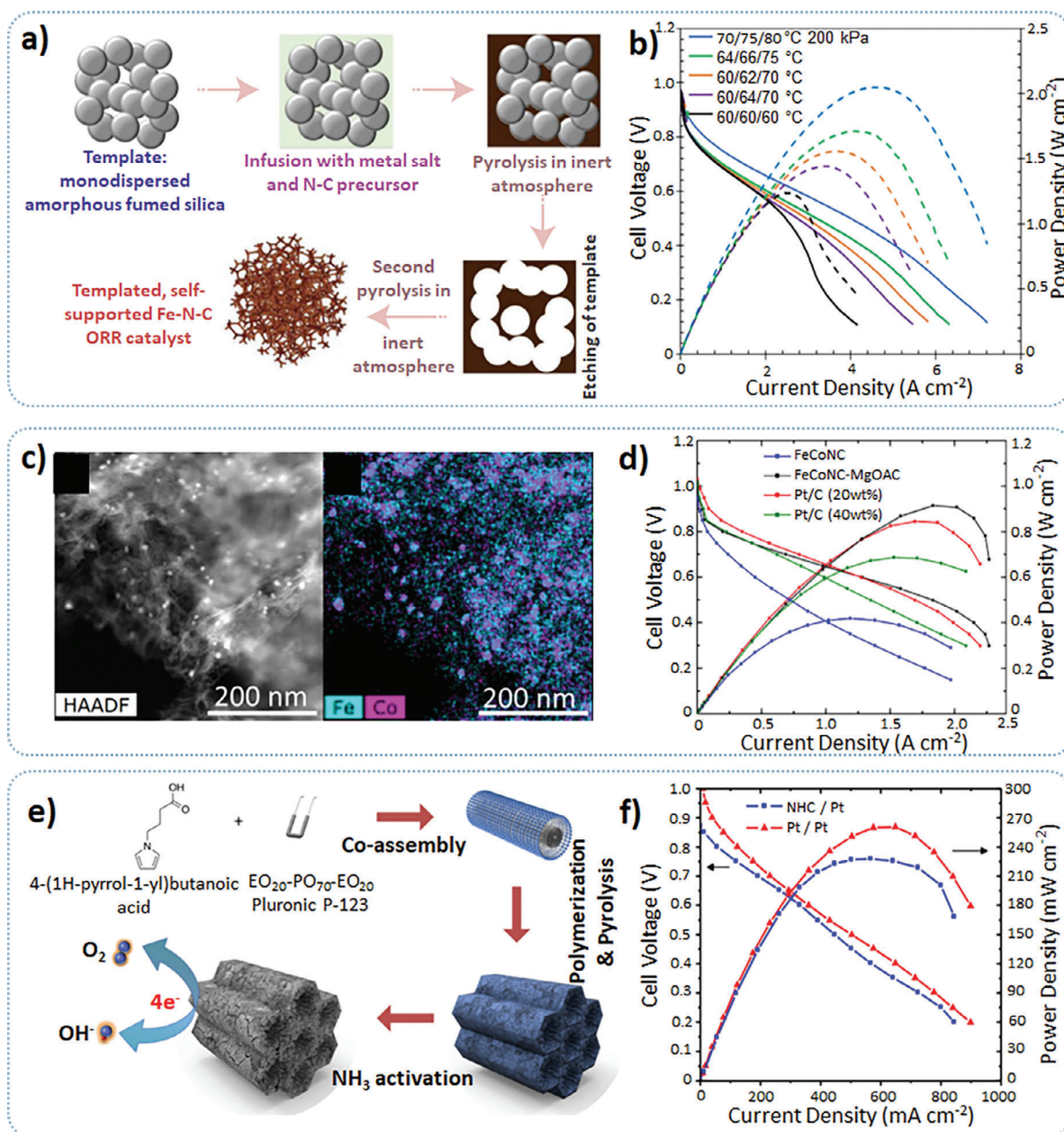**ADVANCED
MATERIALS**

www.advmat.de

Figure 9. a) Synthesis route of commercial mesoporous PMF11904 Fe/N/C catalyst; Reproduced with permission.[24] Copyright 2021, Springer Nature. b) H_2/O_2 AEMFC results with PMF11904 Fe/N/C catalyst; Test conditions: PtRu/C anode (0.60 mg_{PtRu} cm^{-2}) and PMF11904 Fe/N/C catalyst cathode (1.00 mg cm^{-2}); the anode dew point/cathode dew point/cell temperature and back pressure are given in the figure; Reproduced with permission.[24] Copyright 2021, Springer Nature. c) High-angle annular dark field (HAADF) image and energy-dispersive X-ray (EDX) image of FeCoNC-MgOAc; Reproduced with permission.[88] Copyright 2022, American Chemical Society. d) H_2/O_2 AEMFC results of FeCoNC, FeCoNC-MgOAc, and two Pt/C catalysts; Test conditions: PtRu/C anode (0.56 mg_{PtRu} cm^{-2}), FeCoNC and FeCoNC-MgOAc catalyst cathode (0.96 mg cm^{-2}); cell temperature at 55 °C; dew points of H_2/O_2 both at 55 °C with no backpressure; Reproduced with permission.[88] Copyright 2022, American Chemical Society. e) Schematic representation of the synthesis of NHC; Reproduced with permission.[73c] Copyright 2016, Springer Nature. f) H_2/O_2 AEMFC results of NHC as cathode catalyst and of Pt/C as the reference cathode catalyst; Test conditions: Pt/C anode (1.00 mg cm^{-2}) and NHC cathode catalyst (2.00 mg cm^{-2}); cell temperature at 70 °C; Reproduced with permission.[73c] Copyright 2016, Springer Nature.

the micropore volume (0.11 cm^3 g^{-1}) of the FeCoNC were significantly increased compared to the FeCoNC catalyst without the sacrificed MgO template (denoted as FeCoNC, 320 m^2 g^{-1}, 0.81 cm^3 g^{-1}, 0.05 cm^3 g^{-1}, respectively). The FeCoNc-MgOAc achieved a peak power density of 0.92 W cm^{-2}, over twice as high

as the FeCoNC (0.42 W cm^{-2}) (Figure 9d), thanks to the improved mass transport performance and the lower content area-specific resistance.

The hydroxyapatite (HA) was also adopted as a sacrificed template alongside $ZnCl_2$ as a micropore former by Teppor et al.[89]

**ADVANCED
SCIENCE NEWS**

www.advancedsciencenews.com

**ADVANCED
MATERIALS**

www.advmat.de

A Fe/N/C catalyst, Fe-N-PDC-HA, was synthesized with the two pore-formers and renewable peat as a carbon source. The Fe-N-PDC-HA reached a peak power density of 0.84 W cm^{-2} in the H$_2$/O$_2$ AEMFC test at 65 °C, which was almost two-fold of that of the template-free counterpart, thanks to the abundant porous structures in Fe-N-PDC-HA. It was further tested at 80 °C in the H$_2$/O$_2$ AEMFC and reached a peak power density of 1.06 W cm^{-2}.

Porphyrin-like compounds, including porphyrins, phthalocyanines, and corroles, have been adopted as ORR catalysts since 1964 by Jasinski.[90] They were recently studied in the AEMFCs as ORR catalysts.[91] Among them, a series of heat-treated FeP aerogels was studied recently by Elbaz and co-workers in AEMFC as cathode catalysts by varying the pyrolysis temperature in the range of 600 to 1000 °C.[91d] As the heat treatment temperatures increased, the graphitization degrees increased while the nitrogen and iron contents decreased. The optimum balance between them in the FeP catalysts was achieved when the pyrolysis temperature was 800 °C, denoted as HT800-FeP. The H$_2$/O$_2$ AEMFC with HT800-FeP reached a peak power density of 0.58 W cm^{-2} at 80 °C.

Cobalt- and nitrogen-co-doped carbons (Co/N/C) are another type of catalyst widely used in fuel cells.[72j,92] Tammeveski and co-workers developed meso- and microporous cobalt- and nitrogen-doped carbide-derived carbon/ carbon nanotube (Co-N-CDC/CNT) as an ORR catalyst.[72j] The catalyst exhibited a half-wave potential of 0.82 V vs RHE in alkaline media and good durability after 10 000 continuous potential cycles. In H$_2$/O$_2$ AEMFC tests, the Co-N-CDC/CNT catalyst showed a peak power density of 0.58 W cm^{-2} at 60 °C which was attributed to its large mesoporous and microporous network, nitrogen- and cobalt-coordinated species, and the defect-rich nature of the Co-N-CDC/CNT catalyst.[72j,93]

Xu et al. synthesized Zn/Co-N-C with Co-N$_4$ and Zn-N$_4$ local structures as an ORR catalyst.[31] The author synthesized the MOF-derived single-atom catalyst denoted as BMOF-Zn$_{20}$Co, where the ratio of Zn and Co was 20:1. In the operando XAS test of BMOF-Zn$_{20}$Co, it suggested that the primary active site was the Co in the Co-N$_4$ structure. In the half-cell durability test, the BMOF-Zn$_{20}$Co showed an 8.5 mV negative shift of half-wave potential after 50 000 electrochemical cycles. In the H$_2$/O$_2$ AEMFC test, BMOF-Zn$_{20}$Co achieved a peak power density of 1.02 W cm^{-2} with a 0.20 MPa backpressure.

3.2.3. Carbon-Based Metal-Free Catalysts

Carbon-based metal-free materials are promising ORR catalysts in energy conversion and storage devices.[94] These materials also show potential application in AEMFC when provided with controlled porous structures and features from doping with heteroatoms.

Two carbon-based metal-free catalysts were obtained from urea as the nitrogen source and glucose or furfural as the carbon precursors, denoted as GU and FU, respectively.[73d] Both catalysts have a similar amount of nitrogen doping (4.7 at.% for GU and 5.2 at.% for FU) and graphitization degree ($I_D/I_G = 1.01$ for GU and 1.00 for FU) but have different structural features. Compared to GU, FU offers a higher specific surface area, larger pore volume, and more complex pore size distribution. The morphol-

ogy is flaky for GU and rod-like for FU. The rod-like structure of FU facilitates the O$_2$ adsorption and diffusion and, therefore, promotes electron transfer. As a result, the half-wave potential of FU is only 45 mV (0.76 V vs RHE) lower than that of the Pt/C catalyst (0.81 V vs RHE) in the LSV tests in alkaline electrolytes. In the H$_2$/O$_2$ AEMFC test, the different morphologies result in different cell performances, e.g., the peak power density of 0.70 W cm^{-2} is obtained for FU and 0.40 W cm^{-2} for GU at 60 °C.

Ordered mesoporous carbon catalysts are among the most promising ORR catalysts in alkaline media. Moreover, they show high activity and long-term stability towards ORR due to their ordered mesoporous structure providing the interconnected channels and high surface area for the diffusion of electroactive species, as well as the protection of the active sites.[72e,73c,95] A mesoporous and N-doped hierarchical carbon (NHC) catalyst reported by To et al. was synthesized using a triblock copolymer as a template.[73c] Following pyrolysis under an inert atmosphere and NH$_3$ activation processes, the catalyst was found to have a nitrogen content of 3.6 wt.% (Figure 9e). In the RDE test, NHC exhibited a half-wave potential of 0.882 V vs RHE in O$_2$-saturated 0.1 mol L^{-1} KOH. The activity can be attributed to its hierarchical structure and N-heteroatoms. In the H$_2$/O$_2$ AEMFC test, the cell with an NHC cathode attained a peak power density of 0.23 W cm^{-2} at 70 °C, comparable to the cell with a Pt cathode (0.26 W cm^{-2}, Figure 9f).

Carbon materials derived from ionic liquids are another type of metal-free materials. Sang Hoon Joo and co-workers synthesized carbon nanotubes /heteroatom-doped carbon (CNT/HDC) catalysts possessing a core-sheath nanostructure, which was constructed by carbonizing the heteroatom-containing ionic liquids on CNT with silica coating assistant.[73a] Among various prepared catalysts, the most active catalyst of CNT/HDC-1000 with pyrolysis at 1000 °C under N$_2$ atmosphere showed a half-wave potential of 0.82 V vs RHE in the alkaline electrolyte. The MEA prepared with CNT/HDC-1000 cathode catalyst was employed in H$_2$/O$_2$ AEMFCs, generating a peak power density of 0.22 W cm^{-2} at 50 °C.

3.2.4. Stability of Cathode Catalysts

The stability testing methods for cathode catalysts in AEMFCs are similar to those used for anode catalysts, involving galvanostatic and potentiostatic approaches. However, compared to the extensive studies on anode catalysts, research on the stability of cathode catalysts in AEMFCs has been relatively limited. Pt/C, as the benchmark cathode catalyst, maintained a stable voltage at a constant current density of 600 mA cm^{-2} at 70 °C for over 440 h in an H$_2$/air(CO$_2$-free) AEMFC.[68a]

A promising ORR catalyst, CoO$_x$ nanoparticles supported on N-doped carbon (N-C-CoO$_x$), was tested in an H$_2$/air (CO$_2$-free) AEMFC at a constant current density of 600 mA cm^{-2} at 65 °C, showing a voltage loss of 15% for 100 h.[20] The most significant reduction in performance was observed in the mass transport region of the polarization curve.

Iron and nitrogen co-doped carbon (Fe/N/C) catalysts have been intensively developed for fuel cells, with their decay mechanisms studied in both acidic and alkaline media.[96]

**ADVANCED
SCIENCE NEWS**

www.advancedsciencenews.com

**ADVANCED
MATERIALS**

www.advmat.de

A commercial Fe/N/C catalyst (PMF11904) with mesopores demonstrated stable performance, maintaining an operating voltage above 0.6 V (initially 0.68 V to 0.61 V) at a constant current density of 600 mA cm^{-2} for 100 h in an H$_2$/O$_2$ AEMFC at 80 °C.[24] Additionally, a bimetal-doped catalyst, Fe and Co SAs in N-doped mesoporous carbon (FeCoNC-MgOAc), exhibited a voltage degradation of 1.7 mV h^{-1} after 24 h of operation at 55 °C and a constant current density of 600 mA cm^{-2} in an H$_2$/O$_2$ AEMFC.[88]

3.2.5. Summary and Outlook of Cathode Catalysts

By taking advantage of the alkaline electrolyte, the ORR is not a limiting factor in AEMFCs, making the use of Pt-free catalysts feasible. Carbon-supported nanoparticle and atomically dispersed catalysts are among the most promising ORR catalysts for AEMFCs.

Among carbon-supported nanoparticle catalysts, Mn, Co, and Mn-Co oxides are commonly used due to their high activity and stable operation for over 100 h in the alkaline environment of AEMFCs. Atomically dispersed catalysts, such as Fe/N/C catalysts, also show great potential for AEMFCs, benefiting from extensive research in recent years, particularly in the context of PEMFC. The commercial Fe/N/C catalyst (PMF11904), featuring mesoporous features produced using SiO$_2$ templates, has achieved the highest peak power density (2.05 W cm^{-2}) and demonstrated stable voltage output in H$_2$/O$_2$ AEMFCs, highlighting the potential of Fe/N/C catalysts for AEMFC applications.[24]

Various methods have been employed to prepare ORR catalysts, including precursor impregnation followed by H$_2$ reduction,[75] heat-decomposition method,[31,72d,f,j,73d,75,79,85,87,91d] template-assisted heat-decomposition method.[20,24,72a,c,73a,c,88,89] oleylamine method,[74] solid-state reaction,[32] wet reduction method,[71c,79] and hydrothermal method.[21,71d,78] The template-assisted heat-decomposition method is particularly notable for synthesizing ORR catalysts, as mesoporous structures enhance mass transfer. Gas-phase synthesis techniques, such as chemical vapor decomposition and atomic layer decomposition, are also applicable for preparing ORR catalysts.

While the performance of PGM-free cathode catalysts in AEMFCs is promising, the long-term stability of Mn-Co oxides and Fe/N/C catalysts requires further investigation. The decay mechanisms of Fe/N/C catalysts in alkaline media have recently gained attention.[96,97] More in-depth studies, particularly those employing in-situ techniques such as Mössbauer spectroscopy and X-ray absorption spectroscopy, are needed to better understand the stability of Fe/N/C catalysts in AEMFCs.

4. Anion Exchange Polymers

Anion exchange polymers (AEPs), which are used as anion exchange membranes (AEMs) and anion exchange ionomers (AEIs) in AEMFC, played a significant role in the recent emerging AEMFC technology.[98] Classical alkaline fuel cells use liquid electrolytes, which are vulnerable because of the volatile properties of liquid electrolytes and contaminants, such as CO$_2$, causing carbonate precipitation in electrolytes. The usage of AEPs as solid electrolytes for AEMFCs was pioneered by Varcoe in 2005, and it aimed to replace the conventional approach of using separators soaked in an alkaline solution.[11] Since then, the AEPs have been developed rapidly. AEPs are usually formed by a polymer backbone, such as aromatic hydrocarbon polymers, functionalized with cationic functional groups, such as quaternary ammonium groups (QA) and imidazolium groups (IM).[17,99] In AEMFCs, the AEPs transport OH$^-$ anions as counter ions from the cathode to the anode. Nowadays, the commercially available AEPs include FAA series (Fumatech Corporation), Sustainion (Dioxide Materials), Aemion+ (Ionomr Innovations), A201 (Tokuyama), PiperION (Versogen), and so on.[7d,100] However, the AFMFCs with these commercially available membranes were operated around 60 °C, and the studies of these commercial AEPs in AEMFCs are limited. More studies with commercially available AEPs and further optimizations in AEMFCs are desired to obtain stable and long fuel cell performance at a wider temperature range of 60–100 °C and various humidity conditions in AEMFCs.[9]

AEPs degrade in alkaline media, and the underlying mechanisms have been studied. In AEPs containing QA and IM cationic groups, degradation mechanisms such as Hofmann degradation (E_2), nucleophilic substitution (SN_2), or ring-opening reaction via E_2 and SN_2 are likely to happen, resulting in the loss of cationic groups (**Figure 10a,b**).[101] In poly(aromatic ether)-based polymers (**Figure 11a**), such as PEEK, PSF, and PPO, the aryl-ether cleavage reactions were observed (Figure 10c).[101e,102] Those reactions can significantly affect the lifespan of AEPs. Cutting-edge AEMs were designed to avoid those degradation reactions.[68b,103]

This section will focus on the review of AEPs in three parts: i) Effects of cationic groups and backbones on AEPs' performances, ii) AEM-properties-enhancing methods, and iii) Ionomers and constructing triple-phase boundary. These three parts of AEPs are essential for achieving high-performance AEMFC by controlling four AEP-related aspects in AEMFC. They are the chemical stability of AEP, the ionic conductivity of AEP, the mechanical stability of AEP, and the interaction between AEI and catalyst. The chemistry of cationic groups and backbone determines the chemical stability of AEPs. The ionic conductivity of AEP is mainly controlled by the ion exchange capacity (IEC) of the AEP and the ion conduction pathway, which can be optimized by the synthesis route and constructing a phase-segregated structure. The mechanical stability of AEP can be improved by choosing a high-molecular-weight polymer backbone and applying the crosslinking method. AEIs, except for the chemical and mechanical stability, also desire weak adsorption to catalysts.

4.1. Effects of Cationic Groups and Polymer Backbones

As mentioned above, the nature of cationic groups and polymer backbones significantly affect the AEP performance, especially the durability. The QA and IM cationic functional groups are most widely studied despite their potential degradation.[7d,98a,100b,106] The other kinds of cation functional
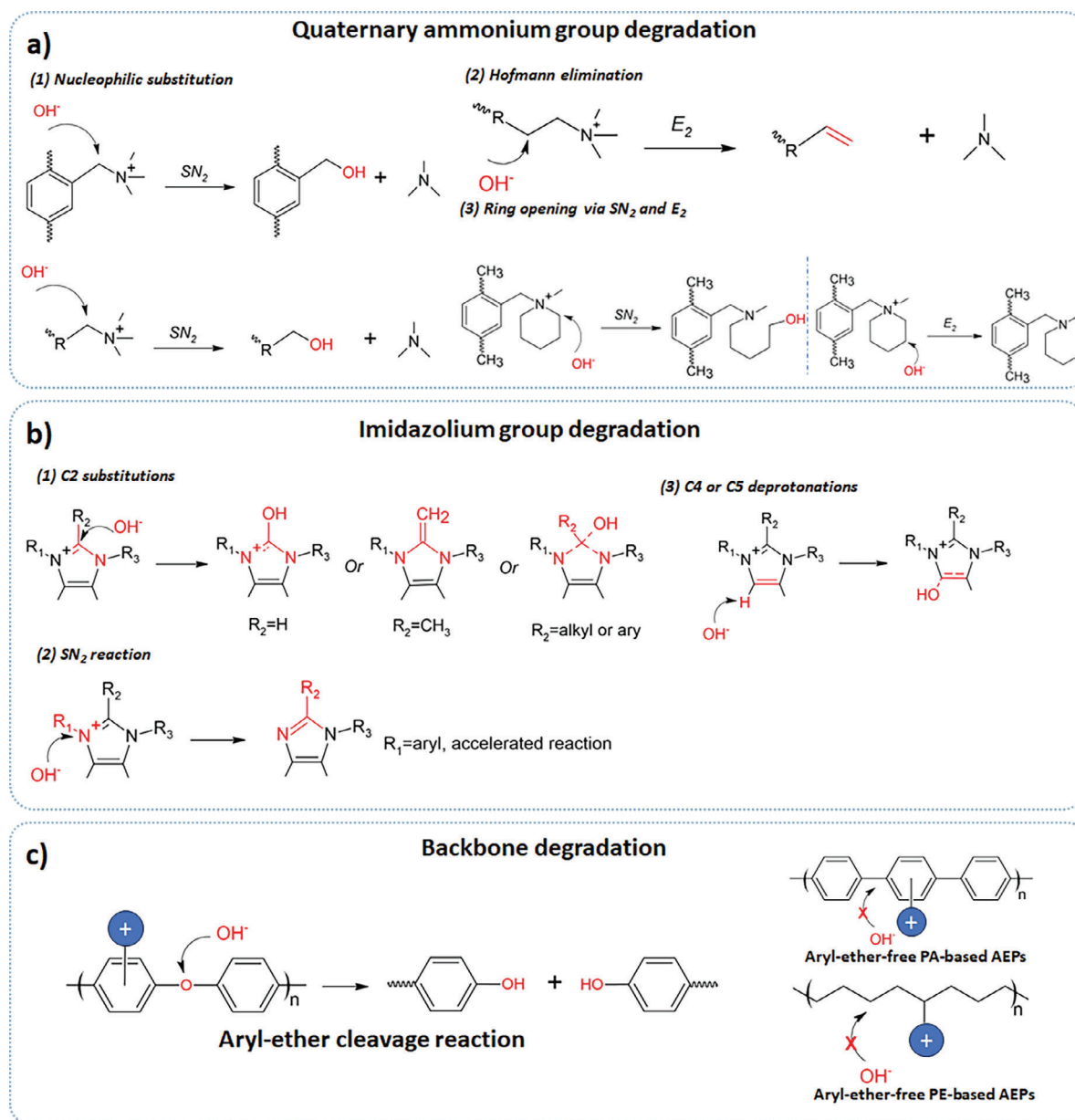
ADVANCED
SCIENCE NEWS

www.advancedsciencenews.com

ADVANCED
MATERIALS

www.advmat.de

Figure 10. a) Degradation pathways of quaternary ammonium groups; Reproduced with permission.[98a] Copyright 2021, Elsevier; Reproduced with permission.[104] Copyright 2022, American Chemical Society. b) Degradation pathways of imidazolium groups; Reproduced with permission.[98a] Copyright 2021, Elsevier. c) Schematic presentation of OH-mediated backbone degradation with/without aryl-ether cleavage reactions; Reproduced with permission.[105] Copyright 2022, John Wiley and Sons.

groups, such as phosphonium-based AEMs,[107] sulfonium-based AEMs,[108] and metallocenium-based AEMs,[109] were also studied.[110] In the backbone structure, aryl-ether cleavage reactions were proven to shorten the lifespan of AEP in alkaline conditions.[102b] Avoiding aryl-ether-containing polymer backbones should be paramount in designing stable AEPs.[98a,111]

This section will review the recently developed AEMs and AEIs with high AEMFC performances based on these criteria. They have also been summarized in **Table 3** with commercially available membranes for comparison.

4.1.1. The Cationic Group Effects in AEPs

In the development of AEP, the QA group and IM group are the most studied cationic groups.[7d,98a,100b,112] Yet, due to their degradation, phosphonium- and sulfonium-based AEPs and the emerging organometallic-cationic groups were also studied. However, it is essential to note that the AEMFC data with cation functional groups, including IM, phosphonium, sulfonium, and organometallic-cationic groups, are rarely reported.[98a]

Quaternary Ammonium Group: Trimethylammonium is a commonly used QA group; for instance, the cationic group
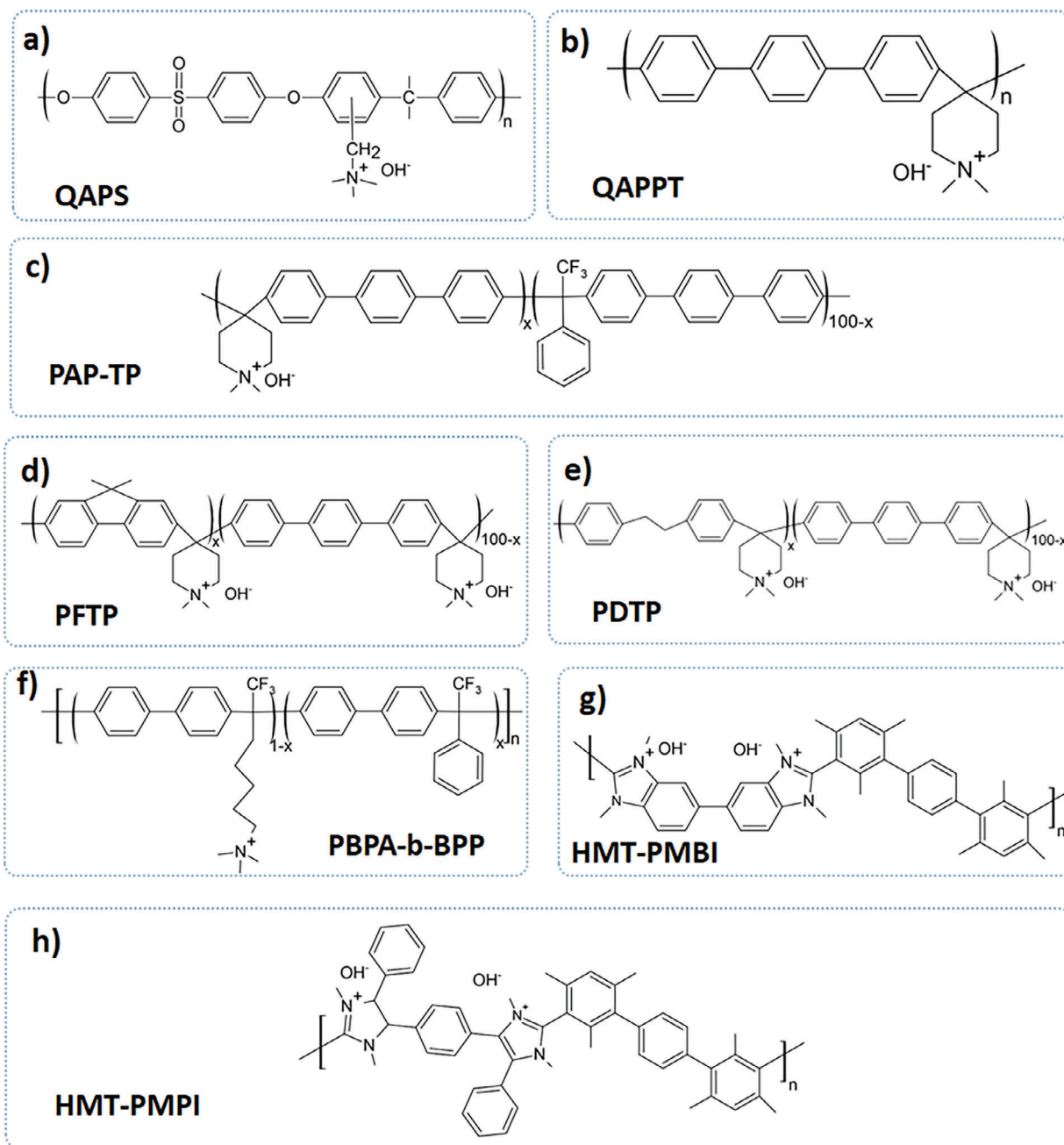
Figure 11. Chemical structures of a) Quaternary ammonia polysulfone (QAPS); Reproduced with permission.[99b] Copyright 2010, John Wiley and Sons. b) Quaternary ammonia poly (N-methyl-piperidine-co-p-terphenyl) (QAPPT); Reproduced with permission.[68b] Copyright 2018, Elsevier. c) Poly(aryl piperidinium) based on terphenyl (PAP-TP); Reproduced with permission.[22] Copyright 2019, Springer Nature. d) Poly(fluorene-co-terphenyl N,N'-dimethylpiperidinium) (PFTP); Reproduced under terms of the CC-BY license.[25] Copyright 2021, The Authors, published by Springer Nature. e) Poly(alkyl-terphenyl piperidinium) (PDTP); Reproduced with permission.[26] Copyright 2021, John Wiley and Sons. f) Multiblock poly(biphenyl alkylene) copolymers poly(biphenyl ammonium-b-biphenyl phenyl) (PBPA-b-BPP); Reproduced with permission.[30] Copyright 2023, John Wiley and Sons. g) Hexamethyl-p-terphenyl poly(benzimidazolium) (HMT-PMBI);[122] h) Poly(arylene-imidazolium) (HMT-PMPI) Reproduced with permission.[122] Copyright 2017, American Chemical Society.

in quaternary ammonia polysulfone (QAPS, Figure 11a).[99b] However, its stability is compromised by degradation pathways such as Hofmann degradation (E_2) and nucleophilic substitution (SN_2), as illustrated in Figure. 10 a. Due to these degradation mechanisms, the alkaline stability of trimethylammonium poses challenges; for instance, QAPS demonstrated stability for only 120 hours at 75 °C.[99b,113]

With intensive studies of the stability of quaternary ammoniums, aliphatic heterocyclic quaternary ammoniums, and medium-long alkyl site-chain structures showed excellent

Table 3. Typical anion exchange membranes and ionomers.

Membrane	IEC[a] [mmol g⁻¹]	OH⁻ Conductivity@ 80 °C [mS cm⁻¹]	HOR Catalyst	HOR Catalyst Loading [mg$_{metal}$ cm⁻²]	ORR Catalyst	ORR Catalyst Loading [mg$_{metal}$ cm⁻²]	Ionomer	Feed Gas	T_{Cell} [°C]	T_{DP} of Anode/Cathode [°C]	Back-pressure of Anode/Cathode [MPa]	PPD[b] [W cm⁻²]	Refs.
Poly(arylene)-based membrane													
aQAPS-S₈	1.00	108	PtRu/C	0.40	Pt/C	0.40	aQAPS-S₁₄	H₂/O₂	60	60/60	0.10/0.10	1.00	[13]
DQEO	1.13	40 (25 °C)	Pt/C	0.50	Pt/C	0.50	–	H₂/O₂	60	60/60	0/0	0.29	[118a]
PX75-T50	0.91	111	PtRu/C	0.50$_{Pt}$	Pt/C	0.50	PVBC	H₂/O₂	80	80/80	0/0	0.73	[146c]
QAPPT	2.65	137	Pt/C	0.40	Pt/C	0.40	QAPPT AEI	H₂/O₂	80	80/80	0.10/0.10	1.45	[68b]
PAP-TP-85	2.37[c]	175	Pt/C	0.40	Pt/C	0.40	PAP-BP-60	H₂/O₂	95	95/95	0.10/0.10	0.87	[22]
PFTP-13	2.81	208	PtRu/C	0.42	Pt/C	0.33	PFBP-14	H₂/O₂	80	73/80	0.13/0.13	2.34	[25]
PDTP-25	2.80	166	PtRu/C	0.39	Pt/C	0.26	PFBP-14	H₂/O₂	80	60/80	0.13/0.13	2.58	[26]
PBPA-b-BPP-0.10	2.42[c]	162	PtRu/C	0.41	Pt/C	0.28	PBPB-b-BPP-0.15	H₂/O₂	80	73/80	0.13/0.13	2.41	[30]
OBImPPO26-PEG05	1.96	94	PtRu/C	0.50	Pt/C	0.50	QPPO	H₂/O₂	60	60/60	0/0	0.41	[121]
HMT-PMBI	2.50	17 (90 °C)	Pt/C	0.40	Pt/C	0.40	HMT-PMBI	H₂/O₂	60	60/60	0.20/0.20	0.37	[112]
HMT-PMPI	2.61[c]	280	Pt/C	0.50	Pt/C	0.50	HMT-PMPI	H₂/O₂	80	72/80	0/0	0.82	[122]
HIm-PBI	2.09[c]	63	PtRu/C	0.40$_{Pt}$	Pt/C	0.40	HIm-PBI	H₂/O₂	60	60/60	–	0.44	[123]
PFBA-QA-0.4	2.17	78 (30 °C)	Pt/C	0.50	Pt/C	0.50	PFBA-QA-0.7	H₂/O₂	60	60/60	0/0	0.61	[130a]
PFPE-Pi	2.49[c]	80	PtRu/C	0.40	Pt/C	0.40	PFPE-Pi	H₂/O₂	80	80/80	0/0	0.66	[132]
QPSB	1.81	99	PtRu/C	0.50	Pt/C	0.50	QPAP	H₂/O₂	80	80/80	0/0	0.90	[133]
BAF-QAF	1.90	134	Pt/C	0.20	Pt/C	0.20	BAF-QAF	H₂/O₂	60	60/60	0.10/0.10	0.32	[134f]
QPAF-C3-Pip	1.26[c]	55 (30 °C)	Pt/C	0.20	Pt/C	0.20	QPAF-4	H₂/O₂	80	80/80	0/0	0.23	[134h]
qPBPTT-5	1.93	117	PtRu/C	0.50	Pt/C	0.50	qPBPTT-5	H₂/O₂	60	60/60	–	0.32	[151a]
b-PTP-2.5	2.81[c]	147	PtRu/C	0.60	Pt/C	0.40	PFBP	H₂/O₂	80	73/80	0.13/0.13	2.30	[15 1b]
b-PTP-2.5	2.81[c]	147	PtRu/C	0.60	Pt/C	0.40	PFBP	H₂/Air[d]	80	73/80	0.13/0.13	1.30	[15 1b]
b-PDTP-TRIP-5	2.95[c]	100	PtRu/C	0.39	Pt/C	0.26	PFBP	H₂/O₂	80	73/80	0.13/0.13	2.50	[34]
Polyethylene-based membrane													
ETFE-AEM	2.11	200	PtRu/C	0.60	Pt/C	0.40	ETFE-AEI	H₂/O₂	70	59/59	0/0	1.57	[14a]
LDPE-AEM	2.87	145	PtRu/C	0.60	Pt/C	0.40	ETFE-AEI	H₂/O₂	80	80/80	0/0	1.45	[135d]
HDPE-AEM	2.44	214	PtRu/C	0.40$_{Pt}$	Pt/C	0.40	ETFE-AEI	H₂/O₂	80	78/78	0/0	2.55	[68a]
M20C9NM5NC5N	2.76	201	PtRu/C	0.60	Pt/C	0.60	ETFE-AEI	H₂/O₂	70	–	0/0	1.28	[136a]
F20C9N	1.12	91	PtRu/C	0.70	Pt/C	0.50	ETFE-AEI	H₂/O₂	60	51/56	0.10/0.10	1.01	[103c]
PE15	1.24	68	PtRu/C	0.40	Pt/C	0.40	QAPPT-AEI	H₂/O₂	80	80/80	0.20/0.20	1.00	[137d]

(Continued)

2410106 (24 of 52)

Table 3. (Continued)

Membrane	IEC[a] [mmol g⁻¹]	OH⁻ Conductivity @80 °C [mS cm⁻¹]	HOR Catalyst	HOR Catalyst Loading [mg_metal cm⁻²]	ORR Catalyst	ORR Catalyst Loading [mg_metal cm⁻²]	Ionomer	Feed Gas	T_{Cell} [°C]	T_{DP} of Anode/Cathode [°C]	Back-pressure of Anode/Cathode [MPa]	PPD[b] [W cm⁻²]	Refs.
Polynorbornene-based membrane													
XL35-rPNB-X$_{60}$-Y$_{40}$	2.20[c]	109	Pt/C	2.10	Pt/C	2.10	PNB-AEI	H$_2$/O$_2$	60	–	–	0.12	[138a]
GT82-5	3.88[c]	212	PtRu/C	0.70	Pt/C	0.60	ETFE-AEI	H$_2$/O$_2$	80	66/75	0.05/0.10	3.50	[23]
GT64-15	3.28[c]	198	PtRu/C	0.70	Pt/C	0.60	ETFE-AEI	H$_2$/O$_2$	80	67/74	–	3.37	[147]
PNB-X$_{62}$-Y$_{38}$	1.88[c]	123	Pt/C	2.10	Pt/C	2.10	PNB-AEI	H$_2$/O$_2$	60	46/46	0.10/0.10	0.54	[139a]
Polystyrene-based membrane													
PVA-1.8PVBMA	1.62	203	PtRu/C	0.40	FeN$_x$-CNTs	2.00	QPPO	H$_2$/O$_2$	60	–	–	1.20	[140]
PVA-0.8PQVBC$_{40\%}$	1.48	98	PtRu/C	0.40	FeN$_x$-CNTs	4.00	QPPO	H$_2$/Air[d]	60	60/60	0.20/0.20	0.64	[141]
UHMWPD-VPC	1.51	102	PtRu/C	0.40$_{catalyst}$	Pt/C	0.4$_{catalyst}$	PAP-BP-60	H$_2$/O$_2$	65	65/65	0.15/0.15	1.01	[142]
UHMWPD-VPC	1.51	102	PtRu/C	0.40$_{catalyst}$	Pt/C	0.4$_{catalyst}$	PAP-BP-60	H$_2$/Air[d]	65	65/65	0.15/0.15	0.53	[142]
XL-100-SEBS-C$_5$-TMA-0.8	1.50	65	PtRu/C	0.5Pt	Pt/C	0.6	FLN	H$_2$/O$_2$	60	–	0.290.29	0.52	[143a]
C$_4$-CAQSEBS	1.35	16 (30 °C)	PtRu/C	0.30	Pt/C	0.30	QASEBS	H$_2$/O$_2$	60	60/60	0.20/0.20	0.64	[145]
OH-SEBS-70	3.37[c]	189	PtRu/C	0.5$_{catalyst}$	Pt/C	0.5$_{catalyst}$	QPTFP-25	H$_2$/O$_2$	80	80/80	0/0	1.01	[144b]
SEBS-TMA	2.41[c]	89 (60 °C)	Pt/C	0.20	Pt/C	0.20	TMAKC6PP	H$_2$/O$_2$	80	80/80	0.10/0.10	0.24	[143b]
Commercially available membrane													
Aemion+	2.94	–	PtRu/C	0.50$_{Pt}$	Pt/C	0.50	Aemion+	H$_2$/O$_2$	70	68/68	0.10/0.10	0.88	[120]
Tokuyama A901	–	38	Pt/C	0.40	Pt/C	0.40	Tokuyama AS-4	H$_2$/O$_2$	80	85/85	0.25/0.25	0.74	[98a]
FAA	–	40 (30 °C)	Pt/C	0.40	Pt/C	0.40	Fumion	H$_2$/O$_2$	80	60/60	0.10/0.10	0.52	[98a]

a) IEC: ion-exchange capacity; b) PPD: peak power density; c) in the unit of meq. g⁻¹; d) Air: CO$_2$-free.

**ADVANCED
SCIENCE NEWS**

www.advancedsciencenews.com

**ADVANCED
MATERIALS**

www.advmat.de

alkaline stability compared to other QA cationic groups.[104,113] The resistance of piperidinium against both Hofmann degradation and nucleophilic substitution in alkaline conditions originates from the unfavorable bond angles and lengths in the reaction transition states of the 6-membered aliphatic heterocycles.[113]

Quaternary ammonia poly (N-methyl-piperidine-co-p-terphenyl) (QAPPT, Figure 11b) AEM with piperidinium QA groups was synthesized to meet the requirement of high-temperature AEFMC operation.[68b] The OH$^-$ conductivity of QAPPT was 137 mS cm^{-1} at 80 °C with an IEC value of 2.65 mmol g^{-1}, and the in-plane swelling degree was 9.5% under a fully hydrated state. QAPPT retained 95% and 84% of its conductivity after soaking in 1 and 3 mol L^{-1} NaOH, respectively, for 5040 h at 80 °C, demonstrating enhanced alkaline stability compared to trimethylammonium cationic groups. The H$_2$/air (CO$_2$-free) AEMFC stability test showed that the QAPPT sustained a stable operation with a current density of 200 mA cm^{-2} at 80 °C for 125 h.

The Yan group synthesized a series of poly(aryl piperidinium) (PAP)-based AEMs with piperidinium QA cationic groups.[22] The typical PAP-based AEM (PAP-TP-85, TP: p-terphenyl, 85: the molar ratio between N-methyl-4-piperidone and 2,2,2-trifluoroacetophenone, Figure 11c) was 25 μm in thickness and the corresponding OH$^-$ conductivity of 193 mS cm^{-2} at 95 °C. In the alkaline stability test, the IEC of PAP-TP-85 decreased only 3% from 2.37 to 2.29 meq. g^{-1} and no detectable chemical change after 2000 h in 1 mol L^{-1} KOH at 100 °C.

The Lee group also used the piperidinium QA cationic groups in AEMs. Several poly(fluorenyl aryl piperidinium) membranes (PFBP, PFPN, and PFTP; PFTP is shown in Figure 11d) were synthesized.[25] The PFTP-13 AEM displayed the OH$^-$ conductivity of 208 mS cm^{-1} at 98 °C and maintained 80% ion conductivity after 5 mol L^{-1} NaOH treatment at 80 °C for 2000 h. Similar QA cationic groups were used in the aliphatic chain-containing poly(diphenyl-terphenyl piperidinium) (PDTP) polymers with piperidinium QA cationic groups, PDTP-25 (Figure 11e), were then synthesized by the same group.[26] The PDTP-25 exhibited an OH$^-$ conductivity of 166 mS cm^{-1} at 80 °C with an IEC of 2.80 mmol g^{-1}, showing no degradation after 1500 h of treatment in 1 mol L^{-1} NaOH at 80 °C.

The stability of piperidinium remains challenging under harsh conditions, such as high alkaline concentration, elevated temperatures, and prolonged testing. Degradation pathways for piperidinium include the Hofmann degradation (E_2), the nucleophilic substitution (SN_2), and the ring-opening via nucleophilic substitution (SN_2) and Hofmann degradation (E_2), as illustrated in Figure 10a.[114] Hofmann elimination (E_2) is considered the primary degradation pathway for piperidiniums.[115]

Quinuclidinium (Qui), a bridged bicyclic ammonium, exhibits stable alkaline stability because of its unique structure, which increases the Gibbs free energy of Hofmann elimination (E_2) and facilitates electron donation from the arylene chain.[116] For instance, the quinuclidinium-containing cationic group retained 67% of its initial quantity after 720 h in 1 mol L^{-1} KOH/CD$_3$OH at 80 °C.[117] Zeng et al. developed a poly(aryl quinuclidinium) AEM that maintained stable OH$^-$ conductivity (139 mS cm^{-1} at 80 °C) after 1800 h in 10 mol L^{-1} NaOH at 80 °C.[116a] Recently, Sun and coworkers synthesized a series of quinuclidinium-containing

AEMs (PAQs).[116b] The PAQ with 5 mol % branching moiety (PAQ-5) demonstrated the highest OH$^-$ conductivity of 187 mS cm^{-1} at 80 °C with an IEC of 2.65 mmol g^{-1}, reduced water uptake (17%, at 80 °C) and a low swelling rate (6%, at 80 °C). In stability tests, PAQ-5 retained 97% of its initial OH$^-$ conductivity after immersion in 1 mol L^{-1} KOH at 80 °C for 2500 h and 99% after 2446 h of operation in an AEM-water electrolyzer at 80 °C, demonstrating its potential for AEMFC applications. However, reports on Qui-containing AEMs in AEMFCs remain limited.[118] Li et al. reported a quinuclidinum-containing AEM, named DQEO, which achieved an OH$^-$ conductivity of 40 mS cm^{-2} at 25 °C, attributed to enhanced hydrophilicity from an alkoxyl extender. In H$_2$/O$_2$ AEMFC tests, DQEO reached a peak power density of 0.29 W cm^{-2} at 60 °C.[118a]

Medium-long cationic alkyl side-chain structures in cationic groups mitigate the radical-attacking backbone degradation caused by the electron-withdrawing effect of cationic groups.[113,119] Ma et al. synthesized poly(biphenyl ammonium-b-biphenyl phenyl)s (PBPA-b-BPP, Figure 11f) with alkyl side chains and a block-type structure.[30] The OH$^-$ conductivity of PBPA-b-BPP was 162 mS cm^{-1} at 80 °C, enhanced by the microphase separation, which limited the swelling ratio to 26% at 80 °C. PBPA-b-BPP retained 87% of its ammonium groups after immersing in 2 mol L^{-1} NaOH for 3750 h at 80 °C. In H$_2$/O$_2$ AFMFC testing, PBPA-b-BPP reached a peak power density of 2.41 W cm^{-2} at 80 °C and operated for 330 h at a current density of 600 mA cm^{-2} at 70 °C with no significant chemical degradation.

Aliphatic heterocyclic quaternary ammonium compounds have shown considerable improvements in both alkaline and AEMFC stability compared to trimethylammonium. The unique structure of quinuclidinium further enhances its alkaline stability, making it a promising cationic group in AEMFCs. Additionally, medium-length cationic alkyl side-chain structures promote microphase separation morphology, which improves ion conductivity and overall stability.

Imidazolium Group: Aemion+ is a commercially available IM-based AEM from Ionomr Innovations Inc. An Aemion+ with an IEC of 2.94 mmol g^{-1} was studied by Holdcroft and coworkers.[120] A degradation of ring opening was observed in Aemion+ after soaking in 3 mol L^{-1} KOH at 80 °C for 168 h. In the H$_2$/O$_2$ AEMFC test, the Aemion+ with a final thickness of 10 μm achieved a peak power density of 0.88 W cm^{-2} at 70 °C. With the direct membrane deposition technique, the H$_2$/O$_2$ AEMFC reached a peak power density of 1.4 W cm^{-2} at 70 °C and in the stability test of the same membrane showed a voltage decay of 7.1 mV h^{-1} operated under a constant current density of 600 mA cm^{-2} for 20 h.

Xu and coworkers synthesized imidazolium-containing AEM, named OBIPPO26, with 0.5% polyethylene glycol grafts (OBImPPO26-PEG0.5).[121] By introducing the polyethylene glycol, the cation-dipole interactions between electronegative alkoxy and imidazolium boosted the phase-segregated structures to enhance the OH$^-$ conduction kinetics. The OBImPPO26-PEG0.5 exhibited an OH$^-$ conductivity of 93.8 mS cm^{-1} at 80 °C, which is higher than its non-grafted counterpart (80.9 mS cm^{-1}), retained 80% of initial conductivity after treating in 2 mol L^{-1} NaOH for 216 h at 60 °C. In the H$_2$/O$_2$ AEMFC test, a peak power density reached 0.41 W cm^{-2} at 60 °C with OBImPPO26-PEG0.5.

**ADVANCED
SCIENCE NEWS**

www.advancedsciencenews.com

**ADVANCED
MATERIALS**

www.advmat.de

The stability test with OBImPPO26-PEG0.5 showed that the single-cell operated for 5 h with 65% voltage preservation due to the aryl-ether bond cleavage of the backbone.

Wright et al. prepared an AEM, named HMT-PMBI, by methylation of poly(benzimidazolium) with IM as a cationic group (HMT-PMBI, Figure 11g).[112] The HMT-PMBI with 89% methylation showed a conductivity of 17.3 mS cm^{-1} at 90 °C and an IEC value of 2.50 mmol g^{-1}. No significant degradation of HMT-PBI was observed after 168 h of soaking in 1 mol L^{-1} NaOH at room temperature. HMT-PBI-based AEMFC achieved a power density of 0.37 W cm^{-2} at 60 °C with both Pt/C anode and cathode and was operated for 100 h at various current densities up to 160 mA cm^{-2} in H$_2$/O$_2$.

Fan et al. synthesized a poly(arylene-imidazolium), HMT-PMPI (Figure 11h), using a microwave polycondensation method and incorporating steric protection around the C2-position. The resulting polymer exhibited an ICE of 2.61 meq. g^{-1} and an estimated OH$^-$ conductivity of 280 mS cm^{-1} at 80 °C in AEMFC.[122] MHT-PMPI demonstrated remarkable chemical stability, showing no degradation after immersion in 10 mol L^{-1} KOH at 100 °C for 168 h. In H$_2$/O$_2$ AEMFC testing, HMT-PMPI achieved a peak power density of 0.82 W cm^{-2} and operated for 10 h at 80 °C with diminished performance due to partial dissolution.

Polybenzimidazole (PBI) backbone structure with long pendant imidazolium cationic groups on N1/N3 position, named HIm-PBI, was synthesized by Lin et al.[123] The HIm-PBI AEM showed a hydroxide conductivity of 63.4 mS cm^{-1} at 80 °C, which was higher than that of the PBI-based AEM with shorter pendant imidazolium groups (PIm-PBI). The higher OH$^-$ conductivity of HIM-PBI was ascribed to the longer pendant imidazolium cationic groups, which favored the formation of larger phase-segregated structures to facilitate OH$^-$ transports. The HIm-PBI showed a decrease of IEC from 2.09 meq. g^{-1} to 1.88 meq g^{-1} after treating in 2 mol L^{-1} KOH at 80 °C for 240 h. In the H$_2$/O$_2$ AEMFC test, the single cell with HIm-PBI showed a peak power density of 0.44 W cm^{-2} at 60 °C, higher than that with PIm-PBI, 0.34 W cm^{-2}.

A series of imidazolium (IM)-based AEMs was synthesized by grafting four different imidazolium cationic groups, i.e., N-vinyl imidazolium (NVIm), 2-methyl-NV imidazolium (2MVIm), 123-trimethyl-4-vinyl imidazolium (4VIm), and 2-styryl-1,1-dipropyl imidazolium (StIm) on the radiation-grafting benzyl trimethylammonium (BTMA) AEM by Mahmoud et al.[124] Among the IM-based graft-type AEMs, the one with STIm cationic groups AEM exhibited a hydroxide conductivity of 109 mS cm^{-1} at 60 °C. In the H$_2$/O$_2$ AEMFC test, StIm-based AEM showed a peak power density of 0.71 W cm^{-2} at 60 °C. In the H$_2$/O$_2$ stability test, 69% of voltage retention was achieved by STlm under a constant current density of 50 mA cm^{-2} after 230 h.

Holdcroft and coworkers further studied the IM-containing AEP to extend the operation time, finding the membrane with poly(arylene imidazolium) backbone and N1/N3-butyl-substituted imidazolium (PAImBB).[125] The PAImBB showed a cation remaining of 98% in 10 mol L^{-1} NaOH at 80 °C after 240 h with a Cl$^-$ conductivity of 8.5 mS cm^{-1}. In the H$_2$/O$_2$ AEMFC test, PAImBB achieved a peak power density of 0.25 W cm^{-2} at 70 °C.

The alkaline stability of IM cationic groups presents significant challenges. Stability studies have shown that the durability of IM groups is highly sensitive to structural modifications. Substituents at the C2 position enhance the alkaline stability by shielding the IM groups from nucleophilic addition (SN_2) attack.[117,122,124,126] C4/C5 substitution with methyl groups or phenyl groups was also proved to increase the stability of the IM group by blocking the deprotonation and other degradation pathway.[127] The substitution with n-butyl or isopropyl groups at the positions of N1 and N3 was observed to influence the rate of SN_2 attack at the C2 position and protect the N1/N3 positions.[117,125,126,128] With those stability enhancement strategies, the stability of IM groups could be significantly improved, making them suitable for applications in AEMFCs.

4.1.2. The Backbone Effects in AEP

Aryl-ether-containing backbones were proven not stable under alkaline conditions because the aryl-ether group facilitates the substitution with hydroxide to the carbon near the electronegative oxygen atom, i.e., the aryl-ether cleavage reaction (Figure 10c), like quaternary ammonia polysulfone (QAPS, Figure 11a) AEP.[17,99b] Aryl-ether-free backbone-based polymers are more stable than aryl-ether polymers by eliminating the aryl-ether cleavage reactions.[102] There are several ways to synthesize aryl-ether-free polymers, such as the radiation-grafting method, Friedel-Crafts polycondensation, ring-opening metathesis polymerization (ROMP), Yamamoto coupling polymerization, Ziegler-Natta polymerization, and Diels-Alder polymerization.[98a,105,129]

Poly(arylene) (PA)-Based AEP: PA-based AEP is the type of AEPs that contain aromatic ring backbones or aromatic cationic groups, e.g., imidazolium, in the backbones. The PA-AEPs have been gaining intensive research in recent years, and some of them have been commercialized, such as Aemion+ (Ionomr Innovations) and PiperION (Versogen).[100a,104,105]

Quaternary ammonia poly (N-methyl-piperidine-co-p-terphenyl) (QAPPT, Figure 11b) AEM, developed in Zhuang's research group in 2018, is one of the PA-AEPs. As discussed in Section 4.1.1., the QAPPT with an OH$^-$ conductivity of 137 mS cm^{-1} at 80 °C and reached a peak power density of 1.45 W cm^{-2} at 80 °C in the H$_2$/O$_2$ AEMFC and a stable operation of 125 h at a current density of 200 mA cm^{-2} at 80 °C with H$_2$/air (CO$_2$-free) feed gases.[68b]

Yan and coworkers used trifluoroacetophenone and N-methyl-4-piperidone to synthesize poly(aryl piperidine) polymer (PAP) with p-terphenyl (TP) via polyhydroxyalkylation to produce a PA-based AEP, named PAP-TP-85 (Figure 11c).[22] The OH$^-$ conductivity of PAP-TP-85 achieved 78 mS cm^{-1} at 20 °C and 193 mS cm^{-1} at 95 °C. The PAP-TP-85 demonstrated 67 MPa stress and 117% strain at break, showing good mechanical properties thanks to the copolymer structure. In the AEMFC test, the MEA with PAP-TP-85 achieved a peak power density of 0.92 W cm^{-2} at 95 °C with H$_2$/air (CO$_2$-free) feed gases. In the stability test at a constant current density of 500 mA cm^{-2} and 95 °C, the voltage loss is 11.5% after 250 h of the test.

Ployfluorenes (FLNs) are one of the promising backbone structures of PA-AEPs thanks to their solvent-processable and alkaline stable characters of them.[130] FLN polymers also reduce the effects of phenyl group adsorption on the surface of

**ADVANCED
SCIENCE NEWS**

www.advancedsciencenews.com

**ADVANCED
MATERIALS**

www.advmat.de

electrocatalysts, which will be discussed in session 4.3. Yang et al. synthesized the (poly[(fluorene alkylene)-co-(biphenyl alkylene)] (PFBA) with trimethylammonium cationic group (PFBA-QA).[130a] The PFBA-QA showed the OH$^-$ conductivity of 78 mS cm^{-2} at 30 °C. In the H$_2$/O$_2$ AEMFC test, the MEA with PFBA-QA achieved a peak power density of 0.61 W cm^{-2} at 60 °C. In the stability test, after 71 h at a constant current density of 200 mA cm^{-2}, the peak power density of PFBA-QA containing AEMFC dropped to 0.24 W cm^{-2} because of the ylide formation and Hofmann elimination.

A FLN polymer, poly(fluorene-co-terphenyl N,N′-dimethylpiperidinium) (PFTP, Figure 11d), was synthesized by Chen et al.[25] The PFTP-13 displayed OH$^-$ conductivity of 208 mS cm^{-1} at 98 °C, lower water uptake, and swelling ratios (ca. 45% and ca. 16%, respectively) and superior gas barrier properties originating from its high molecular weight backbone. The authors used PFTP with PFBP (poly(fluorene-co-biphenyl-N,N′-dimethylpiperidinium) ionomer to fabricate an MEA. In the AEMFC tests, the PFTP-13-based MEA reached 2.34 W cm^{-2} in H$_2$/O$_2$ and 1.25 W cm^{-2} in H$_2$/air (CO$_2$-free) at 80 °C and operated at a current density of 200 mA cm^{-2} in H$_2$/O$_2$ at 70 °C for 200 h with a voltage loss of 3.68%.

The Suzuki coupling reaction, using Pd-complex-based catalysts, is widely employed for synthesizing FLNs and functionalizing backbones of AEPs.[131] A FLN-based AEP with alkyl groups and pendant piperidinium, named PFPE-Pi, was synthesized through this method.[132] The alkyl soft block enhanced the flexibility of PFPE-Pi, resulting in a tensile strength of 19 MPa. PFPE-Pi exhibited an OH$^-$ conductivity of 80 mS cm^{-1} at 80 °C with an IEC of 2.49 meq. g^{-1}, retaining 94% of its conductivity after a stability test in 2 mol L^{-1} KOH at 80 °C for 720 h. In H$_2$/O$_2$ AEMFC testing, PFPE-Pi reached a peak power density of 0.66 W cm^{-2} at 80 °C.

Zhang et al. developed an AEM named QPSB by introducing pendulous piperidinium groups onto a twisted PA-based backbone via the Suzuki coupling reaction.[133] QPSB demonstrated an OH$^-$ conductivity of 99 mS cm^{-1} at 80 °C with an ICE of 1.81 mmol g^{-1}, exhibiting high alkaline stability with only 18% conductivity loss after immersing in 10 mol L^{-1} NaOH solution for 1500 h at 80 °C. This enhanced stability was attributed to the twisted backbone structure, which reduced the squeeze effect on piperidinium rings, improving their stability. In H$_2$/O$_2$ AEMFC testing, QPSB delivered a peak power density of 0.90 W cm^{-2} and maintained a voltage above 0.6 V during 50 h of operation at a constant current density of 200 mA cm^{-2} at 80 °C.

Nickel-catalyzed coupling reactions, which are performed at lower temperatures and shorter times but result in a higher polydispersity index compared to the Suzuki method, are also used for synthesizing PA-based AEPs.[98a] Miyatake and coworkers reported a series of PA-based, fluorinated AEPs produced via nickel-catalyzed coupling reaction.[130b,134] A copolymer (BAF-QAF) with hexafluoroisopropylidene hydrophobic segments and fluorenyl-substituted hydrophilic groups exhibited a microphase-separated morphology, an OH$^-$ conductivity of 134 mS cm^{-1}, and a controlled water uptake of 36%.[134f] In H$_2$/O$_2$ AEMFC testing, BAF-QAF reached a peak power density of 0.32 W cm^{-2}, while a similar polymer, QPAF-4, achieved 0.29 W cm^{-2} at 60 °C.

A partially fluorinated AEP, QPAF-C$_3$-Pip, containing piperidinium cationic groups, was synthesized via a nickel-catalyzed coupling reaction. It demonstrated an OH$^-$ conductivity of 56 mS cm^{-1} with an IEC of 1.26 meq. g^{-1}.[134h] After 736 h in 4 mol L^{-1} KOH at 80 °C, QPAF-C$_3$-Pip retained 80% of its initial conductivity. Its compact heterocyclic ammonium structure also minimized water uptake. In H$_2$/O$_2$ AEMFC testing, QPAF-C$_3$-Pip demonstrated a peak power density of 0.23 W cm^{-2} at 80 °C and operated at a current density of 100 mA cm^{-2} for 240 h with a voltage drop rate of 1.29 mV h^{-1} at 60 °C.

Poly(diphenyl-terphenyl piperidinium) (PDTP) polymers, which contain aliphatic chains, displayed low phenyl adsorption and high molecular weight.[26] The PDTP-series membranes displayed lower H$_2$ permeability than the commercial FAA-3-50 (below 1.00 MPa vs 1.30 MPa). Constructing phase segregated structures, which is an ionic conductivity enhancing method and will be discussed in Section 4.1.3, in PDTP-series membranes. PDTP-25 displayed peak power densities of 2.58 W cm^{-2} and 1.38 W cm^{-2} at 80 °C in H$_2$/O$_2$ and H$_2$/air (CO$_2$-free) AEMFCs, respectively, and operated at a current density of 400 mA cm^{-2} for 100 h at 80 °C in H$_2$/O$_2$ AEMFC without degradation of the cationic groups.

Polyethylene (PE)-Based AEP: PE-based AEPs are anion exchange polymers with the backbone structure of all-aliphatic hydrocarbon. Unlike PA-based AEP, the all-aliphatic hydrocarbon structure of PE-based AEPs prevents the formation of acidic phenol at the cathode, causing fuel cell performance loss. Thanks to their high molecular weight, the all-aliphatic hydrocarbon structure also enhances the mechanical properties of PE-based AEPs.

Various methods, including radiation-grafting polymerization,[14a,68a,135] Zeigler-Natta polymerization,[136] and ring-opening metathesis polymerization (ROMP)[137] synthesized the representative PE-based AEPs. The radiation-grafting polymerization is a well-developed method to design and synthesize stable aryl-ether-free AEMs in AEMFC. Side chains bearing functional groups are controllably grafted onto the polyethylene backbone, and the resulting membranes are denoted as radiation-grafted anion exchange membranes (RG-AEMs).

Recently, a series of sub-30 μm RG-AEMs with excellent performance under AEMFC were reported. Firstly, a 12.7 μm poly(ethylene-*co*-tetrafluoroethylene) (ETFE) film used as a matrix was treated with an electron beam (total dose of 30 kGy) under air, then grafted with vinylbenzyl chloride (VBC) monomer in an aqueous solution followed by an aminating step with an aqueous trimethylamine solution.[14a] The as-synthesized ETFE-AEM possessed a dehydrated thickness of 21 μm, IEC of 2.11 mmol g^{-1}, and water uptake of 59%. To fabricate the MEA, the ETFE-AEM membrane was sandwiched between a PtRu/C anode and a Pt/C or Ag/C cathode. Peak power densities of 1.57 W cm^{-2} (Pt/C) and 1.11 W cm^{-2} (Ag/C) were recorded under H$_2$/O$_2$ at 70 °C AEMFC. The results demonstrate the promising application of ETFE-AEM as a high-performance membrane for AEMFCs.

The main polymer chain of fluorinated or partially fluorinated films, such as ETFE, is vulnerable to electron beam radiation, which strongly affects the mechanical integrity of the membranes, even at low doses. Hence, a new generation of RG-AEMs was synthesized using a fluorine-free polymer, such as the low-density polyethylene (LDPE) films, as a grafting matrix proposed by Wang et al.[135d] The synthetic procedure of LDPE-based AEM is similar to that of ETFE-AEM, and the final products were denoted as LDPE-AEM (**Figure 12a**).[135d,g] The prepared

**ADVANCED
SCIENCE NEWS**

www.advancedsciencenews.com
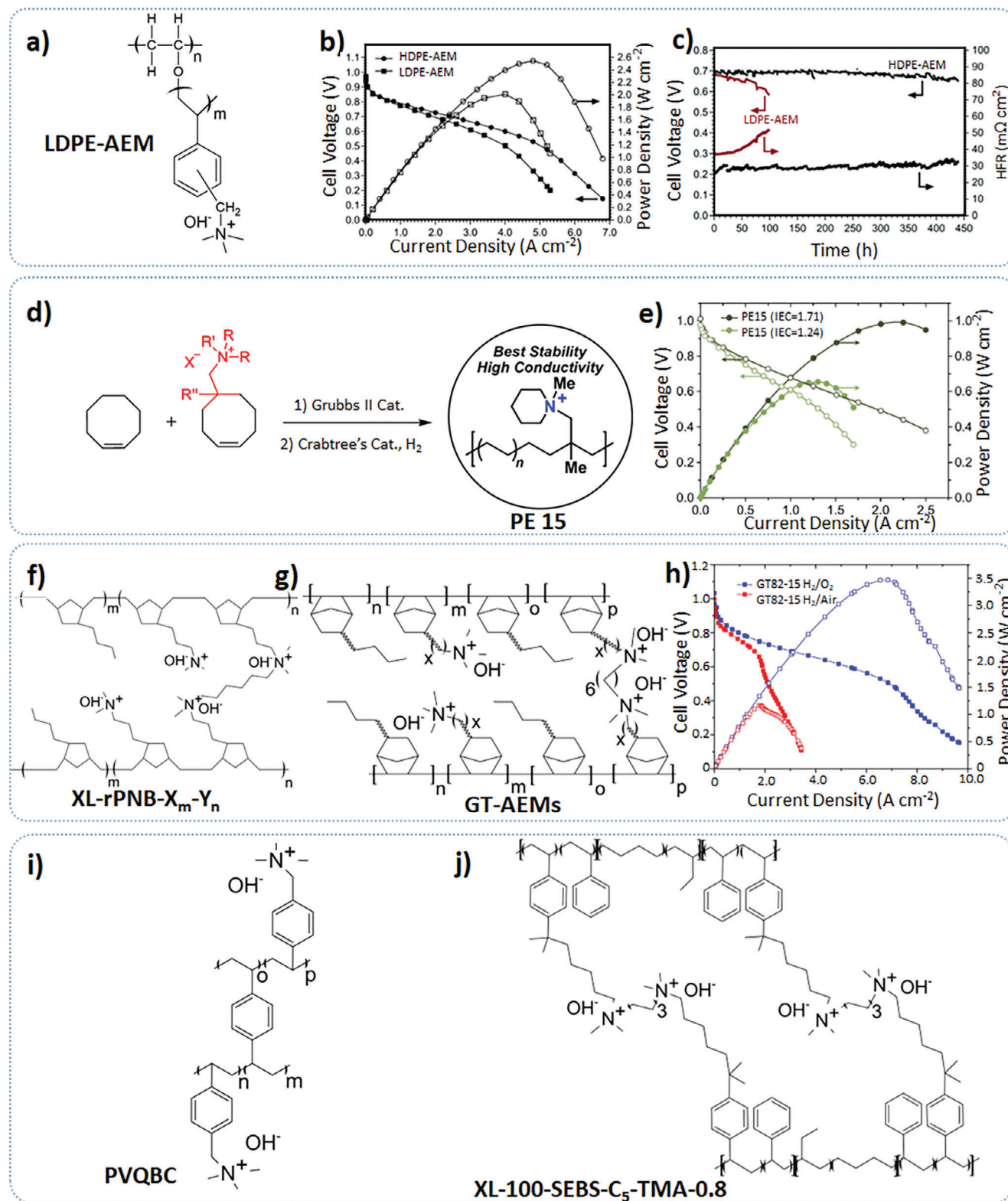
**ADVANCED
MATERIALS**

www.advmat.de

Figure 12. a) Chemical structure of LDPE-AEM; Reproduced under terms of the CC-BY license.[135d] Copyright 2017, The Authors, published by the Royal Society of Chemistry. b) H_2/O_2 AEMFCs tests of HDPE-AEM and LDPE-AEM; Test conditions: PtRu/C anode (0.40 mg_{Pt} cm^{-2}) and Pt/C cathode (0.40 mg_{Pt} cm^{-2}); cell temperature at 80 °C; dew points of H_2/O_2 both at 78 °C with no backpressure; Reproduced under terms of the CC-BY license.[135d] Copyright 2017, The Authors, published by the Royal Society of Chemistry. c) H_2/air (CO_2-free) stability tests of the AEMFCs equipped with LDPE-AEM and HDPE-AEM held at a constant current density of 600 mA cm^{-2}; Test conditions: Pt/C anode (0.60 mg_{Pt} cm^{-2}) and Pt/C cathode (0.60 mg_{Pt} cm^{-2}); cell temperature at 70 °C; dew points of H_2/O_2 both at 68 °C with 0.08 MPa backpressure; Reproduced under terms of the CC-BY license.[68a] Copyright

**ADVANCED
SCIENCE NEWS**

www.advancedsciencenews.com

**ADVANCED
MATERIALS**

www.advmat.de

LDPE-AEMs were exposed to a higher dose of electron beam absorption than that of ETFE-AEM (100 kGy vs 30 kGy), leading to a high degree of grafting. Compared to the ETFE-AEMs, the LDPE-AEMs were exhibiting excellent IEC as well as ionic conductivity, improved mechanical properties, longer stability in alkaline aging tests, and most importantly, better AEMFCs performance at higher cell temperature (80 °C).

As the thickness of AEMs plays a vital role in ohmic resistance and mechanical strength of the MEAs in AEMFC, two LDPE-AEMs with different thicknesses were synthesized by using 15 and 25 μm LDPE films (denoted as LDPE15-AEM and LDPE25-AEM). The LDPE15-AEM displayed a dehydrated thickness of 22 μm, IEC of 2.54 mmol g^{-1}, water uptake of 149% and OH$^-$ conductivity of 208 mS cm^{-1}. The LDPE25-AEM exhibited a dehydrated thickness of 45 μm, IEC of 2.87 mmol g^{-1}, water uptake of 104%, and OH$^-$ conductivity of 145 mS cm^{-1}.[135g] In H$_2$/O$_2$ AEMFC tests, the MEA with LDPE15-AEM sandwiched between the PtRu/C anode and the Pt/C cathode has yielded a peak power density of 2.02 W cm^{-2} at 80 °C, while the MEA containing LDPE25-AEM has attained a value of 1.35 W cm^{-2} under identical conditions. The improved electrochemical performance of the thinner LDPE15-AEM is attributed to the membrane's lower internal ohmic resistance (r = 35 mΩ cm^{-2} for LDPE15-AEM *cf.* 49 mΩ cm^{-2} for LDPE25-AEM) and rapid H$_2$O transport from the anode to the cathode.

The research on sub-30 μm RG-AEMs shifted to high-density polyethylene (HDPE) based AEMs (HDPE-AEM) aiming at solving the modest tensile strength of the LDPE-based AEMs.[68a] The grafting method of HEPE-AEMs is similar to that of LDPE-AEMs. The HDPE-AEM exhibited a dehydrated thickness of 21 μm, IEC of 2.44 mmol g^{-1}, water uptake of 155%, and OH$^-$ conductivity of 214 mS cm^{-1}, comparable to the LDPE15-AEM. However, the mechanical properties differ for the HDPE-AEM and the LDPE-AEM, whose fracture stresses were 35 MPa and 23 MPa, respectively. The H$_2$/O$_2$ AEMFC performances of the two membranes are also different. The peak power density achieved for the HDPE-AEM was 2.55 W cm^{-2} at 80 °C, representing a significant improvement compared to 2.02 W cm^{-2} for the LDPE-AEM (Figure 12b). The authors suggested that this improvement of HDPE-AEM is due to the enhanced water transport from the anode and cathode offered by the distinctive microstructure of the AEM. The stability tests in H$_2$/air (CO$_2$-free) AEMFCs conducted at 70 °C showed distinct results for these two membranes. The HDPE-AEM could operate at the current density of 600 mA cm^{-2} for over 440 h with a mere 7% voltage degradation. On the contrary, the LDPE-AEM couldn't complete the stability test and degraded rapidly within 100 h, which was

associated with an increase in the insitu area-specific resistance (Figure 12c).

Ziegler-Natta polymerization was adopted by Hickner and coworkers to synthesize poly(olefin)-based AEMs with quaternary ammonium cationic groups on side chains and PE-backbone.[136a] The as-synthesized membrane was named M20C9NM5NC5N with a hydroxide conductivity of 201 mS cm^{-1} at 80 °C ascribed to its phase separation in the triple-cation structure. In the AEMFC test, M20C9NM5NC5N reached peak power densities of 1.28 W cm^{-2} under H$_2$/O$_2$ and 0.78 W cm^{-2} under H$_2$/air (CO$_2$-free) at 70 °C.

To improve the stability of poly(olefin)-based AEMFC, the same research group used fluorine substitution on the aromatic comonomer via a one-pot Ziegler-Natta polymerization to obtain a fluorinated poly(olefin)-based AEM, i.e., F20C9N.[103c] The F20C9N showed higher dimensional stability than its non-fluorinated counterparts and a hydroxide conductivity of 91 mS cm^{-1} at 80 °C. In the AEMFC test, F20C9N achieved a peak power density of 1.01 W cm^{-2} at 60 °C under H$_2$/O$_2$. The stability test of F20C9N showed 11% voltage loss during the first 20 h and a voltage loss rate of 0.2 mV h^{-1} over the after 100 h test.

Compared to Ziegler-Natta polymerization, the ROMP method also synthesizes PE-based AEMs with border monomer choices, like cyclooctadiene derivatives. Coates and coworkers synthesized a series of PE-based AEMs with quaternary ammonium cationic groups by ROMP and put them into AEMFC tests (Figure 12d).[137d] Among the as-synthesized PE-based AEMs, the AEM (PE15) with piperidinium-substitution and a β-methyl in the backbone showed a 95% conductivity retention after 720 h in 1 mol L^{-1} KOH at 80 °C. This conductivity retention was ascribed to the β-methyl, blocking the potential Hofmann elimination. The hydroxide conductivity of PE15 was 68 mS cm^{-1} at 80 °C. In the AEMFC test, the PE15 achieved a peak power density of 1.00 W cm^{-2} under H$_2$/O$_2$ at 80 °C (Figure 12e).

Polynorbornene (PNB)-Based AEP: Two main synthesis methods, for PNB-based AEPs are the ROMP method and the vinyl addition polymerization method. The ROMP method is a straightforward method that uses the high ring strain of norbornene to polymerize with norbornene derivatives as monomers, resulting in PNB-based AEPs.[129,138] Chen et al. synthesized a series of ROMP cross-linked poly(norbornene)s with quaternary ammonium cationic groups using butyl norbornene (BuNB) and bromopropyl norbornene (BPNB) as monomers to form the poly(BuNB-b-BPNB) diblock copolymer.[138a] A cross-linking step was adopted to control the water uptake and improve mechanical instability. The resulting AEM, XL35-rPNB-X$_{60}$-Y$_{40}$ (Figure 12f), exhibited an OH$^-$ conductivity of 109 mS cm^{-1} at 80 °C and

---

2019, the Authors, published by the Royal Society of Chemistry. d) Synthesis of quaternary ammonium-functionalized polyethylene AEM (PE15) via the ring-opening metathesis copolymerization; Reproduced with permission.[137d] Copyright 2023, American Chemical Society. e) H$_2$/O$_2$ AEMFC tests of PE-15 AEMs with two IECs; Test conditions: PtRu/C anode (0.40 mg cm^{-2}) and Pt/C cathode (0.40 mg$_{Pt}$ cm^{-2}); cell temperature at 80 °C; dew points of H$_2$/O$_2$ both at 80 °C with 0.20 MPa backpressure; Reproduced with permission.[137d] Copyright 2023, American Chemical Society. f) Chemical structure of XL-rPNB-X$_m$-Y$_n$; Reproduced with permission.[138a] Copyright 2019, American Chemical Society. g) Chemical structure GT series AEMs with blocked structure; Reproduced under terms of the CC-BY license.[23] Copyright 2019, The Authors, published by The Electrochemical Society. h) Polarization and power density curves of AEMFCs equipped with GT82-15 membrane under H$_2$/O$_2$ (blue) and H$_2$/air (CO$_2$-free) (red); Test conditions: PtRu/C anode (0.70 mg$_{PtRu}$ cm^{-2}) and Pt/C cathode (0.60 mg$_{Pt}$ cm^{-2}); cell temperature at 80 °C; dew points at 66/75 °C (H$_2$/O$_2$) and 70/78 °C (H$_2$/air (CO$_2$-free)) with 0.20 MPa backpressure; Reproduced under terms of the CC-BY license.[23] Copyright 2019, The Authors, published by The Electrochemical Society. i) Chemical structure of PVQBC; Reproduce with permission.[141] Copyright 2020, Elsevier. j) Chemical structure of XL-100-SEBS-C$_5$-TMA series MEA; Reproduce with permission.[143a] Copyright 2019, American Chemical Society.

**ADVANCED
SCIENCE NEWS**

www.advancedsciencenews.com

**ADVANCED
MATERIALS**

www.advmat.de

a high IEC of 4.73 meq. g^{-1}, with 100% water uptake and 28% swelling ratio. In the AEMFC test, the XL35-rPNB-X$_{60}$-Y$_{40}$ reached a peak power density of 0.17 W cm^{-2} and an open-circuit voltage of 0.83 V at 60 °C.

The vinyl addition polymerization method is another metal-catalyzed vinyl addition polymerization approach for synthesizing PNB-based AEPs.[23,139] Recently, Kohl and co-workers developed PNB-based tetrablock copolymers.[23] The authors polymerized BuNB, BPNB, and bromopropyl norbornene with the vinyl addition polymerization method and employed a cross-linking agent, *N,N,N′,N′*-tetramethyl-1,6-hexanediamine (TMHDA), as polymer reinforcement. The as-synthesized polymer, GT82-15 (with 82% halogenated monomer content and 15% TMHDA relative to the number of head groups) showed an IEC of 3.76 meq. g^{-1} and an OH$^-$ conductivity of 147 mS cm^{-1} at 80 °C. In H$_2$/O$_2$ AEMFC testing, the GT82-15 membrane demonstrated a peak power density of 3.50 W cm^{-2} at 80 °C, attributed to optimized water permeability in the polymer matrix, enhanced water transport, and reduced ohmic resistance due to the thin GT82-15 (10 µm, Figure 12g). Stability tests of the GT82-15 membrane indicated no significant voltage loss measured at a constant current density of 600 mA cm^{-2} under H$_2$/air (CO$_2$-free) for over 100 h (Figure 12h).

Polystyrene (PS)-Based AEP: PS, a commercially available polymer, is often converted into PS-based AEPs via chloromethylation followed by quaternization to introduce cationic groups. Due to the limited mechanical properties of pure PS-based polymers, copolymerization with soft polymers and polymer blending strategies are commonly employed to improve their performance. Wei and coworkers developed an interpenetrating polymer network (IPN) comprising quaternized poly(vinylbenzyl-N-methyl piperidinium) (PVBMP) and crosslinked poly(vinyl alcohol) (PVA), forming a series of PVA-PVBMP AEPs.[140] The PVA-1.8PVBMA (PVBMA: PVA = 1.8 w/w) showed an OH$^-$ conductivity of 203 mS cm^{-1} at 80 °C and an IEC of 1.62 mmol g^{-1}. In H$_2$/O$_2$ AEMFC testing, this AEM reached a peak power density of 1.20 W cm^{-2} at 60 °C, attributed to the microphase segregation in the membrane, which formed ion channels that facilitate ion conduction.

A similar IPN structure was applied to synthesize quaternized poly(vinylbenzyl chloride) (PQVBC, Figure 12i) crosslinked with poly(vinyl alcohol) (PVA) to obtain PVA-PQVBC AEPs, which also displayed microphase segregation.[141] The PVA-0.8PQVBC$_{40\%}$ membrane demonstrated an OH$^-$ conductivity of 98 mS cm^{-1} at 80 °C with an IEC of 1.50 mmol g^{-1}. In H$_2$/Air (CO$_2$-free) AEMFC testing, this membrane reached a peak power density of 0.64 W cm^{-2} at 60 °C.

Recently, an ultrathin (4 µm) PS-based composite AEM was developed using an ultrahigh molecular weight polyethylene (UHMWPD)-porous membrane as a support, with in-situ polymerization of 4-vinylbenzylchloride (VPC).[142] The UHMWPD-VPC-AEM demonstrated an OH$^-$ conductivity of 101 mS cm^{-1} at 80 °C with an IEC of 1.51 mmol g^{-1}. In AEMFC testing, the membrane exhibited peak power densities of 1.01 W cm^{-2} (H$_2$/O$_2$)) and 0.53 W cm^{-2} (H$_2$/Air (CO$_2$-free)) at 65 °C, due to significantly decreased ohmic internal resistance. In the short-term AEMFC stability test, the UHMWPD-AEM showed a voltage loss of only 2.8% after 10 h at a constant current density of 300 mA cm^{-2} under H$_2$/O$_2$ at 65 °C.

Poly(styrene-ethylene-co-butylene-styrene) (SEBS), a commercially available elastomeric triblock copolymer with PS blocks, is often used in AEP synthesis through methods such as chloromethylation, C-H borylation, Suzuki coupling reaction, and Friedel-Crafts acylation.[143] SEBS generally contains 20–40 wt.% PS, as it was initially designed as a thermoplastic elastomer.[144]

Bae and coworkers synthesized SEBS-based AEP via acid-catalyzed Friedel-Crafts alkylation of the PS blocks in SEBS, followed by amination with trimethylamine.[143a] To optimize water uptake and enhance mechanical properties, the as-synthesized AEP was crosslinked using TMHDA. The resulting membrane, XL-100-SEBS-C$_5$-TMA-0.8, with 100% cross-linking degree, 5-carbon tether chain, and 0.8 mol% functionalization degree (Figure 12h), demonstrated an OH$^-$ conductivity of 65 mS cm^{-1} at 80 °C with an IEC of 1.50 meq. g^{-1}. In H$_2$/O$_2$ AEMFC tests, with this membrane, the fuel cell achieved a peak power density of 0.52 W cm^{-2} at 60 °C.

Gao et al. investigated the effects of different diamine crosslinkers (TMEDA, TMBDA, TMHDA) on SEBS-based AEPs.[145] The C4-CAQSEBSAEP, synthesized with TMBDA (*N,N,N′,N′*-tetramethyl-1,4-butanediamine) with chloromethylated SEBSs, showed the highest OH$^-$ conductivity (16 mS cm^{-1} at 30 °C with an IEC of 1.35 mmol g^{-1}) among as-synthesized membranes. In H$_2$/O$_2$ AEMFC testing, this membrane reached a peak power density of 0.56 W cm^{-2} at 60 °C, with proper chain length of the crosslinker helping to construct a microphase-separated structure that facilitated ion conduction.

A higher percentage of PS block in SEBS was synthesized to increase the IEC of the synthesized SEBS-based AEPs; however, this often leads to a reduction in mechanical properties. Huang et al. synthesized SEBS with higher PS contents (51, 62, and 71 wt.%) labeled as OH-SEBS-50, 60, and 70.[144b] The OH-SEBS-70 membrane showed an OH$^-$ conductivity of 190 mS cm^{-1} at 80 °C with an IEC of 3.37 mmol g^{-1}, a water uptake of 156%, and a swelling ratio of 56% at 80 °C. In H$_2$/O$_2$ AEMFC testing, this membrane reached a peak power density of 1.01 W cm^{-2} at 80 °C, with the higher PS content contributing to the formation of large-volume ion transport channels.

The Suzuki coupling reaction was also employed to modify SEBS-based AEPs by introducing benzyltrimethylammonium groups to the styrene blocks (SEBS-TMA), resulting in an OH$^-$ conductivity of 89 mS cm^{-1} at 60 °C with an IEC of 2.41 meq. g^{-1}.[143b] SEBS-TMA exhibited no degradation of cationic functional groups after 672 h in 1 mol L^{-1} NaOH at 80 °C. In H$_2$/O$_2$ AEMFC tests, it reached a peak power density of 0.24 W cm^{-2} at 80 °C and maintained stable functional groups after 100 h at a constant voltage of 0.3 V at 60 °C.

4.2. AEM-properties-Enhancing Strategies

In addition to using different kinds of cationic groups and polymer backbones, other strategies can also be applied to enhance the conductivity and mechanical properties of the AEMs. Constructing a microphase segregated structure[17,26,146] and reinforcement with cross-linking[139a,b,147] are the two ways that were studied the most. Besides, the organic-inorganic composite is

**ADVANCED
SCIENCE NEWS**

www.advancedsciencenews.com

**ADVANCED
MATERIALS**

www.advmat.de

also a promising and efficient way to enhance the properties of AEM.[148]

The development of phase-segregated structures is one of the potential strategies to increase the ionic conductivity of AEMs by forming ionic channels in the membrane matrix.[17,146a,b] Usually, the ionic clusters are randomly dispersed in the hydrophobic matrix of AEMs. However, when additional hydrophobic side chains are introduced into the matrix, they dynamically assemble to form hydrophobic and hydrophilic ionic domains that promote ion conduction in hydrated conditions. Nevertheless, when ionic domains over-aggregate, the macroscopic uniformity of the AEMs breaks, decreasing the membrane's mechanical properties (**Figure 13a**).[17]

Quaternary ammonia polysulfone (QAPS, Figure 11a) based membranes possessing the aforementioned aggregating structure were synthesized with various side-chain lengths to tune the degree of aggregation (aQAPS-S_x), as shown in Figure 13b.[17] In aQAPS-S_x with three site-chain lengths of 6, 8, or 14 ("x"). The aggregating structure was characterized by small-angle X-ray scattering patterns, which showed that the X-ray scattering peak corroded the microphase structure. The IEC for the series of aQAPS-S_x membranes is ca. 1.00 mmol g^{-1}. In the ionic conductivity tests, aQAPS-S_8 showed a comparable ionic conductivity to Nafion™ 112 and even better when the testing temperature was above 70 °C. The aQAPS-S_8 was also examined in the H$_2$/O$_2$ AEMFCs with PtRu/C as the anode and Pt/C as the cathode catalysts, respectively. A peak power density of 1.00 W cm^{-2} at 60 °C was achieved.[13]

A similar microphase segregated structure was achieved by covalent assembly AEM with charge-delocalized pyrazolium cations and homoconjugated triptycenes by Kim et al., denoted as PX75-T50, in which 75 denoted the intended percent of cross-linking, and the 50 denoted the percent of triptycene repeating sides in the polymer.[146c] The authors indicated that the covalent assembly of repeating ionic segments hosted the delocalized cationic charges and served as an ionic highway. The activation barriers of ion transport were lowered to increase the ionic conductivity (Figure 13c). The OH$^-$ conductivity of PX75-T50 was 112 mS cm^{-1} at 80 °C. In the H$_2$/O$_2$ AEMFC test, a single cell with PX75-T50 reached a peak power density of 0.73 W cm^{-2} and operated for 400 h at 80 °C and a constant current density of 400 mA cm^{-2} with 10% voltage loss.

The cross-linking method can decrease the membrane's swelling degree and water uptake and enhance the mechanical properties of the membranes because of the formation of a cross-linking network in the membrane.[149] Using block copolymers (BCP), Kohl's group synthesized composite AEMs composed of three-block copolymers of poly(norbornene), butyl norbornene, and bromopropyl norbornene with pendant QA head groups.[139a,b,147] In addition, the prepared AEMs were reinforced with a layer of polytetrafluoroethylene (PTFE) on their surface. A light crossing-linking was also accomplished by adding a cross-linking agent, TMHDA. The optimized membrane with 15 mol % TMHDA (XL 15) displayed an IEC value of 3.28 meq. g^{-1}, OH$^-$ conductivity of 198 mS cm^{-1}, and water uptake of 29%.[147] In the H$_2$/O$_2$ AEMFC test, the cell prepared with an XL 15 membrane reached a peak power density of 3.37 W cm^{-2} at 80 °C and an optimized anode/cathode dew point of 68/75 °C (Figure 13d). Further,

the AEMFC showed a stable operation at 80 °C under H$_2$ and CO$_2$-free air for 545 h, without noticeable membrane degradation.

Jeon et al. synthesized a series of polystyrene-*b*-poly(ethylene-*co*-butylene)-*b*-polystyrene (SEBS)-based AEMs with microphase-separated morphology and crosslinking feature.[143a] After crosslinking, the water uptake decreased significantly (155% vs 28%) while the mechanical properties were enhanced. The highest OH$^-$ conductivity of the as-synthesized SEBS-based AEMs was 93 mS cm^{-2} at 80 °C. The H$_2$/O$_2$ AEMFC test showed a peak power density of 0.52 W cm^{-2} reached at 60 °C with XL100-SEBS-C$_5$-TMA-0.8 membrane.

Block polymers have also been developed to create microphase-segregated structures and improve mechanical properties.[23,30,139a] For example, a tetrablock copolymer AEM with PNB-based backbone, synthesized with the vinyl addition polymerization method, was named PNB-X$_{62}$-Y$_{38}$, where X$_{62}$ and Y$_{38}$ represent the mole percentages of combined hydrophobic and hydrophilic blocks, respectively. This polymer demonstrated microphase segregation with an OH$^-$ conductivity of 123 mS cm^{-1} at 80 °C and an IEC of 1.88 meq. g^{-1}.[139a] In terms of alkaline stability, PNB-X$_{62}$-Y$_{38}$ showed no detectable degradation after testing in 1 mol L^{-1} NaOH at 80 °C for 1200 h, and reached a peak power density of 0.54 W cm^{-2} in an H$_2$/O$_2$ AEMFC at 60 °C.

Branched polymers have also exhibited microphase-segregated morphologies with improved mechanical properties. Lui et al. developed branched polymers incorporating flexible segments to enhance chain entanglement, achieving an OH$^-$ conductivity of 85 mS cm^{-1}, higher than the linear counterpart (15 mS cm^{-1}) at 80 °C.[150] Recent branched AEMs using 1,3,5-triphenylbenzene (TPB) as a branching agent demonstrated stable mechanical properties, microphase-segregated morphology, high OH$^-$ conductivity and alkaline stability.[34,116b,151] The branched AEM qPBPTT-5, synthesized with TPB, biphenyl, N-methy-l-4-piperidone, and 1,1,1-trifluoroacetone, exhibited an OH$^-$ conductivity of 117 mS cm^{-1} at 80 °C (IEC of 1.93 mmol g^{-1}), notably higher than its linear counterpart (64 mS cm^{-1}) due to its microphase-segregated structure.[151a] The qPBPTT-5 retained 87% of its initial conductivity after immersing in 1 mol L^{-1} NaOH at 80 °C for 480 h and achieved a peak power density of 0.28 W cm^{-2} at 60 °C in H$_2$/O$_2$ AEMFC testing.

Wu et al. synthesized the branched poly(terphenyl piperidinium) AEMs (b-PTP-2.5) using TPB as a branching agent, achieving an OH$^-$ conductivity of 147 mS cm^{-1} (ICE of 2.81 mmol g^{-1} at 80 °C) and a reduced swelling ratio of 26%, compared to 138 mS cm^{-1} and 33%, respectively, for the linear counterpart.[151b] The Alkaline stability test of b-PTP-2.5 showed no chemical degradation after soaking in 1 mol L^{-1} KOH for 1500 h. In AEMFC testing, b-PTP-2.5 demonstrated a peak power density of 2.30 W cm^{-2} in H$_2$/O$_2$ and 1.30 W cm^{-2} in H$_2$/air (CO$_2$-free) at 80 °C with operation at a constant current density of 200 mA cm^{-2} for 500 h at 60 °C, showing a voltage drop from 0.68 to 0.51 V. The similar branched AEM, poly(aryl-quinuclidinium), with quinuclidinium cationic groups, synthesized by Yin et al., displayed an OH$^-$ conductivity of 187 mS cm^{-1} at 80 °C with an IEC of 2.65 mmol g^{-1} and retained 97% of its initial OH$^-$ conductivity after immersing in 1 mol L^{-1} KOH at 80 °C for 2500 h.[116b]

**ADVANCED
SCIENCE NEWS**

www.advancedsciencenews.com

**ADVANCED
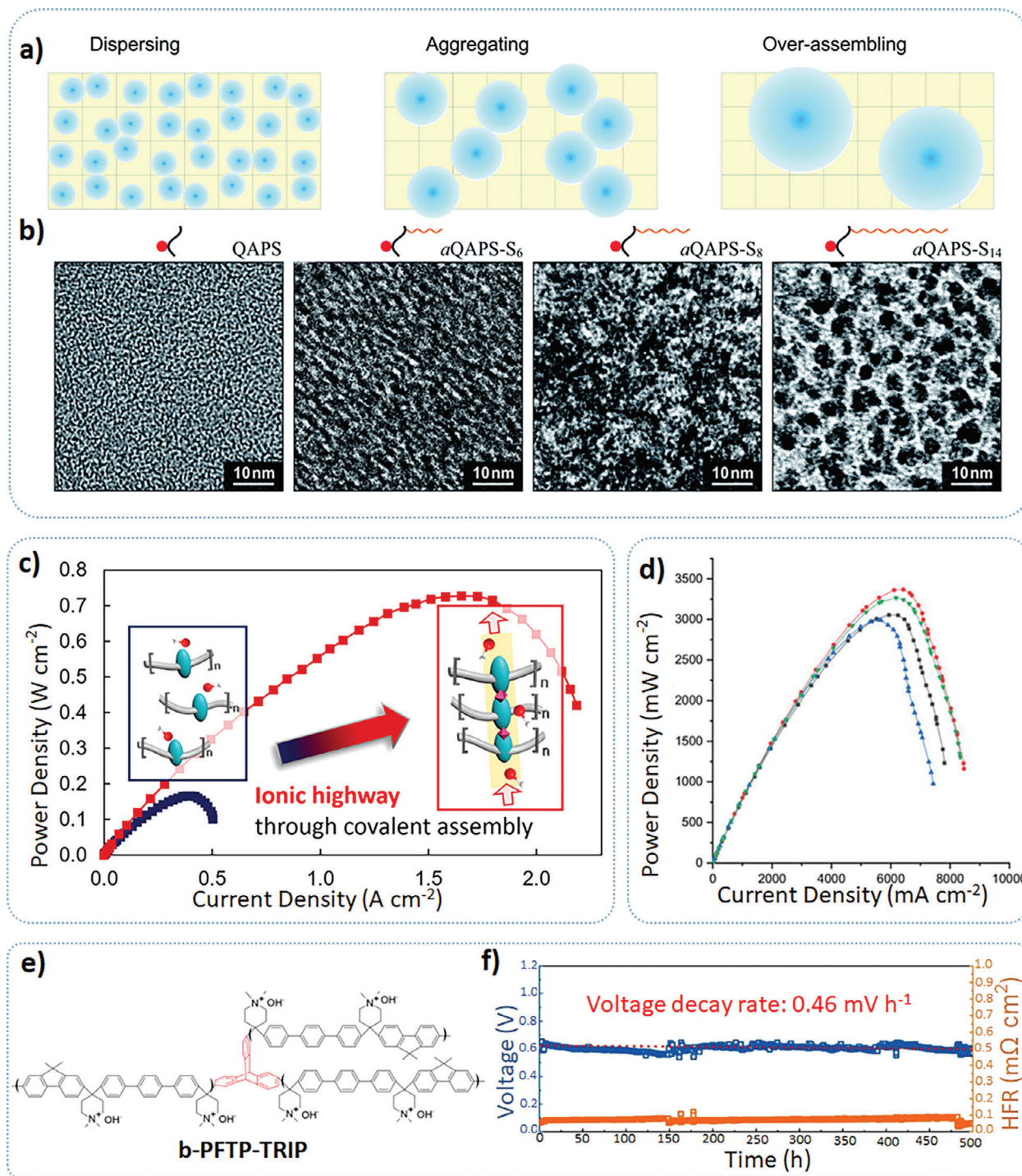MATERIALS**

www.advmat.de

Figure 13. a) Schematic diagrams of the formation of segregated ionic clusters (blue) in a hydrophobic matrix (yellow) of QAPS with the corresponding; Reproduced with permission.[17] Copyright 2014, the Royal Society of Chemistry. b) TEM images of different side chain lengths; Reproduced with permission.[17] Copyright 2014, the Royal Society of Chemistry. c) Schematic (two insets) for without/with ion highway by covalent assembly method and H_2/O_2 AEMFC power density curves for PX75-T50 (red) and reference (black); Test conditions: PtRu/C anode (0.50 mg_{Pt} cm^{-2}) and Pt/C cathode (0.50 mg_{Pt} cm^{-2}); cell temperature at 80 °C; dew points at 80/80 °C with no backpressure; Reproduced with permission.[146c] Copyright 2019, American Chemical Society. d) Cell polarization curves of poly(norbornene) AEMs with different cross-linking concentrations (XL mol%); Test conditions: PtRu/C anode (0.70 mg_{PtRu} cm^{-2}) and Pt/C cathode (0.60 mg_{Pt} cm^{-2}); cell temperature at 80 °C; the anode dew points, and the cathode dew points are given in the figure; Reproduced with under terms of the CC-BY license.[147] Copyright 2019, The Authors, published by The Electrochemical Society. e) Structure of branched b-PFTP-TRIP AEM; Reproduced with permission.[34] Copyright 2023, John Wiley and Sons. f) Stability test of branched b-PFTP-TRIP AEM Test conditions: Pt/C anode (0.67 mg_{Pt} cm^{-2}) and Pt/C cathode (0.67 mg_{Pt} cm^{-2}); cell temperature at 70 °C; dew points at 67/69 °C; Reproduced with permission.[34] Copyright 2023, John Wiley and Sons.

**ADVANCED
SCIENCE NEWS**

www.advancedsciencenews.com

**ADVANCED
MATERIALS**

www.advmat.de

Moving beyond planar structures like TPB, the highly rigid, three-dimensional triptycene (TRIP) has been introduced as a branching agent to increase the membrane free volume and enhance ion transport in branched poly(aryl-co-aryl piperidinium) AEMs.[151c,152] TRIP-branched poly(dibenzyl-co-terphenyl piperidiniums) (b-PDTP-TRIPs, Figure 13e), synthesized by Hu et al., showed similar IECs, lower swell ratios (SR), and enhanced ion conductivity (σ) compared to their linear analogs.[34] For instance, b-PDTP-TRIP-5 achieved an IEC of 2.95 mmol g^{-1}, an SR of 23%, and a conductivity of 100 mS cm^{-1}, outperforming the linear PDTP (2.89 mmol g^{-1} IEC, 30% SR, 79 mS cm^{-1} σ) due to its microphase-segregated structure. When comparing branched AEMs with TPB and TRIP agents, b-PDTP-TRIP-5 showed superior conductivity, attributed to its higher fractional free volume and rigidity. The b-PFTP-TRIP-5 MEA retained 90% of its cations after soaking in 5 mol L^{-1} NaOH for 1000 h. In H$_2$/O$_2$ AEMFC testing, b-PFTP-TRIP-5 reached a peak power density of 2.50 W cm^{-2} at 80 °C, surpassing the TPB-branched AEM (1.10 W cm^{-2}), due to enhanced water permeability. In the AEMFC stability test, b-PFTP-TRIP-5 operated at a constant current density of 600 mA cm^{-2} at 70 °C, with a voltage decay rate of 0.46 mV h^{-1} for 500 h (Figure 13f).

The organic-inorganic composite strategy is also used to improve the mechanical properties of AEMs. The traditional method is the direct addition of inorganic materials, like SiO$_2$,[148a] TiO$_2$,[148e] Al$_2$O$_3$,[148b] etc., in a polymer solution as fillers to produce organic-inorganic composite AEMs. After decomposing with inorganic fillers, the mechanical properties are enhanced, while the ionic conductivity is reduced.[148h] The AEMFC tests with organic-inorganic membranes are limited.

4.3. Anion Exchange Ionomers and Constructing a Triple-phase Boundary

Anion exchange ionomers (AEIs) in fuel cells are commonly employed as binders and ion conductors in the electrodes to form the triple-phase boundary (TPB), the interface of catalysts, membranes, and gas diffusion regions.[153] During the formation of TPB, favorable porous structures in the catalyst layer need the participation of AEIs to enhance ion and reactant transport to the active sites. AEIs need long durability, even at elevated temperatures and high current densities, to ensure high-performance AEMFCs.[154]

The AEIs used in AEMFCs are usually prepared by dissolving or dispersing the AEPs in low-boiling point solvents, then they are mixed with the catalyst materials to form the catalyst ink. Afterward, the ink is used to fabricate the catalyst layers in the MEAs.[68b,155] This catalyst layer preparation method calls for the AEIs to have different requirements than AEMs. Firstly, similarly to AEMs, AEIs are required to possess high ionic conductivity and alkaline stability with high chemical and mechanical strengths. Secondly, the solubility or the dispersibility of AEIs are different compared to the AEMs. Desirable AEIs are expected to mix homogeneously with low-boiling solvents and catalysts to form the TPB. Thirdly, the ideal AEIs should have minimal reactivity with the catalysts, such as the adsorption effect, to avoid poisoning or covering the active sites.

The development of the AEIs chemistry is similar to that of AEMs, which is from aryl-ether AEIs to aryl-ether-free AEIs, and the most commonly used cationic group is the QA group (**Table 4**). There are several AEIs available in the commercial market, including Fumion (Fumatech Corporation), Sustainion (Dioxide Materials), A3 (Tokuyama), and PiperION (Versogen).[7d,100a]

A typical aryl-ether backbone with quaternary phosphonium-based AEI was synthesized by Gu et al. in 2009.[156] The ris(2,4,6-trimethoxyphenyl) polysulfone-methylene quaternary phosphonium hydroxide (TPQPOH) AEI had good dispersion ability in low-boiling-point solvents (e.g., methanol and n-propanol). The OH$^-$ conductivity of TPQPOH was 27 mS cm^{-1}, and the IEC was 1.09 mmol g^{-1}. The H$_2$/O$_2$ AEMFC test with TPQPOH ionomer achieved a peak power density of 0.20 W cm^{-2} at 80 °C with the FAA commercial membrane.

Aryl-ether-free AEIs are the better choice because aryl-ether cleavage reactions are absent.[102] Radiation-grafting technology is a method that can be used to synthesize aryl-ether-free AEIs.[16,157] Ponce-González et al. used vinylbenzyl chloride (VBC) grafted onto poly(ethylene-co-tetrafluoroethylene) (ETFE) powder after exposing the ETFE powder to radiation, followed by submerging in the aqueous trimethylamine solution (TMA) (**Figure 14a**).[16] After quaternization, the chemical properties of ETFE-AEI were similar to that of ETFE-based radiation-grafted AEMs (ETFE-AEM, as discussed above) with an IEC value of 1.24 meq. g^{-1} and water uptake of 155%. The average particle size of ETFE-AEI was 24.5 µm for the dehydrated particles, and the minimum and maximum sizes were 6 and 75 µm, respectively (SEM images shown in Figure 14b,c). The H$_2$/O$_2$ AEMFC test with ETFE-AEI achieved a peak power density of 0.24 W cm^{-2} with ETFE-AEM at 50 °C. After optimizing the electrode components and ratio between AEI, carbon, and metal nanoparticles, the H$_2$/O$_2$ AEMFC achieved a peak power density of 1.90 W cm^{-2} at 60 °C with the same AEI and AEM.[19] Subsequently, the ETFE-AEI combined with the as-discussed HDPE-AEM and cross-linking GT82-15 membrane reached peak power densities of 2.55 W cm^{-2} and 3.50 W cm^{-2} at 80 °C, respectively.[23,68a]

In the Lee group, a series of PFBP polymers were synthesized. The PFBP-14 AEI produced the highest peak power density because of the lower phenyl adsorption in poly(biphenyl)-based ionomers compared to poly(terphenyl)-based ionomers.[25] Also, the water uptake was moderate, so the water back diffusion was improved, and the relative humidity of the anode was low. After optimizing the operating conditions, the H$_2$/O$_2$ AEMFC with PFBP-14 ionomer achieved a peak power density of 2.34 W cm^{-2} at 80 °C. Combined with the PDTP-25 membrane, the PFBP-14 ionomer reached a peak power density of 2.58 W cm^{-2} at 80 °C in H$_2$/O$_2$ AEMFCs.[26]

Since the ionomers are directly in contact with the catalysts, they define the environment surrounding the catalysts. The interaction between ionomers and catalysts can affect the performance of catalysts.[158] Li et al. showed that the adsorption of the phenyl group in PA-based ionomers lowered the HOR activity of Pt catalysts.[158a] Two distinctive features of the phenyl-group adsorption were pointed out. The first feature was that this was non-accumulative adsorption, which intended that the phenyl-group adsorption was physisorbed by the interaction between the
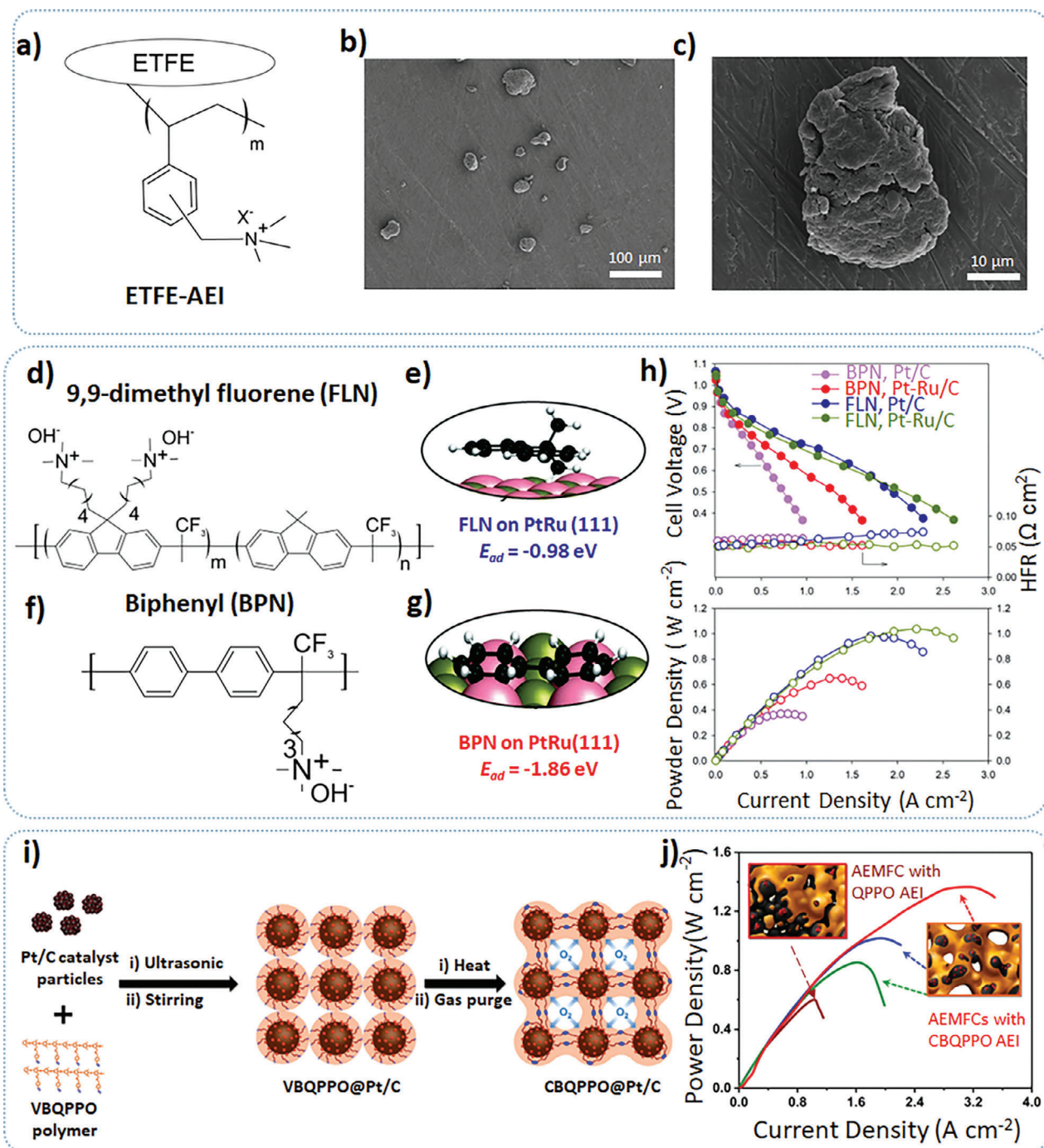
ADVANCED
SCIENCE NEWS

www.advancedsciencenews.com

ADVANCED
MATERIALS

www.advmat.de

Figure 14. a) Synthetic pathway of ETFE-based anion exchange ionomers; Reproduced under terms of the CC-BY license.[16] Copyright 2014, The Authors, published by the Royal Society of Chemistry. b,c) SEM images of the dehydrated anion exchange ETFE-based ionomers; Reproduced under terms of the CC-BY license.[16] Copyright 2014, The Authors, published by the Royal Society of Chemistry. d) Chemical structure of FLN and f) BPN ionomers; Reproduced with permission.[158d] Copyright 2018, the Royal Society Chemistry. Optimized geometries and adsorption energy of e) FLN and g) BPN on PtRu(111). Pink: Ru, tan: Pt, black: C and white: H; Reproduced with permission.[158d] Copyright 2018, the Royal Society Chemistry. h) Power density curves of H_2/O_2 AEMFC tests with FLN and BPN ionomers; Test conditions: PtRu/C anode (0.60 mg_{Pt} cm^{-2}) or PtRu/C anode (0.50 mg_{Pt} cm^{-2}), and Pt/C cathode (0.60 mg_{Pt} cm^{-2}); cell temperature at 80 °C; dew points of anode and cathode both at 80 °C with 0.29 MPa backpressure; Reproduced with permission.[158d] Copyright 2018, the Royal Society Chemistry. i) Schematic representation of synthesis and crosslinking process of CBQPPO ionomers; Reproduced with permission.[160a] Copyright 2019, American Chemical Society. j) H_2/O_2 AEMFC tests of two QPPO and CBQPPO ionomers under different conditions; insets schematic illustration of the morphologies of two types of catalyst layers; Test conditions: PtRu/C anode (0.50 mg_{PtRu} cm^{-2}) and Pt/C cathode (0.50 mg_{Pt} cm^{-2}); cell temperature at 70 °C; dew points of anode/cathode at 70/70 °C (red, blue, and brown curves) or 65/65 °C (green curve) with a 0.10 MPa backpressure (red curve) or no back pressure (blue, green, and brown curves); Reproduced with permission.[160a] Copyright 2019, American Chemical Society.

ADVANCED
SCIENCE NEWS

www.advancedsciencenews.com

ADVANCED
MATERIALS

www.advmat.de

Table 4. Typical anion exchange ionomers.

Ionomer	IEC[a] [mmol g^{-1}]	OH$^-$ Conductivity @ 80 °C [mS cm^{-1}]	HOR Catalyst	HOR Catalyst Loading [mg$_{metal}$ cm^{-2}]	ORR Catalyst	ORR Catalyst Loading [mg$_{metal}$ cm^{-2}]	Membrane	Feed Gas	T$_{Cell}$ [°C]	T$_{DP}$ of Anode/Cathode [°C]	Back-pressure of Anode/Cathode [MPa]	PPD[b] [W cm^{-2}]	Refs.
TPQPOH	1.09	27 (20 °C)	Pt/C	0.5	Pt/C	0.5	FAA	H$_2$/O$_2$	80	70/80	0.25/0.25	0.20	[156]
ETFE-AEI	1.24[c]	–	Pt/C	0.4	Pt/C	0.4	ETFE-AEM	H$_2$/O$_2$	50	50/50	0/0	0.24	[16]
PFBP-14	2.86	131 (60 °C)	PtRu/C	0.39	Pt/C	0.26	PDTP-25	H$_2$/O$_2$	80	73/80	0.13/0.13	2.58	[26]
FLN-55	2.50[c]	120	PtRu/C	0.5$_{Pt}$	Pt/C	0.6	TPN	H$_2$/O$_2$	80	80/80	0.29/0.29	1.46	[158d]
QP-NB	2.50[c]	137	PtRu/C	0.5$_{Pt}$	Pt/C	0.6	HTMA-DAPP	H$_2$/O$_2$	80	80/80	0.15/0.15	1.40	[158f]
CBQPPO	–	–	PtRu/C	0.5	Pt/C	0.5	TMImPPO	H$_2$/O$_2$	70	70/70	0.10/0.10	1.02	[160a]
x-Trip-PFBP-Pr-30	3.42	97	PtRu/C	0.39	Pt/C	0.26	x-PDTP-Pr-10	H$_2$/O$_2$	80	76/80	0/0	1.02	[160b]

a) IEC: ion-exchange capacity; b) PPD: peak power density; c) in the unit of meq. g^{-1}.

aromatic π-electrons of phenyl and the electronic cloud of the metal atoms. The second feature showed that the phenyl-group adsorption affected the AEMFC performances by blocking the active sites of the catalysts. This phenyl-group surface adsorption was also observed in other HOR catalysts, including Pt/C, PtRu/C, Pd/C, and Pd/C-CeO$_2$ catalysts.[158c–e,159]

To compare the phenyl-group adsorption effect, two ionomers, namely, alkyl ammonium tethered poly(fluorine)s (FLNs, Figure 14d) and poly(biphenylene) (BPN, Figure 14e) were synthesized. The FLNs were chosen based on the hypothesis that non-rotatable phenyl-phenyl rings in the polyaromatic backbone can mitigate the phenyl group interaction with HOR electrocatalysts to avoid the ionomer poisoning effect.[158a,d] The weaker interaction of FLNs compared to BPN was asserted from the calculated adsorption energy of fluorine (−0.98 eV) and biphenyl (-0.186 eV) on Pt-Ru alloy catalysts (Figure 14f).[158d] The H$_2$/O$_2$ AEMFCs tests with FLN-55 (IEC = 2.50 meq. g^{-1}) or BPN (IEC = 2.60 meq. g^{-1}) were carried out using Pt/C or PtRu/C as HOR catalysts. The performances were consistent with the hypothesis and the calculation results of fluorine and biphenyl absorption energies on the surface of Pt and Pt-Ru. With the optimized operating conditions, among all the H$_2$/O$_2$ fuel cell tests, the single cell employing FLN-55 ionomer and PtRu/C anode attained the highest peak power density of 0.98 W cm^{-2} at 80 °C, whereas 0.67 W cm^{-2} was measured for the BPN ionomer with PtRu/C anode (Figure 14g). Finally, an H$_2$/O$_2$ AEMFC with FLN-55 ionomers demonstrated almost no degradation at 80 °C for 350 h at the constant current of 600 A cm^{-2} under fully hydrated conditions.

Leonard et al. prepared a phenyl-free polynorbornene by vinyl addition polymerization.[158f] The calculated results showed that the adsorption energies on Pt(111) of bornane were the smallest among the tested fragments, i.e., -0.58 eV and -0.64 eV in two orientations. The minimal adsorption energy of bornane originated from the absence of the aromatic π-electrons of the phenyl group and the sp^2 electrons of the double bond in norbornene. Those two types of electrons can interact with the d-electrons of metals and increase the adsorption energy. Based on the calculation results, the soluble quaternized polynorbornene (QP-NB) was synthesized and showed an OH$^-$ conductivity of 137 mS cm^{-1} at 80 °C. In the AEMFC test, QP-NB achieved a peak power density of 1.41 W cm^{-2}, higher than that of the AEMFCs with the phenyl-containing ionomer (m-TPN).

Several in-situ ionomer cross-linking approaches were adopted to enhance the AEMFC performances[160] Xu and co-workers put forward in-situ ionomer cross-linking immobilization for the MEA fabrication.[160a] Pt/C nanoparticle catalysts were immobilized by poly(2,6-dimethyl-p-phenylene oxide)-(PPO)-based quaternary ammonium(QPPO) ionomer to form porous catalyst layers by thermally triggered (70 °C) cross-linking (Figure 14h), denoted as CBQPPO. Compared to the non-cross-linking ionomer, the cross-linking ionomer catalyst layer displayed better durability in the RDE test, and the Pt agglomeration in the ionomer catalyst layer was suppressed, as evidenced in the TEM images. The H$_2$/O$_2$ AEMFC test revealed that the cell employed with a cross-linking ionomer with PtRu/C as the anode and Pt/C as the cathode catalysts reached a peak power density of 1.02 W cm^{-2} at 70 °C without back-pressure (Figure 14i). The cell stability test also showed that the

cross-linking ionomer improved the AEMFC stability compared to the non-cross-linking counterpart. This can be attributed to the immobilization of catalyst nanoparticles and pores in the catalyst layer.

Similarly, the in-situ crosslinking strategy was further applied to construct covalent bonds between ionomers and membranes to enhance the catalyst layer stability. Hu et al. incorporated a thermally induced cross-linking group, propargyl, into both ionomer and membrane structures, improving catalyst layer adhesion strength (0.395 N mm^{-1}) up to 7 times, compared to the non-crosslinked counterpart ($\approx$0.055 N mm^{-1}).[160b] Crosslinking also reduced ionomer leaching in alkaline media, which was believed to mitigate the Pt nanoparticle aggregation during the RDE tests. Using the ionomer, x-Trip-PFBP-Pr-30 (OH$^-$ conductivity of 97 mS cm^{-2} at 80 °C with IEC of 3.42 mmol g^{-1}), and the membrane, x-PDTP-Pr-10 (OH$^-$ conductivity of 150 mS cm^{-2} at 80 °C with IEC of 2.87 mmol g^{-1}), and combining them with the in-situ cross-linking strategy between ionomer and membrane, the MEA achieved a peak power density of 1.02 W cm^{-2} in H$_2$/O$_2$ AEMFC test without backpressure at 80 °C. H$_2$/O$_2$ stability tests revealed a significant improvement for the in-situ crosslinked MEA compared to the non-crosslinked MEA, showing a voltage drop rate of 0.02 mV h^{-1} vs 6.2 mV h^{-1}, which can be attributed to the crosslinking.

4.4. Stability of Anion Exchange Polymers in AEMFCs

This section summarizes representative studies on the stability of AEM under fuel cell conditions. Typical stability tests for AEPs in AEMFCs use galvanostatic methods with constant current densities ranging from 100 to 600 mA cm^{-2} and cell temperatures between 60 and 95 °C under H$_2$/O$_2$ or H$_2$/air (CO$_2$-free).

Aryl-ether-containing AEPs tend to be unstable in AEMFCs due to aryl-ether cleavage reactions. The SQDEO membrane with aryl-ether bones in the backbones showed a voltage drop from 0.72 to 0.48 V at a current density of 200 mA cm^{-2} at 60 °C for 12 h.[118a] Similarly, the OBImPPO26-PEG05 membrane with aryl-ether backbones experienced a notable voltage drop after approximately 4 hours at a current density of 400 mA cm^{-2} at 60 °C.[121] Those results underscore the importance of backbone structures in determining the stability of AEMs.

In contrast, PA-based AEMs with aryl-ether-free backbones and piperidiniums demonstrated enhanced stability in AEMFCs. For instance, the QAPPT membrane maintained 0.62 V at a constant current density of 200 mA cm^{-2} at 80 °C under H$_2$/air (CO$_2$-free) for 125 h.[68b] The high-molecular-weight PAP-TP-85 copolymer, with PA-based backbones and piperidiniums, operated at a constant current density of 500 mA cm^{-2} at 95 °C under H$_2$/air (CO$_2$-free) for 300 h with an 11.5% voltage loss.[22]

Several PA-based IM-containing AEMs have been evaluated for their stability under H$_2$/O$_2$ conditions in AEMFCs. Aemion+, a commercial IM-based AEM, showed a voltage drop rate of 7.1 mV h^{-1} at a constant current density of 600 mA cm^{-2} for 20 h at 70 °C under H$_2$/O$_2$.[120] In a long-term stability study, a StIM-based AEM demonstrated a 31% voltage drop after 230 h of operation at a constant current density of 50 mA cm^{-2} under H$_2$/O$_2$ at 60 °C after 230 h.[124]

The PFBA-QA-0.4 copolymer, with mid-long aryl side trains, maintained over 0.7 V in an H$_2$/O$_2$ AEMFC at 200 mA cm^{-2} at 60 °C for 74 h.[130a] The QPAF-C3-Pip polymer, synthesized via a nickel-catalyzed coupling reaction, exhibited a decay rate of 1.29 mV h^{-1} at a constant current density of 100 mA cm^{-2} at 60 °C under H$_2$/O$_2$ for 240 h.[134h] The PA-based, piperidinium containing PFTP-13 copolymer, with rigid FLN groups, showed a 3.68% voltage drop at a constant current density of 200 mA cm^{-2} at 70 °C under H$_2$/O$_2$ for 200 h.[25] The block polymer PBPA-b-BPP-0.10 achieved stable AEMFC voltage output at a current density of 600 mA cm^{-2} at 70 °C under H$_2$/O$_2$ for 170 h, with a voltage decay rate of 0.53 mV h^{-1}.[30] Similarly, the branched PA-based b-PTP-2.5 maintained voltage between 0.68 and 0.51 V at a constant current density of 200 mA cm^{-2} at 60 °C under H$_2$/O$_2$ for the first 160 h, holding above 0.51 V for entire 500 h stability test with two catalyst layer refreshment processes.[151b] Another branched PA-based AEM, B-PDTP-TRIP-5, exhibited a voltage drop of 0.46 mV h^{-1} for 500 h operated at 600 mA cm^{-2} at 70 °C under H$_2$/O$_2$ with two immersions of the MEA into 1 mol L^{-1} NaOH solution for 12 h (Figure 13f).[34] With the in-situ crosslinking strategy, a MEA comprising x-PDTP-Pr-10 AEM, x-Trip-PFBP-Pr-10 anode ionomer, and x-Trip-PFBP-Pr-30 cathode ionomer demonstrated a 1000 h longevity with a voltage drop rate of 0.02 mV h^{-1} when tested at 600 mA cm^{-1}, 80 °C under H$_2$/O$_2$. The MEA was refreshed by immersing it in an alkaline solution overnight.[160b]

A PE-based HDPE-AEM was tested in an H$_2$/air (CO$_2$-free) AEMFC at a current density of 600 mA cm^{-2} at 70 °C for 440 h, exhibiting only 7% voltage degradation at a rate of 0.68 mV h^{-1}.[68a] GT64-15, a PNB-based AEM, operated in an H$_2$/air (CO$_2$-free) AEMFC at a current density of 600 mA cm^{-2} for 545 h without detectable chemical degradation but a 17% drop during the first 300 h.[147] Another PNB-based AEM, GT82-15, was tested in H$_2$/air (CO$_2$-free) AEMFC at a current density of 600 mA cm^{-2} at 70 °C for 100 h with negligible voltage loss.[23] These two PNB-based AEMs demonstrated stable voltage in the AEMFCs operated at 600 mA cm^{-2}, showing the potential of PNB-based AEMs for AEMFC applications.

A PE-based AEM, F20C9N, was tested in an H$_2$/O$_2$ AEMFC at a current density of 600 mA cm^{-2} at 60 °C for 120 h. It showed rapid voltage decay at the first 20 h from 0.75 to 0.67 V, followed by a steady degradation rate of 0.2 mV h^{-1} for the subsequent 100 h.[103c] Lastly, the PS-based UHWMPE4-s-AEM, tested in an AEMFC at a constant current density of 300 mA cm^{-2} at 65 °C for 12 h, showed voltage drops of 2.8% and 5.4% under H$_2$/O$_2$ and H$_2$/air (CO$_2$-free), respectively.[142]

4.5. Summary and Outlook of Anion Exchange Polymers in AEMFCs

Anion exchange polymers are essential in advancing AEMFC technology. The ideal AEP should exhibit high alkaline stability, excellent conductivity, robust mechanical properties, and strong performances in AEMFCs, including both activity and stability.

Among cationic groups, aliphatic heterocyclic quaternary ammoniums, particularly piperidinium-based AEMs, have been extensively studied for their stable alkaline properties and high activity in AEMFCs. Recently, quinuclidinium groups have shown

**ADVANCED
SCIENCE NEWS**

www.advancedsciencenews.com

**ADVANCED
MATERIALS**

www.advmat.de

exceptional alkaline stability, though their use in AEMFCs remains limited. Increased research on quinuclidinium-based AEMs may further improve AEMFC performance.

Poly(arylene) (PA)-based AEPs are commonly used as AEM backbones due to their relatively simple synthesis processes. Synthesis methods of PA-based AEPs include acylation reaction,[118a] demethylation,[146c] acid-catalyzed condensation reaction,[25,26,30,34,68b,130a,133,151a,b,158d] Menshutkin reaction,[22,121] Cu-catalyzed click chemistry,[121] Suzuki coupling reaction,[132,133] nickel-catalyzed coupling reaction,[134f,h] Diels-Alder reaction,[102a] microwave polycondensation method.[122] Copolymer and branched strategies have led to high-molecular-weight PA-based AEPs with enhanced mechanical properties and improved stability in alkaline environments and AEMFCs. However, the phenyl-group adsorption effect can poison electrocatalysts, which requires caution when developing PA-based AEPs.

Polyethylene (PE)-based AEPs show stable AEMFC performance, although one common synthesis method, radiation-grafting polymerization, requires specialized equipment, limiting their scalability.[14a,16,68a,135d] Other synthesized methods, such as Ziegler-Natta polymerization and ring-opening metathesis copolymerization, have also been used to create PE-based AEPs.[103c,136a,137d] ETFE-AEI is solid, which could lead to inconsistent dispersion with electrocatalysts and form a less efficient three-phase boundary in AEMFCs.[16] PE-based AEPs with improved dispersion and accessible synthesis methods would be ideal for AEMFC applications.

Poly(norbornene) (PNB)-based AEPs exhibit high OH⁻ conductivity in AEPs due to their high ICEs. In AEMFC testing, PNB-based MEAs have demonstrated high peak power densities and extended operation times. PNB-based AEPs are mainly synthesized using ring-opening metathesis polymerization, vinyl addition polymerization method, and Diels-Alder reaction.[23,138a,139a,147,158f] However, the AEMFC stability of PNB-based MEAs often fluctuates due to water management issues, suggesting that further research into their water uptake and water content properties is needed.

Polystyrene (PS)-based AEPs can be derived from commercial SEBS, simplifying synthesis. The synthesis methods of PS-based AEPs include radical polymerization,[140,141] in-situ polymerization,[142] Friedel-Crafts reaction,[143a] Suzuki coupling reaction,[143b] and chloromethylating method.[145] However, PS-based AEPs typically exhibit lower AEMFC performance than other AEP types due to the limited PS contents in SEBS. Enhancements could focus on increasing PS content in SEBS or functionalizing the rubbery domains of SEBS.[144b,161]

Several strategies have been developed to enhance AEP properties. Microphase separation through long-side chains, copolymerization, block polymers, and branched polymers is the most widely used approach. Further studies on microphase separation could improve the design of ion-conductive channels and free volume. The cross-linking method effectively controls the water uptake, while balancing mechanical properties. The in-situ crosslinking strategy is an effective approach to construct stable catalyst layers and significantly enhances the adhesion strength between the catalyst layer and the membrane. Additionally, hy-

brid AEM structures, such as porous-sandwich structure composite membranes,[162] aligned composite membranes,[163] and magnetic field-oriented membranes,[164] have been developed to improve the conductivity and mechanical properties of AEMs. However, further investigation is needed to fully integrate these hybrid AEMs in AEMFCs.

5. Cell Operating Management

In addition to developing novel materials, cell operation management is vital to obtaining a high-performance AEMFC. After proper optimization of the fuel cell operating conditions, like the dew points of the anode and the cathode,[19,165] the feed gas backpressure,[165] and the electrode structure,[166] the peak power density of the optimized AEMFCs can be two-fold or higher than the counterparts with the same catalysts and membranes. The cell operation management for optimizing AEMFC performance was also recently reviewed by Li et al.[167]

In cell operation management, the main challenge is mass transport. Compared with the tests in RRDE, the catalyst loading in MEA is higher, and the testing conditions are harsher, including higher operation temperature, higher current density, and sometimes higher pressure. Similar issues are also affecting the development of PEMFC, as reviewed by Fan et al.[168] Those strategies and experiences can be transferred to the cell operation management of AEMFC.

The two main hurdles in AEMFC cell operation are water management,[1a,15a,19,23,165] and CO_2 limitation.[10,15b,169] In AEMFC, water is generated at the anode by HOR (Equation 1) but also consumed at the cathode by ORR (Equation 2), which tends to flood the anode while the cathode is potentially drying out. The water molecules are transported from the cathode to the anode by the electro-osmotic drag effect and can be back-diffused from the anode to the cathode due to the concentration gradient of water. This water transportation of AEMFC causes more water-management-related issues than in PEMFC. When AEMFCs are under a low hydrated condition, the nucleophilic OH⁻ ions also drive severe AEM degradation which directly affects the performance and durability of AEMFCs.[170] The alkaline environment of AEMFCs can also become an issue when the cathode feed gas is switched to air because of the generation of carbonate and bicarbonate from CO_2 in the air. The carbonate and bicarbonate ions can lower the transfer rate of hydroxide ions, which also affects the performances of AEMFCs. Due to these significant effects on the performance and life span of AEMFCs, the details of water management and CO_2 limitation AEMFCs will be discussed in Section 5.2 and 5.3.

5.1. MEA Preparation and AEMFC Operating Conditions

MEA is the heart of an AEMFC, significantly affecting its performance. The preparation of MEAs briefly assembles the gas diffusion layer (GDL), the catalyst layer (CL), and the membrane (**Figure 15a**). Choosing different MEA components impacts the mass transport in AEMFCs, including the accessibility of active sites, anion transport, and, most importantly, water transport, which will be discussed in Section 5.2.[171]
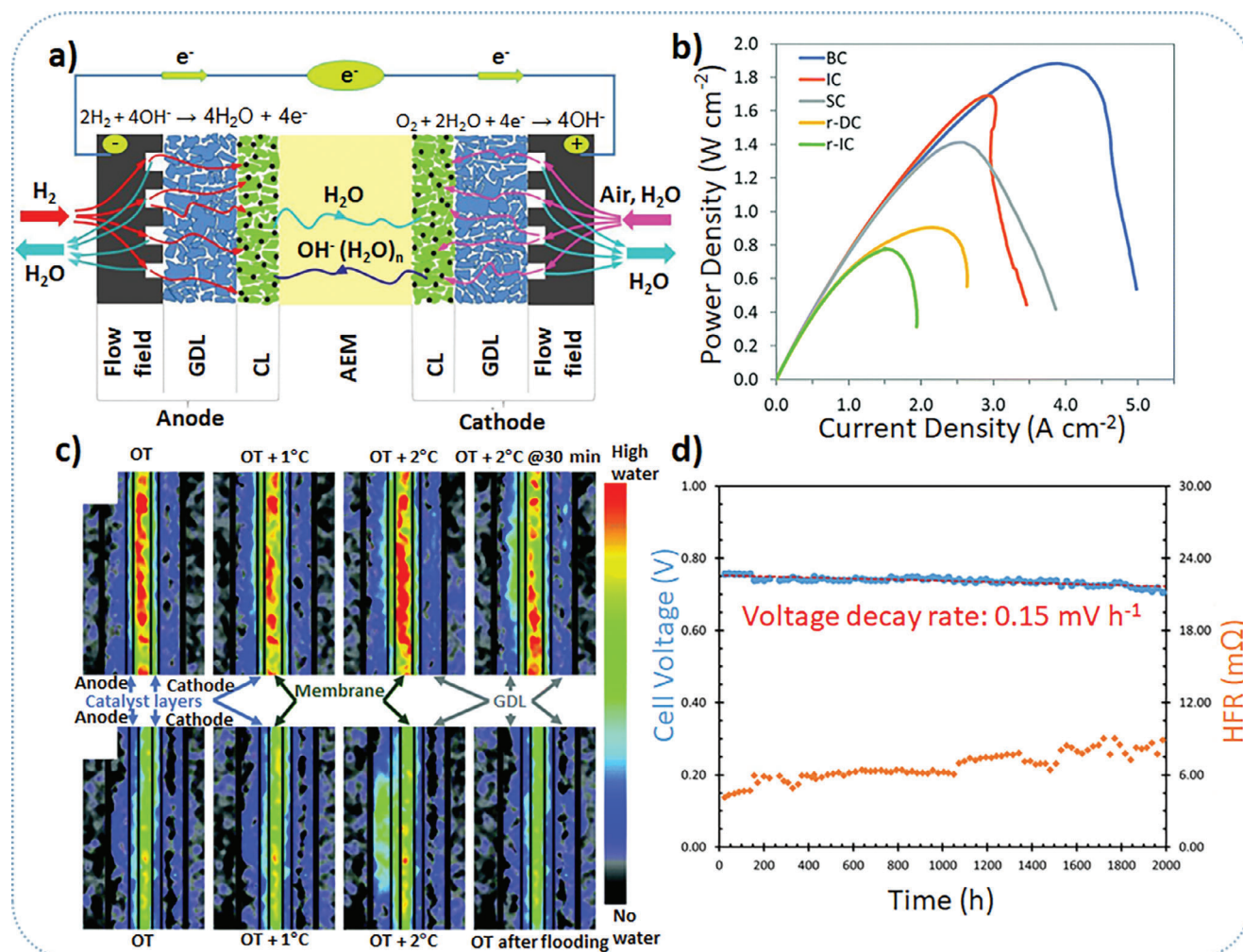
**ADVANCED
SCIENCE NEWS**

www.advancedsciencenews.com

**ADVANCED
MATERIALS**

www.advmat.de

Figure 15. a) Schematic presentation of an H_2/air AEMFC and the components inside the cell; Reproduced with permission.[7f] Copyright 2018, Elsevier. b) Polarization curves of H_2/O_2 AEMFCs equipped with the same cathode while different anode structures, i.e., the electrode of the standard amount of carbon (SC), the electrode of increased carbon ratio (IC), the electrode of 60% loading with the same ratio of carbon, ionomer, and catalyst as IC (r-IC), the electrode of the same loading of r-IC but twice the ratio of carbon to ionomer (r-DC), and the electrode of balanced ratio of carbon, ionomer, and catalyst (BC); Test conditions: The cell temperature at 60 °C with optimized dew points (anode/cathode) to different anode structures: BC (45/46), IC (47/49), SC (54/57), r-IC (53/53), r-DC (51/52), (unit: °C); Reproduced under terms of the CC-BY license.[19] Copyright 2018, The Authors, published by the Royal Society of Chemistry. c) Operando in-plane neutron radiographic images of water in two H_2/O_2 AEMFCs, i.e., ETFE-MEA-based AEMFC (above) and PFAEM-based AEMFC (below), after equilibration at the following symmetric dew points: optimum temperature (OT), OT+1 °C, OT+2 °C, and OT+2 °C @ 30 min for ETFE-MEA-based AEMFC (above) or recovered cell at OT for PFAEM-based AEMFC (below); Reproduced under terms of the CC-BY license.[19] Copyright 2018, The Authors, published by the Royal Society of Chemistry. d) Cell voltage and high-frequency resistance during a 2000 h stability test at constant current density of 600 mA cm^{-2} in an H_2/O_2 AEMFC; Test conditions: PtRu/C anode (0.7 mg$_{PtRu}$ cm^{-2}, GT78 ionomer) and Pt/C cathode (0.6 mg$_{Pt}$ cm^{-2}, GT32 ionomer); cell temperature at 75 °C; dew points of anode and cathode at 72/74 °C with no backpressure; Reproduced with permission.[14b] Copyright 2020, John Wiley and Sons.

Common catalyst deposition techniques include drop coating, blade coating, air-blush spray, and ultrasonic spray.[172] The catalyst layer in MEA can be applied to gas diffusion electrodes or membranes, using the catalyst-coated substrate (CCS) method and the catalyst-coated membrane (CCM) method, respectively. The CCS method is widely used because of its straightforward preparation process, but challenges with ink uniformity and catalyst layer consistency can arise. In contrast, the CCM method, which applies the catalyst layer on both sides of the membrane, requires specialized coating equipment. However, it offers enhanced interface stability between the CL and membrane, eliminating the need for a hot-press process—making it particularly suited for more brittle membranes.

In a study comparing the CCS and CCM methods using commercial AEMs, Chae et al. found that the ohmic resistance at 0.6 V was consistently lower with the CCM method across all tested AEMs.[173] For instance, using the CCM method with PiperION membranes reduced ohmic resistance by 69% compared to the CCS approach. Similarly, Li et al. compared the CCS and CCM methods for fabricating MEAs with branched AEMs (B-PAPA).[151c] The MEA prepared by the CCM method achieved a peak power density of 0.69 W cm^{-2}, outperforming the MEA

**ADVANCED
SCIENCE NEWS**

www.advancedsciencenews.com

**ADVANCED
MATERIALS**

www.advmat.de

prepared with the CCS method (0.43 W cm^{-2}) due to the reduced contact resistance between the membrane and catalyst layer.

By tuning the accessibility of active sites and ion transport, the AEI weight percentage in the CL is an important parameter.[16,174] AEIs in AEMFC act as the binder and as the anion conductor to conduct OH$^-$ to the active sites and let the reactions happen at the three-phase boundary. Insufficient AEI lowers the utilization of the catalyst. However, too much AEI reduces the mass transport by clogging the channels and the pores in the catalysts, thus increasing the resistance in the catalyst layer. Accordingly, Kaspar et al. found that the 20 wt.% of AEI delivered the highest peak power density.[175] The AEI weight percentage in the ink could also affect the electrode surface condition—two inks with 15 wt.% and 20 wt.% AEI were prepared and used to fabricate the MEA with symmetrical ionomer weight percentage in the anode and the cathode. The 15 wt.% ink induced cracks on the surface of the catalyst layer, where isolated AEI particles were found.[16] The fuel cell tests showed that the use of 15 wt.% ink resulted in an AEMFC exhibiting a larger overpotential at low current density and low power density (0.18 W cm^{-2} at 50 °C under fully hydrated conditions) than the one derived from the use of 20 wt.% AEI (0.24 W cm^{-2} under the same conditions).

Instead of the weight percentage of AEI, the interaction between dispersions and ionomers can also affect the ionomers aggregation in CL.[176] Hyun et al. controlled the aggregation of ionomer, m-TPN (meta-poly(terphenylene)), in CL with three different dispersions, i.e., isopropanol, methanol, and dimethyl sulfoxide.[176a] The ionomer dispersion was most homogeneous with dimethylsulfoxide and most aggregated with isopropanol. They found that if the ionomer-solvent interaction was weaker than the ionomer self-interaction, the ionomer trended to aggregate. The aggregated ionomer clogged the porous structures of catalysts and decreased the peak power densities of fuel cells.

Anion exchange membranes act as a gas separator and a solid electrolyte transporting anions in AEMFCs. The chemistry of AEMFC was discussed in Section 4. In addition to the pristine properties of AEM, membrane pre-treatment is also an essential step in AEMFC tests. An alkaline solution, like NaOH solution, is widely adopted in membrane pre-treatment steps; however, its function is unclear. Shi et al. studied the functions of this step by pre-treating the AEMs with NaHCO$_3$ and NaOH, compared to the AEM without pre-treatment.[177] Before studying the functions of the pre-treatment step, the authors found acetate from the ion chromatography analysis of different MEAs when the ethanol and Pt-based catalysts were used simultaneously in the ink preparation. In contrast, acetate was absent in the Pt/Pd-free-catalyst-based MEA or without using ethanol. Acetate was considered an oxidation product from the oxidation reaction catalyzed by Pt or Pd. Following this analysis, all the MEAs with Pt-based and Pt/Pd-free catalysts were pre-treated by NaOH and NaHCO$_3$ and then tested in H$_2$/O$_2$ AEMFCs. The results showed that: (i) the alkaline pre-treatment helped eliminate carboxylates, like acetate, generated from primary alcohols, e.g., ethanol, oxidation over Pt or Pd during the MEA preparation; (ii) bicarbonate pre-treatment, such as NaHCO$_3$, is a better choice because it acts as an ion exchange agent without the use of strong bases, which influenced the cell performance as shown in the AEMFC test; (iii) the MEAs with Pt/Pd-free catalyst exhibited better performance without alkaline pre-treatment of the membrane.

The operation temperatures of AEMFCs range typically between 60 to 95 °C and mainly depend on the properties of the membranes. At the beginning of AEMFC's development, because of the usage of aryl-ether polymers, the cell temperature was limited to ca. 60 °C to increase the AEMFCs' lifespan. Recently, the cell temperatures have been elevated to 80 °C or even to 95 °C.[22,25,98a] The elevated temperature can accelerate the reaction rates and decrease the HBE, increasing the cell power outputs.[70,165]

The backpressure also has an important effect on the AEMFC performance. A higher backpressure is considered to increase cell performance by elevating the fuel's partial pressure. The backpressure can also have other effects on the AEMFCs' performance. Li et al. showed that increased backpressure narrowed the performance gap between the PtRu/C anode and the Pt/C anode even though Ru can lower the H absorption energy on Pt and provide OH$^-$ absorption sites, which were considered to facilitate the HOR rate.[70] When the backpressure of the AEMFC was increased to 0.20 MPa at 80 °C, the peak power density was 2.08 W cm^{-2} with the PtRu/C as the anode and Pt/C as the cathode. Even if the anode catalyst was changed to the Pt/C catalyst, the peak power density still reached 1.92 W cm^{-2} at 80 °C. The narrowed performance gap between the PtRu/C and the Pt/C anode was ascribed to the decreased HBE, which could also be achieved by higher cell temperature. The backpressure in AEMFCs is usually applied equally to anodes and cathodes to avoid membrane breakage and fuel crossover. However, by using unequal backpressure to AEMFC, Wang et al. discovered that the backpressure at the anode needed to be lower than that at the cathode (0.13 and 0.25 MPa, respectively) to enhance both the water removal at the anode and the water retention at the cathode.[165]

5.2. Water Management

As discussed in the introduction, during the operating cell, HOR generates water at the anode, while ORR consumes water at the cathode. Water is also transported from the cathode to the anode by electro-osmotic drag and diffuses back in the opposite direction, driven by the concentration gradient of water. On account of these issues, water management in AEMFCs is crucial to avoid flooding or drying out of the electrodes and to keep the MEAs hydrated for long and smooth outputs.

When the cell is flooded, the performance of AEMFCs significantly decreases due to mass transfer losses triggered by the accumulation of excess water on the anode surface, blocking proper gas diffusion to the active sites.[1a] On the other hand, under insufficient hydration, i.e., the cathode electrode drying out, the cell performance at the mass transfer region of the polarization curves is reduced by the insufficient H$_2$O as a reactant at the cathode. The dynamic equilibrium of water content can be achieved by adjusting the feed gas's dew point and flow rate, tuning the electrode structure, and using a suitable membrane to enhance the water back diffusion.[19,135g]

Omasta et al. demonstrated that optimizing the water management by lowering the anode dew point from 60 °C to 58 °C while keeping the cathode dew point at a fixed cell temperature of 60 °C could increase the power densities by at least 2.5 times.[1a] Moreover, increasing the fuel cell temperature enabled its operation

**ADVANCED
SCIENCE NEWS**

www.advancedsciencenews.com

**ADVANCED
MATERIALS**

www.advmat.de

under higher relative humidity and mitigated water flooding by increasing absolute water content in the gas phase, thus improving the capacity of the gas flow to carry more water. The flow rate of the gas inlets also has a substantial impact on cell water management and cell performance. The cell performance decreased when the flow rate was low since the water removal was less efficient. Besides, the authors indicated that the fuel cell performance was more sensitive to the flow rate at the cathode rather than that at the anode.

To address the challenges associated with the accumulation of water and flooding problems in AEMFCs, the composition of the electrodes, including catalyst loading and the amount and ratio between carbon, ionomer, and catalyst, was also studied by Omasta et al.[19] The authors developed five anode electrodes denoted as follows: the electrode of the standard amount of carbon (SC), the electrode of increased carbon ratio (IC), the electrode of 60% loading with the same ratio of carbon, ionomer, and catalyst as IC (r-IC), the electrode of the same loading of r-IC but twice the ratio of carbon to ionomer (r-DC), and the electrode of balanced ratio of carbon, ionomer, and catalyst (BC) to study the mitigation methods for water management. Apart from the different types of anodes, the MEAs were constructed with a Pt/C cathode (loading: 0.53-0.54 mg_{Pt} cm^{-2}), an ETFE-AEM, and an ETFE-AEI.

Compared to SC, with a carbon loading of 0.45 mg cm^{-2}, the carbon content in IC was increased to 0.71 mg cm^{-2} to obtain a higher pore volume and water capacity at the anode electrode.[19] The cell power density curves are shown in Figure 15b. The IC-based fuel cell showed a higher power density (1.70 W cm^{-2}) than that of the SC-based fuel cell (1.40 W cm^{-2}). However, water management in the IC-based fuel cell is still a concern in the mass transfer region. To investigate this, the r-IC electrode was fabricated. The IC and r-IC curves showed that lower water capacity in the electrodes lowered the limiting current. To increase the water capacity of the electrode, r-DC was developed with a doubled ratio of carbon to ionomer but the same catalyst loading as in r-IC. As the carbon-to-ionomer ratio was increased, the mass transport limiting current density and the peak power density increased by 35% and 15%, respectively, thanks to the higher water buffering capacity, ionic conductivity, and water mobility in the catalyst layer. Finally, the optimal ratio among AEI, carbon, and Pt was set as 0.94: 2.5: 1.0, with the same PtRu loading of IC, i.e., 0.71 mg_{PtRu} cm^{-2}, denoted as BC. The AEMFC test with the BC electrode showed a mass transport limiting current density of 5 A cm^{-2} and a peak power density of 1.90 W cm^{-2}. The AEMFC maintained an acceptable performance in a wide cell humidity range, namely, from optimum dew points (anode/cathode: 54/51 °C) to optimum dew points +5 °C, applied to both the anode and the cathode, which suggested that the mass transfer loss induced by water management was not an issue by using BC electrode.

Furthermore, the water distribution in the cell components was studied and visualized in an operando neutron experiment (Figure 15c). The quantitative through-plane water distribution was varied by controlling the dew points of the anode and cathode at three temperatures, i.e., optimum temperature (OT), OT+1 °C, and OT+2 °C.[19] As seen in Figure 15c, an increase in the dew point of the feed gas causes a large amount of water to accumulate at the anode, whereas the water accumulation at the cathode

is rarely affected by the changing dew points. Regarding cell performance, the accumulated water induced a significant drop in the cell voltage observed in the high current density region. The results also suggested that the water back diffusion from the anode to the cathode was the primary way to keep the AEM hydrated and of the water source to the cathode to maintain fuel cell operation.

Similarly, operando neutron imaging technology coupled with micro X-ray computed tomography (X-ray CT) was used to examine the water distribution in AEMFCs under different cell operating conditions, such as varying current density and backpressure during the cell operation.[178] The author found that under the same dew point, the amount of liquid water in the cell was proportional to the current density. Low current density generates less water at the anode, leading to water scarcity at the cathode and reducing water transfer through the membrane. The relationship between water and current density helped optimize the dew point for the anode and the cathode at each operating current density to optimize the cell performance. The backpressure also impacts the water distribution in the fuel cell. They also found that when the backpressure increased, the rate of convective evaporation from the anode reduced, which made the cell operate under relatively low electrode dew points and relatively low current density but suffered less drying out issues.

Water management also influences the long-term AEMFC operation. If flooding events frequently happen, the cell voltage is unstable in AEMFCs. On the other hand, flooding is avoided when the water content is low, but the performance is reduced since the ionomer and polymer degrade rapidly under low RH.[170,179] To gain the steady and optimized water content in AEMFC, two contents of PTFE, i.e., 8 wt.% and 20 wt.% were added to the CL and GDL, respectively. After employing the new MEA, the cell could achieve a peak power density of 2.35 W cm^{-2} under H_2/O_2 and 1.60 W cm^{-2} under H_2/air (CO_2-free).[178] The stability of PTFE-containing AEMFC was significantly improved as the cell continuously operated at 600 mA cm^{-2} and 65 °C for over 1000 h under fully humidified H_2/ air (CO_2-free) with only a 4.6% voltage loss. This improved performance was explained by the following hypothesis: the high water content extends the lifespans of ionomers and polymer membranes, while the PTFE-added MEAs have superior dynamic water management and provide stability. X-ray CT verified the water content optimization, where no visual flooding or ionomer swelling was observed.

From the experiments above, we know that adding the PTFE to the CL and the GDL can change the performance of AEMFCs due to their different wetproofing properties. Kaspar et al. systematically studied the weight percentage of PTFE in GDL.[175] Five GDLs were chosen with different PTFE weight percentages of 0, 5, 10, 20, and 50. The results showed that even a low level of wetproofing (5 wt.%) had a noticeable negative effect on the cell polarization curves, and this effect was more evident if the PTFE increased to 50 wt.% by trapping water in the electrode. However, this negative effect of PTFE was solely observed when added to the anode electrode, as opposed to being exclusively added to the cathode. The reason was that the PTFE at the anode acted as a water-retaining barrier, causing anode flooding, even at moderate current density (170 mA cm^{-2}). While at the cathode, water

**ADVANCED
SCIENCE NEWS**

www.advancedsciencenews.com

**ADVANCED
MATERIALS**

www.advmat.de

was consumed, so this water-trapping effect had minimal impact on the cell polarization curve. The authors concluded that little or no waterproofing (0-5 wt.%) was optimal as the trapped water decreased the internal resistance. However, if the hydration level was too high, in this case, caused by the high amount of wetproofing agent ETFE, mass transport loss happened because of the flooding of the anode.

Changing the hydrophilic properties of AEIs is another way to manage the water content in AEMFCs. Hu et al. compared two anode ionomers that have similar ionic conductivity and IEC but different hydrophilic properties, i.e., the hydrophilic quaternary ammonia poly(*N*-methyl-piperidine-co-p-terphenyl) (QAPPT) and the hydrophobic quaternary ammonia poly(arylene perfluoroalkylene) (QAPAF).[130b,180] The fuel cell based on QA-PAF outputted a stable performance over the entire tested current density interval (from 4 to 0.6 A cm^{-2}), while the fuel cell using the QAPPT ionomer showed inferior stability and lower operation voltage at identical current densities.[180] The significant difference between the two anodes, analyzed by the distribution of relaxation times deconvolution method to the electrochemical impedance spectroscopy semi-circle, was found to be the mass transport resistance caused by the different hydrophilic properties between the QAPPT and the QAPAF-derived electrodes.[180,181]

Hassan et al. also studied the hydrophilic properties of AEIs.[14b] The authors used different poly(norbornene) tetrablock copolymer ionomers which were denoted as GT32, GT64, and GT78. The number following the GT represents the mole fraction of the quaternary ammonium group. The IEC values of GT32, GT64, and GT78 obtained were 1.88, 3.37, and 3.74 meq. g^{-1}, and the water uptake values were 63%, 90%, and 163%, respectively. Since water is the product at the anode and the reactant at the cathode, the required hydrophilic properties of AEIs are different at the anode and cathode. The authors constructed asymmetric electrodes with different ionomers on each side: the hydrophilic ionomer (GT78) at the anode and the less hydrophilic analog (GT32) at the cathode. The higher water uptake of GT78 helped the anode surface to discharge water more quickly to the membrane and the anode feed gas. Besides, backpressure was added to the cathode side to suppress the convective evaporation of water and to keep the cathode hydrated. Lastly, PTFE was incorporated into both catalyst layers to reject excessive liquid water. Eventually, the cell reached a peak power density of 3.20 W cm^{-2} under H$_2$/O$_2$, which is twice the value of the fuel cell using symmetric GT64 ionomer on both sides and 1.75 W cm^{-2} under H$_2$/air (CO$_2$-free) at 80 °C with optimized dew points of feed gases. The fuel cell operated at a current density of 600 mA cm^{-2} at 75 °C for 2000 h with a voltage decay rate of 0.15 mV h^{-1} and a voltage loss of only 3.65%, demonstrating excellent stability (Figure 15d).

The water distribution inside AEMFCs is also affected by the introduction of CO$_2$ into the cathode feed gas. It was shown that after carbonation, the backbone crystallinity of AEMs decreased, which decreased the water uptake in AEMs.[15c] Water distribution inside the carbonated AEMFC was visualized by operando neutron imaging. The results showed a decreased water uptake in the entire AEMFC caused by the introduction of CO$_2$ at the cathode. The following section will discuss the detailed effects of CO$_2$ on AEMFCs.

5.3. Impact of CO$_2$

When the cathode feed gas is switched from oxygen to ambient air containing ca. 400 ppm of CO$_2$, the OH$^-$ anions from ORR react with CO$_2$ to generate carbonate and bicarbonate anions, as shown in Equations (11) and (12). These carbonate and bicarbonate anions have lower mobility than hydroxide ions, which lowers the ionic conductivity of AEM and, consequently, reduces the fuel cell performance.[10,15a]

$$OH^- + CO_2 = HCO_3^- \tag{11}$$

$$HCO_3^- + OH^- = CO_3^{2-} + H_2O \tag{12}$$

A study showed that when the OH$^-$ was partially replaced by CO$_3^{2-}$ by immersing the membrane in KHCO$_3$, the peak power density decreased from 0.61 W cm^{-2} to 0.43 W cm^{-2} in H$_2$/O$_2$ AEMFCs at 60 °C.[169a] The cell voltage (V_{cell}) can be divided into seven parts and written as the equation below:

$$V_{cell} = V_{OCV} - i\left(R_{\Omega,\,OH} + R_{ctORR} + R_{mtORR} + R_{ctHOR}\right)$$
$$-\Delta V_{Nernst} - i\left(\Delta ASR + \Delta R_{ctHOR}\right) \tag{13}$$

where V_{OCV} is the open-circuit voltage; i is the cell current; $R_{\Omega,OH}$ is the ohmic resistance for OH$^-$ anion transport; R_{ctORR} is the charge transfer resistance for ORR; R_{mtORR} is the mass transport resistance for ORR; R_{ctHOH} is the charge transfer resistance for HOR; ΔV_{Nernst} is the Nernstian voltage loss; ΔASR is the change of area-specific resistance; and ΔR_{ctHOR} is the change of charge transfer resistance for HOR.

The main reasons for CO$_2$-related voltage drop (ΔV_{CO_2}) are ΔASR, ΔV_{Nernst}, and ΔR_{ctHOR}. When CO$_2$ is introduced into an AEMFC, the ΔASR increases. The HCO$_3^-$ and CO$_3^{2-}$ anions partly replace the OH$^-$ anion, and the ionic conductivity of HCO$_3^-$ and CO$_3^{2-}$ anions is lower than that of OH$^-$ anions. The ionic radius of HCO$_3^-$ and CO$_3^{2-}$ is more significant than that of OH$^-$, which leads to a lower diffusion coefficient and lower ionic mobility of HCO$_3^-$ and CO$_3^{2-}$ in solutions and AEMs.[169c,182] Moreover, OH$^-$ anions are transported through the membrane via several mechanisms, such as diffusion, convection, and proton hopping. The hopping mechanism is exclusive to OH$^-$ and not observed for HCO$_3^-$ and CO$_3^{2-}$ anions.[10,183]

As the OH$^-$ anions are continuously produced at the cathode, HCO$_3^-$ and CO$_3^{2-}$ are generated constantly with CO$_2$ in the feed gas and then diffuse from the cathode to the anode. ΔV_{Nernst} is caused by a decrease in the local pH as HCO$_3^-$ and CO$_3^{2-}$ anions are accumulated at the electrode. According to the Nernst equation, the overpotential increases theoretically by 180–350 mV.[184]

The accumulated HCO$_3^-$ and CO$_3^{2-}$ anions occupy the active sites at the anode catalyst. As a result, the value of ΔR_{ctHOR} increases, even though the intrinsic HOR activity is not affected by the HCO$_3^-$ and CO$_3^{2-}$ anions. By analyzing the impact of CO$_2$, the authors indicated that ΔV_{Nernst} and ΔR_{ctHOR} dominated the ΔV_{CO_2}, whereas the contribution of ΔASR was minor.[15a]

In studying the impact of CO$_2$ on the voltage loss in H$_2$/air (ambient) AEMFCs, Mustian and co-workers found that the ΔV_{CO_2} was increased when the current density decreased, and the CO$_2$ concentration in the cathode feed gas increased.[15a,b] For

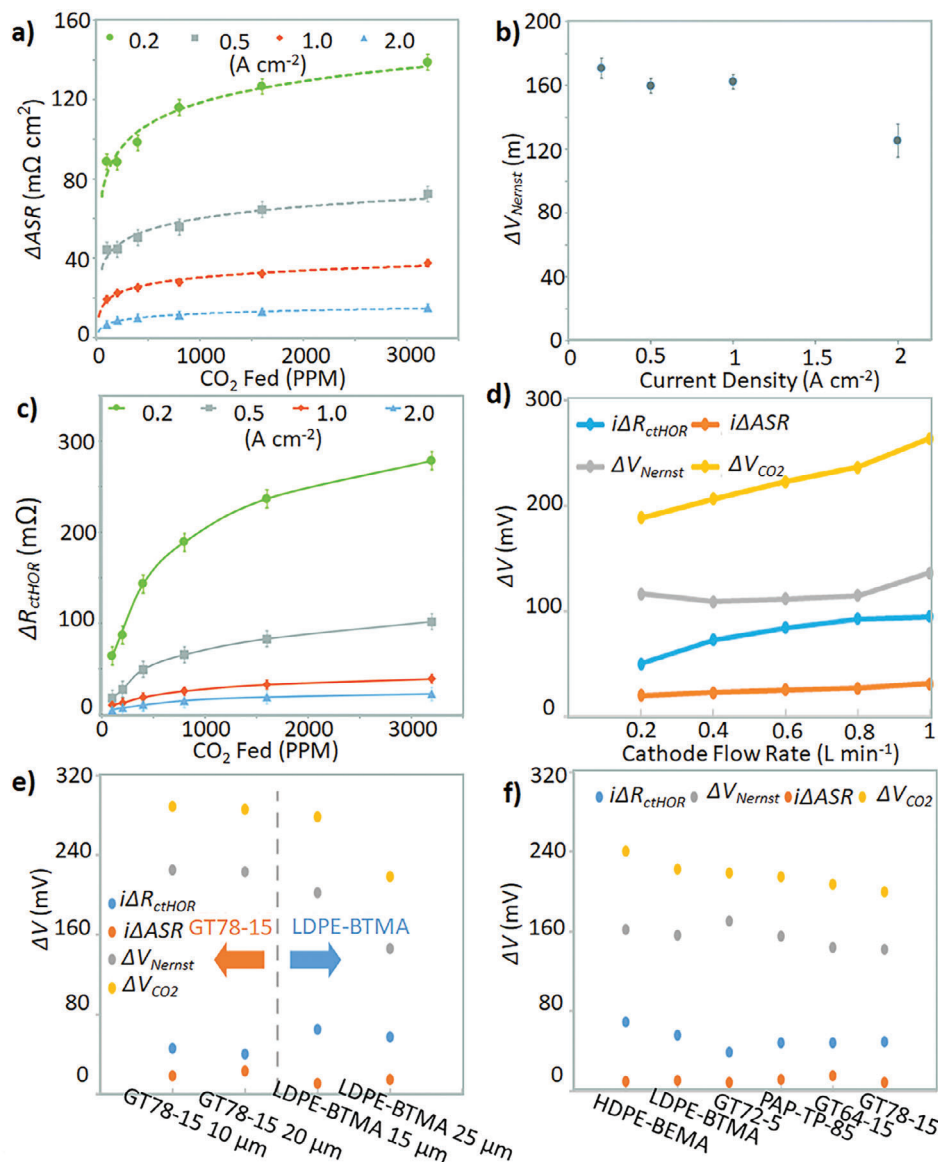**Figure 16.** a) The change in the ΔASR at various current densities and CO_2 concentration from the deconvoluted ΔV_{CO_2}; Reproduced under terms of CC-BY license.[15a] Copyright 2019, The Authors, published by the Royal Society of Chemistry. b) The change of ΔV_{Nernst} as the function of current density; Reproduced under terms of CC-BY license.[15a] Copyright 2019, The Authors, published by the Royal Society of Chemistry. c) The change of ΔR_{ctHOR} at various current densities and CO_2 concentrations from deconvoluted ΔV_{CO_2}; Reproduced under terms of CC-BY license.[15a] Copyright 2019, The Authors, published by the Royal Society of Chemistry. d) Deconvoluted ΔV_{CO_2} from the effect of cathode flow rate; Reproduced with permission.[15b] Copyright 2020, Elsevier. e) Deconvoluted ΔV_{CO_2} with different membrane thicknesses; Reproduced under terms of CC-BY license.[15c] Copyright 2021, The Authors, published by MDPI. f) Deconvoluted ΔV_{CO_2} with different types of AEM; Reproduced under terms of CC-BY license.[15c] Copyright 2021, The Authors, published by MDPI.

ΔASR, it was small if the CO_2 concentration at the cathode was low and the current density was high. When the high current density was applied to AEMFCs, the concentration gradient of carbonated species in the AEM shifted towards the anode electrode, which triggered the self-purging mechanism at the anode. Hence, the CO_2 content was reduced in the fuel cell (**Figure 16a**). For ΔV_{Nernst}, when the current density increased, it decreased with a slight fluctuation, as shown in Figure 16b, which was attributed to the fact that the higher current density lowered the quantity of CO_2 inside the fuel cell and enhanced the accumu-

lation of CO_2 at the anode by the self-purging mechanism as mentioned above. For ΔR_{ctHOR}, it increased when the concentration of CO_2 increased at the cathode and the current density decreased (Figure 16c). The effect of current density was caused by the higher current density leading to the thinner carbonate layer in the outermost portion of the anode, which exposed more active sites for the reactants.

The threshold of CO_2 concentration and the effect of the fuel cell temperature on the ΔV_{CO_2} were also studied. It showed that even 5–10 ppm of CO_2 in the cathode or the anode feed gas

caused ca. 140 mV voltage drop at the current density of 1 A cm^{-2}. The results implied that the threshold of CO_2 concentration not causing the ΔV_{CO_2} was very low.[15a] Higher cell temperature decreased the ΔV_{CO_2} and the ΔASR because of the reduced CO_2 uptake in the fuel cell at elevated cell temperature.

The CO_2 quantity in the fuel cell system can be controlled by manipulating the flow rates of the feed gases, which was controlled to systematically investigate the CO_2 impact on the AEMFC performance.[15b] The effect of the cathode flow rate was examined with 400 ppm CO_2 in the cathode feed gas. As shown in Figure 16d, ΔASR, ΔV_{Nernst}, and ΔR_{ctHOR} were increased as the cathode flow rate increased. As a result, the ΔV_{CO_2} increased and was dominated by the ΔV_{Nernst} and ΔR_{ctHOR}.

On the contrary, the anode flow rate with 400 ppm CO_2 does not cause a substantial impact on the ΔV_{CO_2}, which merely decreased as the anode flow rate increased. The change of ΔV_{CO_2} was ascribed to the decreased ΔV_{Nernst} and ΔR_{ctHOR} because of the lower accumulation of CO_2 concentration at the anode.[15b] Finally, the authors identified that the symmetrical lowering of the anode and the cathode flow rates did not have a significant impact on the ΔV_{CO_2}.

The hydration conditions of cells were studied by adjusting the feed gas dew points and the water uptake of AEMs. Increasing the feed gas dew points decreased the CO_2 uptake in the cell and lowered the ΔV_{CO_2} because of the dilution effect caused by the increased water introduced to the cell through the feed gas.[15b] However, as the dew points increased to a critical point, the anode flooded, which led the authors to apply the second strategy, which was changing the cell hydration condition by employing high water uptake AEMs to balance the water content in the cell. The results implied that as the water uptake of the AEMs increased, the overall ΔV_{CO_2} decreased from 300 to 254 mV.

After the systematic study to minimize the ΔV_{CO_2}, the authors proposed an optimized operating condition of cell temperature at 80 °C with the dew points of anode/cathode at 78/80 °C and the flow rate of anode/cathode at 1/0.2 L min^{-1}, respectively. Then, they reported the AEMFC performance under the conditions mentioned above by varying the CO_2 concentrations in the cathode gas. The corresponding result showed that the power density at 0.6 V of the AEMFC using the cathode gas containing the CO_2 concentration of 400 ppm was only 20% lower than that of the CO_2-free counterpart. Under the above-mentioned conditions, the ΔV_{CO_2} was 182 mV, half the value previously reported, with 400 ppm CO_2 concentration in the cathode feed gas.[15a,b] Therefore, the results demonstrated that an operation of AEMFC under higher CO_2 concentrations (e.g.,400 ppm) was achieved without severe performance loss by tuning the operating conditions, such as cell temperature, anode/cathode flow rates, and dew point temperatures.

The properties of the membranes are also factors that impact (bi)carbonate transport in AEMFCs. Zheng et al. studied two sets of AEMs with different thicknesses and compositions.[15c] The chosen AEMs were 10/20 μm GT-78-15 and 15/25 μm LDPE-BTMA. The results showed that in each set, a thicker membrane, in which more charge-carrying groups were included, led to a lower ΔV_{CO_2}, ΔV_{Nernst}, and ΔR_{ctHOR} but a higher ΔASR (Figure 16e). The reasons were that the more charge-carrying groups in the membranes uptook more CO_2 and led to a higher degree of carbonation of the membranes, which reduced the ac-

cumulation of carbonate at the anode. The thicker membrane also relaxed the carbonate concentration gradient, which was considered a positive effect in mitigating CO_2 impacts at the anode.

As discussed above, in Section 4, the properties of the cationic group properties and polymer backbone are the fundamental determinants of the AEM. Accordingly, the influence of different structures of AEMs on the ΔV_{CO_2} was also studied. Six AEMs with different thicknesses ranging from 10 to 15 μm, conductivity from 138 to 208 mS cm^{-1}, and crystallinity from 0 to 23%, were studied.[15c] The results showed that the membrane with lower crystallinity and lower ionic conductivity had a lower ΔV_{CO_2} (Figure 16f). In this study, the lowest voltage loss (ca. 250 mV) belonged to GT-78-15 with a poly(norbornene) copolymer structure.[15c,139b] The further deconvolution analysis of the ΔV_{CO_2} showed that ΔV_{Nernst} was its dominant factor.

6. Summary and Perspectives

AEMFCs have a wide range of potential applications: the aerospace industry, stationary electric power suppliers, transportation, etc. In addition, according to the OSET mechanism for ORR in alkaline media, a variety of PGM-free materials can be used as the cathode catalysts in AEMFCs. Currently, a peak power density of 1.5 W cm^{-2} has been achieved with a PGM-free cathode electrocatalyst (CF-VC) in H_2/O_2 AEMFCs at 70 °C.[71c]

There are relatively fewer studies on HOR catalysts than on ORR catalysts in alkaline media. The most widely used HOR catalyst in AEMFCs is the PtRu/C, which has better HOR activity than the Pt/C catalyst. The reasons for this activity improvement are attributed to the fact that Ru reduces the hydrogen binding energy and/or participates in the formation of a bifunctional catalytic surface.[13] The research on PGM-free HOR catalysts is mainly focused on Ni-based catalysts. However, the development of PGM-free HOR catalysts capable of replacing the PtRu/C catalyst is still a long way off.

Both anion exchange membranes and ionomers have played an important role in the recent development of AEMFCs. However, the stability and ionic conductivity of membranes and ionomers can be further improved to make AEMFCs more competitive with PEMFCs. Recently, the application of phase-aggregated and radiation-grafted AEMs has dramatically improved the performance of AEMFCs. The new generation AEMs allow the fuel cells to operate at a high temperature (i.e., 95 °C) and to achieve peak power densities of 2.5 to 3.5 W cm^{-2} with noble metal catalysts.[22,23,68a,147] In addition, the interaction between ionomers and catalysts also has an impact on fuel cell performance.[158d]

Controlling the operating conditions of AEMFCs is more complicated than that of PEMFCs. Because water is generated and consumed asymmetrically in AEMFCs, water management affects the performance of AEMFCs more than that of PEMFCs. The formation and accumulation of HCO_3^- and CO_3^{2-} anions in the cell pose additional challenges in AEMFCs when the cathode feed gas is switched to ambient air. Water management can be optimized by controlling the operating conditions, using highly ion-conductive AEMs, and constructing optimized electrode structures with a higher tolerance for water by adjusting the carbon and ionomer content.[19] The limitations caused by CO_2 can also

be mitigated by operating the AEMFCs at high current density, elevated cell temperature, low cathode flow rate, and high dew points of the feed gas.[15b]

Future research on AEMFCs should focus on the following challenges:

1) The sluggish HOR kinetics of non-PGM catalysts require the development of novel and affordable materials to lower the overpotential of the reaction and to improve the energy efficiency of the AEMFCs. The PGM-based materials (Pt and Ru) are commonly used in AEMFCs as anode catalysts. However, non-PGM materials are rarely used as anode catalysts in AEMFCs. Ni-based materials are the most investigated non-PGM materials. The other transition metal elements, such as Fe and Co, are also worthy of investigation as catalysts or as metal/nitrogen/carbon-type substrates with metal nanoparticles, such as Pt and Ru, to find suitable materials for the anode of AEMFCs.

2) The stability of AEMs and ionomers should be extended to 80 °C or higher. High cell temperature can improve ionic conductivity and mitigate the effects of CO_2 on AEMFCs. To improve the stability, the decay mechanisms of AEMs and ionomers are crucial aspects that researchers should focus on. Based on the decomposition mechanisms of AEMs and ionomers, the proper backbones and cationic groups of AEMs and ionomers can be designed.

3) The properties of AEMs and AEIs should achieve a good balance between chemical stability, anion conductivity, and mechanical stability to obtain high-performance AEMFCs. Especially for AEIs, the adsorption of AEIs on catalyst surfaces should be minimized to avoid the poisoning effect of AEIs on the catalyst activities.

4) Long-term operation is required for AEMFCs, especially for industrial applications. Large-scale commercialization of AEMFCs requires highly stable catalysts and membranes to withstand operating conditions. Water control is another aspect of ensuring the long-term operation of AEMFCs by adjusting the cell operation parameters and optimizing the electrode structures.

5) The triple-phase interface is the most important aspect of AEMFCs that determines the performance of the cell during operation. Advanced characterization methods, such as X-ray absorption spectroscopy, computed tomography scans, and neutron radiography, should be included in the research of AEMFCs to perform in-situ/operando experiments. These technologies can provide insight into the triple-phase interface and additional information on the mass contribution of AEMFCs.

6) The critical challenge for AEMFCs, similar to PEMFCs,[168] is translating the high intrinsic activity of the materials shown in the half-cell test into single-cell performance. This includes preventing the ionomer poisoning of the catalysts, optimizing the electrode structure to improve mass transport, and managing water to minimize the difference between the intrinsic and single-cell performance.

7) Computational methods are also helpful in the development of AEMFCs. DFT computational models, combined with the linear combination fitting, can help to determine the structures of active site moieties in catalysts. By using the electro-

chemical theory, the active site models, and artificial intelligence, the catalyst screening can be easily performed to find suitable materials for AEMs.[185] Molecular dynamics (MD) simulation can be used to simulate the mass distribution and the conditions inside the cell.

8) Since AEMFCs are a promising technology for use in aircraft, aerospace, and vehicles, it is important to systematically investigate AEMFCs under extreme conditions such as low gravity, low temperature, and low pressure to expand their applicability.

Conflict of Interest

The authors declare no conflict of interest.

[1] a) T. J. Omasta, L. Wang, X. Peng, C. A. Lewis, J. R. Varcoe, W. E. Mustain, *J. Power Sources* **2018**, *375*, 205; b) Y. Wang, D. F. Ruiz Diaz, K. S. Chen, Z. Wang, X. C. Adroher, *Mater. Today* **2020**, *32*, 178.

[2] a) T. Yoshida, K. Kojima, *Electrochem. Soc. Interface* **2015**, *24*, 45; b) M. Shao, Q. Chang, J.-P. Dodelet, R. Chenitz, *Chem. Rev.* **2016**, *116*, 3594; c) O. Saritas, D. Meissner, A. Sokolov, *J. Knowl. Econ.* **2019**, *10*, 1183.

[3] X. Lü, Y. Wu, J. Lian, Y. Zhang, C. Chen, P. Wang, L. Meng, *Energy Conv. Manag.* **2020**, *205*, 112474.

[4] https://www.hydrogen.energy.gov/docs/hydrogenprogramlibraries/pdfs/review22/fc353_james_2022_o-pdf.pdf?Status=Master (accessed: October 2024).

[5] a) Z. Chen, D. Higgins, A. Yu, L. Zhang, J. Zhang, *Energy Environ. Sci.* **2011**, *4*, 3167; b) Y. He, Q. Tan, L. Lu, J. Sokolowski, G. Wu, *Electrochem. Energy Rev.* **2019**, *2*, 231; c) R. L. Borup, A. Kusoglu, K. C. Neyerlin, R. Mukundan, R. K. Ahluwalia, D. A. Cullen, K. L. More, A. Z. Weber, D. J. Myers, *Curr. Opin. Electrochem.* **2020**, *21*, 192.

[6] J. St-Pierre, N. Jia, *J. New Mat. Electrochem. Syst.* **2002**, *5*, 263.

[7] a) S. Gottesfeld, D. R. Dekel, M. Page, C. Bae, Y. Yan, P. Zelenay, Y. S. Kim, *J. Power Sources* **2018**, *375*, 170; b) H. A. Firouzjaie, W. E. Mustain, *ACS Catal.* **2019**, *10*, 225; c) W. E. Mustain, *Curr. Opin. Electrochem.* **2018**, *12*, 233; d) J. R. Varcoe, P. Atanassov, D. R. Dekel, A. M. Herring, M. A. Hickner, P. A. Kohl, A. R. Kucernak, W. E. Mustain, K. Nijmeijer, K. Scott, T. Xu, L. Zhuang, *Energy Environ. Sci.* **2014**, *7*, 3135; e) A. Sarapuu, E. Kibena-Põldsepp, M. Borghei,

K. Tammeveski, *J. Mater. Chem. A* **2018**, *6*, 776; f) D. R. Dekel, *J. Power Sources* **2018**, *375*, 158; g) W. E. Mustain, M. Chatenet, M. Page, Y. S. Kim, *Energy Environ. Sci.* **2020**, *13*, 2805; h) S. Noh, J. Y. Jeon, S. Adhikari, Y. S. Kim, C. Bae, *Accounts Chem. Res.* **2019**, *52*, 2745.

[8] a) N. Ramaswamy, S. Mukerjee, *Chem. Rev.* **2019**, *119*, 11945; b) N. Ramaswamy, S. Mukerjee, *J. Phys. Chem. C* **2011**, *115*, 18015.

[9] S. T. Thompson, D. Peterson, D. Ho, D. Papageorgopoulos, *J. Electrochem. Soc.* **2020**, *167*, 084514.

[10] N. Ziv, W. E. Mustain, D. R. Dekel, *ChemSusChem* **2018**, *11*, 1136.

[11] J. R. Varcoe, R. C. T. Slade, *Fuel Cells* **2005**, *5*, 187.

[12] S. Lu, J. Pan, A. Huang, L. Zhuang, J. Lu, *Proc. Natl. Acad. Sci. U.S.A.* **2008**, *105*, 20611.

[13] Y. Wang, G. Wang, G. Li, B. Huang, J. Pan, Q. Liu, J. Han, L. Xiao, J. Lu, L. Zhuang, *Energy Environ. Sci.* **2015**, *8*, 177.

[14] a) L. Wang, J. J. Brink, J. R. Varcoe, *Chem. Commun.* **2017**, *53*, 11771; b) N. Ul Hassan, M. Mandal, G. Huang, H. A. Firouzjaie, P. A. Kohl, W. E. Mustain, *Adv. Energy Mater.* **2020**, *10*, 2001986.

[15] a) Y. Zheng, T. J. Omasta, X. Peng, L. Wang, J. R. Varcoe, B. S. Pivovar, W. E. Mustain, *Energy Environ. Sci.* **2019**, *12*, 2806; b) Y. Zheng, G. Huang, L. Wang, J. R. Varcoe, P. A. Kohl, W. E. Mustain, *J. Power Sources* **2020**, *467*, 228350; c) Y. Zheng, L. N. Irizarry Colón, N. Ul Hassan, E. R. Williams, M. Stefik, J. M. LaManna, D. S. Hussey, W. E. Mustain, *Membranes* **2021**, *11*, 102.

[16] S. D. Poynton, R. C. T. Slade, T. J. Omasta, W. E. Mustain, R. Escudero-Cid, P. Ocón, J. R. Varcoe, *J. Mater. Chem. A* **2014**, *2*, 5124.

[17] J. Pan, C. Chen, Y. Li, L. Wang, L. Tan, G. Li, X. Tang, L. Xiao, J. Lu, L. Zhuang, *Energy Environ. Sci.* **2014**, *7*, 354.

[18] H. A. Miller, A. Lavacchi, F. Vizza, M. Marelli, F. Di Benedetto, F. D'Acapito, Y. Paska, M. Page, D. R. Dekel, *Angew. Chem., Int. Ed.* **2016**, *55*, 6004.

[19] T. J. Omasta, A. M. Park, J. M. LaManna, Y. Zhang, X. Peng, L. Wang, D. L. Jacobson, J. R. Varcoe, D. S. Hussey, B. S. Pivovar, W. E. Mustain, *Energy Environ. Sci.* **2018**, *11*, 551.

[20] X. Peng, T. J. Omasta, E. Magliocca, L. Wang, J. R. Varcoe, W. E. Mustain, *Angew. Chem., Int. Ed.* **2019**, *58*, 1046.

[21] Y. Yang, H. Peng, Y. Xiong, Q. Li, J. Lu, L. Xiao, F. J. DiSalvo, L. Zhuang, H. D. Abruña, *ACS Energy Lett.* **2019**, *4*, 1251.

[22] J. Wang, Y. Zhao, B. P. Setzler, S. Rojas-Carbonell, C. Ben Yehuda, A. Amel, M. Page, L. Wang, K. Hu, L. Shi, S. Gottesfeld, B. Xu, Y. Yan, *Nat. Energy* **2019**, *4*, 392.

[23] M. Mandal, G. Huang, N. U. Hassan, X. Peng, T. Gu, A. H. Brooks-Starks, B. Bahar, W. E. Mustain, P. A. Kohl, *J. Electrochem. Soc.* **2019**, *167*, 054501.

[24] H. Adabi, A. Shakouri, N. Ul Hassan, J. R. Varcoe, B. Zulevi, A. Serov, J. R. Regalbuto, W. E. Mustain, *Nat. Energy* **2021**, *6*, 834.

[25] N. Chen, H. H. Wang, S. P. Kim, H. M. Kim, W. H. Lee, C. Hu, J. Y. Bae, E. S. Sim, Y.-C. Chung, J.-H. Jang, S. J. Yoo, Y. Zhuang, Y. M. Lee, *Nat. Commun.* **2021**, *12*, 2367.

[26] N. Chen, C. Hu, H. H. Wang, S. P. Kim, H. M. Kim, W. H. Lee, J. Y. Bae, J. H. Park, Y. M. Lee, *Angew. Chem., Int. Ed.* **2021**, *60*, 7710.

[27] W. Ni, T. Wang, F. Héroguel, A. Krammer, S. Lee, L. Yao, A. Schüler, J. S. Luterbacher, Y. Yan, X. Hu, *Nat. Mater.* **2022**, *21*, 804.

[28] Y. Gao, Y. Yang, R. Schimmenti, E. Murray, H. Peng, Y. Wang, C. Ge, W. Jiang, G. Wang, F. J. DiSalvo, D. A. Muller, M. Mavrikakis, L. Xiao, H. D. Abruña, L. Zhuang, *Proc. Natl. Acad. Sci. U.S.A.* **2022**, *119*, 2119883119.

[29] W. Ni, J. L. Meibom, N. U. Hassan, M. Chang, Y.-C. Chu, A. Krammer, S. Sun, Y. Zheng, L. Bai, W. Ma, S. Lee, S. Jin, J. S. Luterbacher, A. Schüler, H. M. Chen, W. E. Mustain, X. Hu, *Nat. Catal.* **2023**, *6*, 773.

[30] Y. Ma, C. Hu, G. Yi, Z. Jiang, X. Su, Q. Liu, J. Y. Lee, S. Y. Lee, Y. M. Lee, Q. Zhang, *Angew. Chem., Int. Ed.* **2023**, *62*, 202311509.

[31] W. Xu, R. Zeng, M. Rebarchik, A. Posada-Borbón, H. Li, C. J. Pollock, M. Mavrikakis, H. D. Abruña, *J. Am. Chem. Soc.* **2024**, *146*, 2593.

[32] X. Zhong, L. Sui, M. Yang, T. Koketsu, M. Klingenhof, S. Selve, K. G. Reeves, C. Ge, L. Zhuang, W. H. Kan, M. Avdeev, M. Shu, N. Alonso-Vante, J. M. Chen, S. C. Haw, C. W. Pao, Y. C. Chang, Y. Huang, Z. Hu, P. Strasser, J. Ma, *Nat. Catal.* **2024**, *7*, 546.

[33] P. Han, X. Yang, L. Wu, H. Jia, J. Chen, W. Shi, G. Cheng, W. Luo, *Adv. Mater.* **2024**, *36*, 2304496.

[34] C. Hu, N. Y. Kang, H. W. Kang, J. Y. Lee, X. Zhang, Y. J. Lee, S. W. Jung, J. H. Park, M. G. Kim, S. J. Yoo, S. Y. Lee, C. H. Park, Y. M. Lee, *Angew. Chem., Int. Ed.* **2024**, *63*, 202316697.

[35] A. J. Bard, L. R. Faulkner, *Electrochemical Methods: Fundamentals and Applications*, John Wiley & Sons, Inc, New York **2001**.

[36] a) K. Elbert, J. Hu, Z. Ma, Y. Zhang, G. Chen, W. An, P. Liu, H. S. Isaacs, R. R. Adzic, J. X. Wang, *ACS Catal.* **2015**, *5*, 6764; b) P. J. Rheinländer, J. Herranz, J. Durst, H. A. Gasteiger, *J. Electrochem. Soc.* **2014**, *161*, F1448.

[37] a) C. A. Campos-Roldán, N. Alonso-Vante, *Electrochem. Energy Rev.* **2019**, *2*, 312; b) J. Durst, A. Siebel, C. Simon, F. Hasché, J. Herranz, H. A. Gasteiger, *Energy Environ. Sci.* **2014**, *7*, 2255; c) W. Sheng, M. Myint, J. G. Chen, Y. Yan, *Energy Environ. Sci.* **2013**, *6*, 1509; d) J. Zheng, W. Sheng, Z. Zhuang, B. Xu, Y. Yan, *Sci. Adv.* **2016**, *2*, 1501602.

[38] a) D. Strmcnik, M. Uchimura, C. Wang, R. Subbaraman, N. Danilovic, D. van der Vliet, A. P. Paulikas, V. R. Stamenkovic, N. M. Markovic, *Nat. Chem.* **2013**, *5*, 300; b) N. Ramaswamy, S. Ghoshal, M. K. Bates, Q. Jia, J. Li, S. Mukerjee, *Nano Energy* **2017**, *41*, 765; c) S. M. Alia, B. S. Pivovar, Y. Yan, *J. Am. Chem. Soc.* **2013**, *135*, 13473.

[39] M. T. M. Koper, *Nat. Chem.* **2013**, *5*, 255.

[40] a) H. Wang, H. D. Abruña, *J. Am. Chem. Soc.* **2017**, *139*, 6807; b) W. Sheng, Z. Zhuang, M. Gao, J. Zheng, J. G. Chen, Y. Yan, *Nat. Commun.* **2015**, *6*, 5848.

[41] J. Li, S. Ghoshal, M. K. Bates, T. E. Miller, V. Davies, E. Stavitski, K. Attenkofer, S. Mukerjee, Z.-F. Ma, Q. Jia, *Angew. Chem., Int. Ed.* **2017**, *56*, 15594.

[42] a) Z. Ma, Z. P. Cano, A. Yu, Z. Chen, G. Jiang, X. Fu, L. Yang, T. Wu, Z. Bai, J. Lu, *Angew. Chem., Int. Ed.* **2020**, *59*, 18334; b) S. Guo, S. Zhang, S. Sun, *Angew. Chem., Int. Ed.* **2013**, *52*, 8526.

[43] K. Wan, Z. Yu, X. Li, M. Liu, G. Yang, J. Piao, Z. Liang, *ACS Catal.* **2015**, *5*, 4325.

[44] a) E. Janin, H. von Schenck, M. Göthelid, U. O. Karlsson, M. Svensson, *Phys. Rev. B* **2000**, *61*, 13144; b) C. Zhang, F. R. F. Fan, A. J. Bard, *J. Am. Chem. Soc.* **2009**, *131*, 177.

[45] a) J. R. Goldstein, A. C. C. Tseung, *J. Catal.* **1974**, *32*, 452; b) O. Špalek, J. Balej, I. Paseka, *J. Chem. Soc., Faraday Trans. 1* **1982**, *78*, 2349; c) J. Abbot, D. G. Brown, *Int. J. Chem. Kinet.* **1990**, *22*, 963.

[46] a) P. Fischer, J. Heitbaum, *J. Electroanal. Chem. Interfacial Electrochem.* **1980**, *112*, 231; b) S. M. Park, S. Ho, S. Aruliah, M. F. Weber, C. A. Ward, R. D. Venter, S. Srinivasan, *J. Electrochem. Soc.* **2019**, *133*, 1641; c) K. A. Striebel, *J. Electrochem. Soc.* **1990**, *137*, 3351; d) C. F. Zinola, A. M. Castro Luna, W. E. Triaca, A. J. Arvia, *J. Appl. Electrochem.* **1994**, *24*, 531.

[47] a) M. Lefèvre, E. Proietti, F. Jaouen, J.-P. Dodelet, *Science* **2009**, *324*, 71; b) N. Ramaswamy, U. Tylus, Q. Jia, S. Mukerjee, *J. Am. Chem. Soc.* **2013**, *135*, 15443; c) L. Wang, X. Wan, S. Liu, L. Xu, J. Shui, *J. Energy Chem.* **2019**, *39*, 77; d) H. A. Firouzjaie, W. E. Mustain, *ACS Catal.* **2020**, *10*, 225.

[48] a) E. S. Davydova, S. Mukerjee, F. Jaouen, D. R. Dekel, *ACS Catal.* **2018**, *8*, 6665; b) Y. Cong, B. Yi, Y. Song, *Nano Energy* **2018**, *44*, 288.

[49] S. Lu, Z. Zhuang, *J. Am. Chem. Soc.* **2017**, *139*, 5156.

[50] a) J. Ohyama, T. Sato, Y. Yamamoto, S. Arai, A. Satsuma, *J. Am. Chem. Soc.* **2013**, *135*, 8016; b) L. Zeng, H. Peng, W. Liu, J. Yin, L.

Xiao, J. Lu, L. Zhuang, *J. Power Sources* **2020**, *461*, 228147; c) J. Nash, J. Zheng, Y. Wang, B. Xu, Y. Yan, *J. Electrochem. Soc.* **2018**, *165*, J3378.

[51] a) M. Alesker, M. Page, M. Shviro, Y. Paska, G. Gershinsky, D. R. Dekel, D. Zitoun, *J. Power Sources* **2016**, *304*, 332; b) H. A. Miller, F. Vizza, M. Marelli, A. Zadick, L. Dubau, M. Chatenet, S. Geiger, S. Cherevko, H. Doan, R. K. Pavlicek, S. Mukerjee, D. R. Dekel, *Nano Energy* **2017**, *33*, 293; c) T. J. Omasta, X. Peng, H. A. Miller, F. Vizza, L. Wang, J. R. Varcoe, D. R. Dekel, W. E. Mustain, *J. Electrochem. Soc.* **2018**, *165*, J3039; d) M. Bellini, M. V. Pagliaro, A. Lenarda, P. Fornasiero, M. Marelli, C. Evangelisti, M. Innocenti, Q. Jia, S. Mukerjee, J. Jankovic, L. Wang, J. R. Varcoe, C. B. Krishnamurthy, I. Grinberg, E. Davydova, D. R. Dekel, H. A. Miller, F. Vizza, *ACS Appl. Energy Mater.* **2019**, *2*, 4999.

[52] a) Q. Hu, G. Li, J. Pan, L. Tan, J. Lu, L. Zhuang, *Int. J. Hydrog. Energy* **2013**, *38*, 16264; b) L. Gao, Y. Wang, H. Li, Q. Li, N. Ta, L. Zhuang, Q. Fu, X. Bao, *Chem. Sci.* **2017**, *8*, 5728; c) S. Kabir, K. Lemire, K. Artyushkova, A. Roy, M. Odgaard, D. Schlueter, A. Oshchepkov, A. Bonnefont, E. Savinova, D. C. Sabarirajan, P. Mandal, E. J. Crumlin, I. V. Zenyuk, P. Atanassov, A. Serov, *J. Mater. Chem. A* **2017**, *5*, 24433; d) A. Roy, M. R. Talarposhti, S. J. Normile, I. V. Zenyuk, V. De Andrade, K. Artyushkova, A. Serov, P. Atanassov, *Sustain. Energy Fuels* **2018**, *2*, 2268; e) G. Wang, W. Li, B. Huang, L. Xiao, J. Lu, L. Zhuang, *ACS Appl. Energy Mater.* **2019**, *2*, 3160; f) Y. Pan, G. Hu, J. Lu, L. Xiao, L. Zhuang, *J. Energy Chem.* **2019**, *29*, 111; g) Y. Gao, H. Peng, Y. Wang, G. Wang, L. Xiao, J. Lu, L. Zhuang, *ACS Appl. Mater. Interfaces* **2020**, *12*, 31575.

[53] T. Ioroi, Z. Siroma, S.-i. Yamazaki, K. Yasuda, *Adv. Energy Mater.* **2019**, *9*, 1801284.

[54] a) K. C. Neyerlin, W. Gu, J. Jorne, H. A. Gasteiger, *J. Electrochem. Soc.* **2007**, *154*, B631; b) W. Sheng, H. A. Gasteiger, Y. Shao-Horn, *J. Electrochem. Soc.* **2010**, *157*, B1529.

[55] H. Adabi, A. Shakouri, A. Zitolo, T. Asset, A. Khan, J. Bohannon, R. Chattot, C. Williams, F. Jaouen, J. R. Regalbuto, W. E. Mustain, *Appl. Catal. B-Environ.* **2023**, *325*, 122375.

[56] Y. Zhao, F. Yang, W. Zhang, Q. Li, X. Wang, L. Su, X. Hu, Y. Wang, Z. Wang, L. Zhuang, S. Chen, W. Luo, *CCS Chemistry* **2022**, *4*, 1732.

[57] Y. Xue, L. Shi, X. Liu, J. Fang, X. Wang, B. P. Setzler, W. Zhu, Y. Yan, Z. Zhuang, *Nat. Commun.* **2020**, *11*, 5651.

[58] C. Yang, Y. Li, C. Ge, W. Jiang, G. Cheng, L. Zhuang, W. Luo, *Chin. J. Chem.* **2022**, *40*, 2495.

[59] Z. Cui, Z. Ren, C. Ma, B. Chen, G. Chen, R. Lu, W. Zhu, T. Gan, Z. Wang, Z. Zhuang, Y. Han, *Angew. Chem., Int. Ed.* **2024**, *63*, 202404761.

[60] a) H. Yu, E. S. Davydova, U. Ash, H. A. Miller, L. Bonville, D. R. Dekel, R. Maric, *Nano Energy* **2019**, *57*, 820; b) V. Yarmiayev, M. Alesker, A. Muzikansky, M. Zysler, D. Zitoun, *J. Electrochem. Soc.* **2019**, *166*, F3234; c) N. Ralbag, E. S. Davydova, M. Mann-Lahav, P. Cong, J. He, A. M. Beale, G. S. Grader, D. Avnir, D. R. Dekel, *J. Electrochem. Soc.* **2020**, *167*, 054514; d) R. K. Singh, E. S. Davydova, J. Douglin, A. O. Godoy, H. Tan, M. Bellini, B. J. Allen, J. Jankovic, H. A. Miller, A. C. Alba-Rubio, D. R. Dekel, *Adv. Funct. Mater.* **2020**, *30*, 2002087; e) H. A. Miller, M. Bellini, D. R. Dekel, F. Vizza, *Electrochem. Commun.* **2022**, *135*, 107219; f) V. M Truong, J. Richard Tolchard, J. Svendby, M. Manikandan, H. A. Miller, S. Sunde, H. Yang, D. R. Dekel, A. O Barnett, *Energies* **2020**, *13*, 582.

[61] a) Z. A. Feng, F. El Gabaly, X. Ye, Z.-X. Shen, W. C. Chueh, *Nat. Commun.* **2014**, *5*, 4374; b) K. P. Kepp, *Inorg. Chem.* **2016**, *55*, 9461.

[62] H. A. Miller, M. V. Pagliaro, M. Bellini, F. Bartoli, L. Wang, I. Salam, J. R. Varcoe, F. Vizza, *ACS Appl. Energy Mater.* **2020**, *3*, 10209.

[63] F.-Y. Gao, M.-R. Gao, *Accounts Chem. Res.* **2023**, *56*, 1445.

[64] a) P. Han, X. Yang, L. Wu, H. Jia, W. Luo, *Chem. Sci.* **2024**, *15*, 5633; b) R. Ren, C. Ge, Q. Li, G. Wang, L. Xiao, J. Lu, L. Zhuang, *J. Power Sources* **2023**, *556*, 232439.

[65] X. Tian, R. Ren, F. Wei, J. Pei, Z. Zhuang, L. Zhuang, W. Sheng, *Nat. Commun.* **2024**, *15*, 76.

[66] a) Z. Cui, R. G. Burns, F. J. DiSalvo, *Chem. Mat.* **2013**, *25*, 3782; b) Y. Zhong, X. Xia, F. Shi, J. Zhan, J. Tu, H. J. Fan, *Adv. Sci.* **2016**, *3*, 1500286; c) J. Zheng, W. Zhang, J. Zhang, M. Lv, S. Li, H. Song, Z. Cui, L. Du, S. Liao, *J. Mater. Chem. A* **2020**, *8*, 20803; d) H. Wang, J. Li, K. Li, Y. Lin, J. Chen, L. Gao, V. Nicolosi, X. Xiao, J.-M. Lee, *Chem. Soc. Rev.* **2021**, *50*, 1354; e) R. Zeng, Y. Yang, X. Feng, H. Li, L. M. Gibbs, F. J. DiSalvo, H. D. Abruña, *Sci. Adv.* **2022**, *8*, eabj1584; f) X.-L. Zhang, S.-J. Hu, Y.-H. Wang, L. Shi, Y. Yang, M.-R. Gao, *Nano Lett.* **2023**, *23*, 107.

[67] Y. Wang, H. Su, Y. He, L. Li, S. Zhu, H. Shen, P. Xie, X. Fu, G. Zhou, C. Feng, D. Zhao, F. Xiao, X. Zhu, Y. Zeng, M. Shao, S. Chen, G. Wu, J. Zeng, C. Wang, *Chem. Rev.* **2020**, *120*, 12217.

[68] a) L. Wang, X. Peng, W. E. Mustain, J. R. Varcoe, *Energy Environ. Sci.* **2019**, *12*, 1575; b) H. Peng, Q. Li, M. Hu, L. Xiao, J. Lu, L. Zhuang, *J. Power Sources* **2018**, *390*, 165.

[69] F.-Y. Gao, S.-N. Liu, J.-C. Ge, X.-L. Zhang, L. Zhu, Y.-R. Zheng, Y. Duan, S. Qin, W. Dong, X. Yu, R.-C. Bao, P.-P. Yang, Z.-Z. Niu, Z.-G. Ding, W. Liu, S. Lan, M.-R. Gao, Y. Yan, S.-H. Yu, *Nat. Catal.* **2022**, *5*, 993.

[70] Q. Li, H. Peng, Y. Wang, L. Xiao, J. Lu, L. Zhuang, *Angew. Chem., Int. Ed.* **2019**, *58*, 1442.

[71] a) I. Kruusenberg, L. Matisen, Q. Shah, A. M. Kannan, K. Tammeveski, *Int. J. Hydrog. Energy* **2012**, *37*, 4406; b) S. Gu, W. Sheng, R. Cai, S. M. Alia, S. Song, K. O. Jensen, Y. Yan, *Chem. Commun.* **2013**, *49*, 131; c) X. Peng, V. Kashyap, B. Ng, S. Kurungot, L. Wang, J. Varcoe, W. Mustain, *Catalysts* **2019**, *9*, 264; d) Y. Wang, Y. Yang, S. Jia, X. Wang, K. Lyu, Y. Peng, H. Zheng, X. Wei, H. Ren, L. Xiao, J. Wang, D. A. Muller, H. D. Abruna, B. J. Hwang, J. Lu, L. Zhuang, *Nat. Commun.* **2019**, *10*, 1506; e) S. Kabir, A. Serov, P. Atanassov, *J. Power Sources* **2018**, *375*, 255.

[72] a) F. L. Meng, Z. L. Wang, H. X. Zhong, J. Wang, J. M. Yan, X. B. Zhang, *Adv. Mater.* **2016**, *28*, 7948; b) I. Kruusenberg, D. Ramani, S. Ratso, U. Joost, R. Saar, P. Rauwel, A. M. Kannan, K. Tammeveski, *ChemElectroChem* **2016**, *3*, 1455; c) Y. J. Sa, D. J. Seo, J. Woo, J. T. Lim, J. Y. Cheon, S. Y. Yang, J. M. Lee, D. Kang, T. J. Shin, H. S. Shin, H. Y. Jeong, C. S. Kim, M. G. Kim, T. Y. Kim, S. H. Joo, *J. Am. Chem. Soc.* **2016**, *138*, 15046; d) H. Ren, Y. Wang, Y. Yang, X. Tang, Y. Peng, H. Peng, L. Xiao, J. Lu, H. D. Abruña, L. Zhuang, *ACS Catal.* **2017**, *7*, 6485; e) Y. Mun, M. J. Kim, S.-A. Park, E. Lee, Y. Ye, S. Lee, Y.-T. Kim, S. Kim, O.-H. Kim, Y.-H. Cho, Y.-E. Sung, J. Lee, *Appl. Catal. B-Environ.* **2018**, *222*, 191; f) J. Woo, S. Y. Yang, Y. J. Sa, W.-Y. Choi, M.-H. Lee, H.-W. Lee, T. J. Shin, T.-Y. Kim, S. H. Joo, *Chem. Mat.* **2018**, *30*, 6684; g) K.-C. Wang, H.-C. Huang, S.-T. Chang, C.-H. Wu, I. Yamanaka, J.-F. Lee, C.-H. Wang, *ACS Sustainable Chem. Eng.* **2019**, *7*, 9143; h) L. Cui, L. Cui, Z. Li, J. Zhang, H. Wang, S. Lu, Y. Xiang, *J. Mater. Chem. A* **2019**, *7*, 16690; i) M. M. Hossen, K. Artyushkova, P. Atanassov, A. Serov, *J. Power Sources* **2018**, *375*, 214; j) J. Lilloja, E. Kibena-Põldsepp, A. Sarapuu, M. Kodali, Y. Chen, T. Asset, M. Käärik, M. Merisalu, P. Paiste, J. Aruväli, A. Treshchalov, M. Rähn, J. Leis, V. Sammelselg, S. Holdcroft, P. Atanassov, K. Tammeveski, *ACS Appl. Energy Mater.* **2020**, *3*, 5375.

[73] a) Y. J. Sa, C. Park, H. Y. Jeong, S. H. Park, Z. Lee, K. T. Kim, G. G. Park, S. H. Joo, *Angew. Chem., Int. Ed.* **2014**, *53*, 4102; b) S. Lee, M. Choun, Y. Ye, J. Lee, Y. Mun, E. Kang, J. Hwang, Y. H. Lee, C. H. Shin, S. H. Moon, S. K. Kim, E. Lee, J. Lee, *Angew. Chem., Int. Ed.* **2015**, *54*, 9230; c) J. W. F. To, J. W. D. Ng, S. Siahrostami, A. L. Koh, Y. Lee, Z. Chen, K. D. Fong, S. Chen, J. He, W.-G. Bae, J. Wilcox, H. Y. Jeong, K. Kim, F. Studt, J. K. Nørskov, T. F. Jaramillo, Z. Bao, *Nano Res.* **2016**, *10*, 1163; d) Y. Lu, Y. Wang, K. Preuß, M. Qiao, M.-M. Titirici, J. Varcoe, Q. Cai, *J. Power Sources* **2017**, *372*, 82.

[74] H. Li, R. Zeng, X. Feng, H. Wang, W. Xu, X. Lu, Z. Xie, H. D. Abruña, *J. Am. Chem. Soc.* **2022**, *144*, 8106.

[75] W. Xu, D. Yoon, Y. Yang, Y. Xiong, H. Li, R. Zeng, D. A. Muller, H. D. Abruña, *ACS Appl. Mater. Interfaces* **2022**, *14*, 44735.

[76] Y. Xiong, Y. Yang, F. J. DiSalvo, H. D. Abruna, *J. Am. Chem. Soc.* **2019**, *141*, 10744.

[77] a) F. Lu, Y. Zhang, S. Liu, D. Lu, D. Su, M. Liu, Y. Zhang, P. Liu, J. X. Wang, R. R. Adzic, O. Gang, *J. Am. Chem. Soc.* **2017**, *139*, 7310; b) E. C. M. Tse, C. J. Barile, N. A. Kirchschlager, Y. Li, J. P. Gewargis, S. C. Zimmerman, A. Hosseini, A. A. Gewirth, *Nat. Mater.* **2016**, *15*, 754.

[78] C. Ge, Q. Li, M. Hu, G. Wang, L. Xiao, J. Lu, L. Zhuang, *J. Power Sources* **2022**, *520*, 230868.

[79] P. G. Santori, F. D. Speck, S. Cherevko, H. A. Firouzjaie, X. Peng, W. E. Mustain, F. Jaouen, *J. Electrochem. Soc.* **2020**, *167*, 134505.

[80] a) F. Jaouen, J.-P. Dodelet, *J. Phys. Chem. C* **2009**, *113*, 15422; b) A. Muthukrishnan, Y. Nabae, T. Okajima, T. Ohsaka, *ACS Catal.* **2015**, *5*, 5194; c) C. H. Choi, W. S. Choi, O. Kasian, A. K. Mechler, M. T. Sougrati, S. Brüller, K. Strickland, Q. Jia, S. Mukerjee, K. J. J. Mayrhofer, F. Jaouen, *Angew. Chem., Int. Ed.* **2017**, *56*, 8809; d) S. S. A. Shah, T. Najam, C. Cheng, L. Peng, R. Xiang, L. Zhang, J. Deng, W. Ding, Z. Wei, *Chem.-Eur. J.* **2018**, *24*, 10630; e) L. Osmieri, R. Escudero-Cid, A. H. A. Monteverde Videla, P. Ocón, S. Specchia, *Renew. Energy* **2018**, *115*, 226.

[81] a) Y. Yuan, J. Wang, S. Adimi, H. Shen, T. Thomas, R. Ma, J. P. Attfield, M. Yang, *Nat. Mater.* **2020**, *19*, 282; b) Z. Meng, S. Zheng, R. Luo, H. Tang, R. Wang, R. Zhang, T. Tian, H. Tang, *Nanomaterials* **2022**, *12*, 2660; c) Z.-G. Yang, H.-M. Xu, T.-Y. Shuai, Q.-N. Zhan, Z.-J. Zhang, K. Huang, C. Dai, G.-R. Li, *Nanoscale* **2023**, *15*, 11777.

[82] a) X.-F. Yang, A. Wang, B. Qiao, J. Li, J. Liu, T. Zhang, *Accounts Chem. Res.* **2013**, *46*, 1740; b) A. Wang, J. Li, T. Zhang, *Nat. Rev. Chem.* **2018**, *2*, 65; c) J. Lu, *Accounts Mater. Res.* **2022**, *3*, 358; d) X. Yang, W. Sun, J. Chen, Y. Gao, R. Zhang, Q. Luo, T. Lyu, L. Du, *J. Mater. Sci. Technol.* **2024**, *173*, 100; e) X. Yang, Z. Huang, L. Du, Q. Li, S. Ye, *ACS Catal.* **2024**, *14*, 15471.

[83] a) Y. Chen, S. Ji, C. Chen, Q. Peng, D. Wang, Y. Li, *Joule* **2018**, *2*, 1242; b) J. Wu, L. Xiong, B. Zhao, M. Liu, L. Huang, *Small Methods* **2020**, *4*, 1900540; c) A. Sarapuu, J. Lilloja, S. Akula, J. H. Zagal, S. Specchia, K. Tammeveski, *ChemCatChem* **2023**, *15*, 202300849.

[84] M. Rauf, J. Wang, S. Handschuh-Wang, Z. Zhou, I. Waheed, S. A. Khan, L. Zhuang, X. Ren, Y. Li, S. Sun, *Prog. Nat. Sci.: Mater. Int.* **2022**, *32*, 27.

[85] H. Adabi, P. G. Santori, A. Shakouri, X. Peng, K. Yassin, I. G. Rasin, S. Brandon, D. R. Dekel, N. U. Hassan, M.-T. Sougrati, A. Zitolo, J. R. Varcoe, J. R. Regalbuto, F. Jaouen, W. E. Mustain, *Mater. Today Adv.* **2021**, *12*, 100179.

[86] Z.-W. Chang, F.-L. Meng, H.-X. Zhong, X.-B. Zhang, *Chin. J. Chem.* **2018**, *36*, 287.

[87] S. Ratso, A. Zitolo, M. Käärik, M. Merisalu, A. Kikas, V. Kisand, M. Rähn, P. Paiste, J. Leis, V. Sammelselg, S. Holdcroft, F. Jaouen, K. Tammeveski, *Renew. Energy* **2021**, *167*, 800.

[88] K. Kisand, A. Sarapuu, J. C. Douglin, A. Kikas, A. Treshchalov, M. Käärik, H.-M. Piirsoo, P. Paiste, J. Aruväli, J. Leis, V. Kisand, A. Tamm, D. R. Dekel, K. Tammeveski, *ACS Catal.* **2022**, *12*, 14050.

[89] P. Teppor, R. Jäger, M. Koppel, O. Volobujeva, R. Palm, M. Månsson, E. Härk, Z. Kochovski, J. Aruväli, K. Kooser, S. Granroth, T. Käämbre, J. Nerut, E. Lust, *J. Power Sources* **2024**, *591*, 233816.

[90] R. Jasinski, *Nature* **1964**, *201*, 1212.

[91] a) A. Friedman, M. Mizrahi, N. Levy, N. Zion, M. Zachman, L. Elbaz, *ACS Appl. Mater. Interfaces* **2021**, *13*, 58532; b) Y. Kumar, E. Kibena-Põldsepp, J. Kozlova, M. Rähn, A. Treshchalov, A. Kikas, V. Kisand, J. Aruväli, A. Tamm, J. C. Douglin, S. J. Folkman, I. Gelmetti, F. A. Garcés-Pineda, J. R. Galán-Mascarós, D. R. Dekel, K. Tammeveski, *ACS Appl. Mater. Interfaces* **2021**, *13*, 41507; c) R. Ren, X. Wang, H. Chen, H. A. Miller, I. Salam, J. R. Varcoe, L. Wu, Y. Chen, H.-G. Liao,

E. Liu, F. Bartoli, F. Vizza, Q. Jia, Q. He, *Angew. Chem., Int. Ed.* **2021**, *60*, 4049; d) N. Zion, J. C. Douglin, D. A. Cullen, P. Zelenay, D. R. Dekel, L. Elbaz, *Adv. Funct. Mater.* **2021**, *31*, 2100963.

[92] a) M. Mooste, E. Kibena-Põldsepp, V. Vassiljeva, A. Kikas, M. Käärik, J. Kozlova, V. Kisand, M. Külaviir, S. Cavaliere, J. Leis, A. Krumme, V. Sammelselg, S. Holdcroft, K. Tammeveski, *ChemCatChem* **2020**, *12*, 4568; b) J. Zhang, Y. Pei, W. Zhu, Y. Liu, Y. Yin, Y. Qin, M. D. Guiver, *J. Power Sources* **2021**, *484*, 229259; c) X. X. Wang, V. Prabhakaran, Y. He, Y. Shao, G. Wu, *Adv. Mater.* **2019**, *31*, 1805126.

[93] B. Britton, S. Holdcroft, *J. Electrochem. Soc.* **2016**, *163*, F353.

[94] a) K. Gong, F. Du, Z. Xia, M. Durstock, L. Dai, *Science* **2009**, *323*, 760; b) L. Yang, J. Shui, L. Du, Y. Shao, J. Liu, L. Dai, Z. Hu, *Adv. Mater.* **2019**, *31*, 1804799; c) R. Paul, L. Zhu, H. Chen, J. Qu, L. Dai, *Adv. Mater.* **2019**, *31*, 1806403.

[95] a) C. Liang, Z. Li, S. Dai, *Angew. Chem., Int. Ed.* **2008**, *47*, 3696; b) R. Liu, D. Wu, X. Feng, K. Müllen, *Angew. Chem., Int. Ed.* **2010**, *49*, 2565; c) H.-y. Lei, J.-h. Piao, A. Brouzgou, E. Gorbova, P. Tsiakaras, Z.-x. Liang, *Int. J. Hydrog. Energy* **2019**, *44*, 4423; d) K. Wan, A.-d. Tan, Z.-p. Yu, Z.-x. Liang, J.-h. Piao, P. Tsiakaras, *Appl. Catal. B-Environ.* **2017**, *209*, 447; e) A.-d. Tan, Y.-f. Wang, Z.-y. Fu, P. Tsiakaras, Z.-x. Liang, *Appl. Catal. B-Environ.* **2017**, *218*, 260; f) A. Eftekhari, Z. Fan, *Mat. Chem. Front.* **2017**, *1*, 1001.

[96] K. Kumar, L. Dubau, F. Jaouen, F. Maillard, *Chem. Rev.* **2023**, *123*, 9265.

[97] a) Y.-P. Ku, K. Kumar, A. Hutzler, C. Götz, M. Vorochta, M. T. Sougrati, V. Lloret, K. Ehelebe, K. J. J. Mayrhofer, S. Thiele, I. Khalakhan, T. Böhm, F. Jaouen, S. Cherevko, *ACS Catal.* **2024**, *14*, 8576; b) Y.-P. Ku, K. Ehelebe, A. Hutzler, M. Bierling, T. Böhm, A. Zitolo, M. Vorokhta, N. Bibent, F. D. Speck, D. Seeberger, I. Khalakhan, K. J. J. Mayrhofer, S. Thiele, F. Jaouen, S. Cherevko, *J. Am. Chem. Soc.* **2022**, *144*, 9753.

[98] a) N. Chen, Y. M. Lee, *Prog. Polym. Sci.* **2021**, *113*, 101345; b) Z. Tao, C. Wang, X. Zhao, J. Li, M. D. Guiver, *Adv. Mater. Technol.* **2021**, *6*, 2001220; c) B. Yang, Z. Cunman, *Chem. Eng. J.* **2023**, *457*, 141094.

[99] a) L. Zhu, J. Pan, C. M. Christensen, B. Lin, M. A. Hickner, *Macromolecules* **2016**, *49*, 3300; b) J. Pan, S. Lu, Y. Li, A. Huang, L. Zhuang, J. Lu, *Adv. Funct. Mater.* **2010**, *20*, 312; c) J. Wang, J. Wang, S. Zhang, *J. Membr. Sci.* **2012**, *415–416*, 205.

[100] a) W. K. Ng, W. Y. Wong, N. A. H. Rosli, K. S. Loh, *Separations* **2023**, *10*, 424; b) G. Merle, M. Wessling, K. Nijmeijer, *J. Membr. Sci.* **2011**, *377*, 1; c) D. Henkensmeier, M. Najibah, C. Harms, J. Žitka, J. Hnát, K. Bouzek, *J. Electrochem. Energy Convers. Storage* **2020**, *18*, 024001.

[101] a) Z. Sun, J. Pan, J. Guo, F. Yan, *Adv. Sci.* **2018**, *5*, 1800065; b) B. Lee, D. Yun, J.-S. Lee, C. H. Park, T.-H. Kim, *J. Phys. Chem. C* **2019**, *123*, 13508; c) Y. Liu, J. Wang, Y. Yang, T. M. Brenner, S. Seifert, Y. Yan, M. W. Liberatore, A. M. Herring, *J. Phys. Chem. C* **2014**, *118*, 15136; d) H. Long, B. Pivovar, *J. Phys. Chem. C* **2014**, *118*, 9880; e) F. Xu, Y. Li, J. Ding, B. Lin, *ChemElectroChem* **2023**, *10*, 202300445.

[102] a) C. Fujimoto, D.-S. Kim, M. Hibbs, D. Wrobleski, Y. S. Kim, *J. Membr. Sci.* **2012**, *423–424*, 438; b) C. G. Arges, V. Ramani, *Proc. Natl. Acad. Sci. U.S.A.* **2013**, *110*, 2490.

[103] a) J. S. Olsson, T. H. Pham, P. Jannasch, *Adv. Funct. Mater.* **2018**, *28*, 1702758; b) Y. Peng, Y. Wang, X. Wei, J. Zhou, H. Peng, L. Xiao, J. Lu, L. Zhuang, *ACS Appl. Energy Mater.* **2018**, *10*, 33581; c) L. Zhu, X. Peng, S. L. Shang, M. T. Kwasny, T. J. Zimudzi, X. Yu, N. Saikia, J. Pan, Z. K. Liu, G. N. Tew, W. E. Mustain, M. Yandrasits, M. A. Hickner, *Adv. Funct. Mater.* **2019**, *29*, 1902059.

[104] Y. Yang, C. R. Peltier, R. Zeng, R. Schimmenti, Q. Li, X. Huang, Z. Yan, G. Potsi, R. Selhorst, X. Lu, W. Xu, M. Tader, A. V. Soudackov, H. Zhang, M. Krumov, E. Murray, P. Xu, J. Hitt, L. Xu, H.-Y. Ko, B. G. Ernst, C. Bundschu, A. Luo, D. Markovich, M. Hu, C. He, H. Wang, J. Fang, R. A. DiStasio Jr., L. F. Kourkoutis, et al., *Chem. Rev.* **2022**, *122*, 6117.

[105] H. Chen, R. Tao, K.-T. Bang, M. Shao, Y. Kim, *Adv. Energy Mater.* **2022**, *12*, 2200934.

[106] S. Haj-Bsoul, J. R. Varcoe, D. R. Dekel, *J. Electroanal. Chem.* **2022**, *908*, 116112.

[107] a) B. Zhang, R. B. Kaspar, S. Gu, J. Wang, Z. Zhuang, Y. Yan, *ChemSusChem* **2016**, *9*, 2374; b) B. Zhang, H. Long, R. B. Kaspar, J. Wang, S. Gu, Z. Zhuang, B. Pivovar, Y. Yan, *RSC Adv.* **2018**, *8*, 26640; c) K. J. T. Noonan, K. M. Hugar, H. A. I. V. Kostalik, E. B. Lobkovsky, H. D. Abruña, G. W. Coates, *J. Am. Chem. Soc.* **2012**, *134*, 18161; d) M. Treichel, C. Tyler Womble, R. Selhorst, J. Gaitor, T. M. S. K. Pathiranage, T. Kowalewski, K. J. T. Noonan, *Macromolecules* **2020**, *53*, 8509.

[108] B. Zhang, S. Gu, J. Wang, Y. Liu, A. M. Herring, Y. Yan, *RSC Adv.* **2012**, *2*, 12683.

[109] a) T. Zhu, S. Xu, A. Rahman, E. Dogdibegovic, P. Yang, P. Pageni, M. P. Kabir, X.-d. Zhou, C. Tang, *Angew. Chem., Int. Ed.* **2018**, *57*, 2388; b) T. Zhu, Y. Sha, H. A. Firouzjaie, X. Peng, Y. Cha, D. M. M. M. Dissanayake, M. D. Smith, A. K. Vannucci, W. E. Mustain, C. Tang, *J. Am. Chem. Soc.* **2020**, *142*, 1083; c) K. Aggarwal, S. Li, S. Nijem, D. R. Dekel, C. E. Diesendruck, *Chem.-Eur. J.* **2024**, *30*, 202400029.

[110] P. Zuo, Z. Xu, Q. Zhu, J. Ran, L. Ge, X. Ge, L. Wu, Z. Yang, T. Xu, *Adv. Funct. Mater.* **2022**, *32*, 2207366.

[111] A. C. Yang-Neyerlin, S. Medina, K. M. Meek, D. J. Strasser, C. He, D. M. Knauss, W. E. Mustain, S. Pylypenko, B. S. Pivovar, *J. Electrochem. Soc.* **2021**, *168*, 044525.

[112] A. G. Wright, J. Fan, B. Britton, T. Weissbach, H.-F. Lee, E. A. Kitching, T. J. Peckham, S. Holdcroft, *Energy Environ. Sci.* **2016**, *9*, 2130.

[113] M. G. Marino, K. D. Kreuer, *ChemSusChem* **2015**, *8*, 513.

[114] N. Chen, Y. Jin, H. Liu, C. Hu, B. Wu, S. Xu, H. Li, J. Fan, Y. M. Lee, *Angew. Chem., Int. Ed.* **2021**, *60*, 19272.

[115] T. H. Pham, A. Allushi, J. S. Olsson, P. Jannasch, *Polym. Chem.* **2020**, *11*, 6953.

[116] a) M. Zeng, X. He, J. Wen, G. Zhang, H. Zhang, H. Feng, H. Qian, M. Li, *Adv. Mater.* **2023**, *35*, 2306675; b) L. Yin, R. Ren, L. He, W. Zheng, Y. Guo, L. Wang, H. Lee, J. Du, Z. Li, T. Tang, G. Ding, L. Sun, *Angew. Chem., Int. Ed.* **2024**, *63*, 202400764; c) J. Wen, X. He, G. Zhang, M. Zeng, Y. Qian, M. Li, *Sci. China Mater.* **2024**, *67*, 965; d) H. Zhang, X. He, H. Feng, C. Li, M. Li, *J. Mater. Chem. A* **2024**, *12*, 23570.

[117] W. You, K. M. Hugar, R. C. Selhorst, M. Treichel, C. R. Peltier, K. J. T. Noonan, G. W. Coates, *J. Org. Chem.* **2021**, *86*, 254.

[118] a) L. Li, J. Wang, M. Hussain, L. Ma, N. A. Qaisrani, S. Ma, L. Bai, X. Yan, X. Deng, G. He, F. Zhang, *J. Membr. Sci.* **2021**, *624*, 119088; b) N. A. Qaisrani, L. Ma, M. Hussain, J. Liu, L. Li, R. Zhou, Y. Jia, F. Zhang, G. He, *ACS Appl. Mater. Interfaces* **2020**, *12*, 3510; c) S. S. Patil, M. V., I. Kammakakam, M. H. H. Swamy, K. S. Patil, Z. Lai, A. Rao H N, *Electrochim. Acta* **2022**, *426*, 140826.

[119] a) H.-S. Dang, P. Jannasch, *J. Mater. Chem. A* **2016**, *4*, 17138; b) H.-S. Dang, P. Jannasch, *Macromolecules* **2015**, *48*, 5742.

[120] Q. Wei, X. Cao, P. Veh, A. Konovalova, P. Mardle, P. Overton, S. Cassegrain, S. Vierrath, M. Breitwieser, S. Holdcroft, *Sustain. Energy Fuels* **2022**, *6*, 3551.

[121] W. Yu, J. Zhang, X. Liang, X. Ge, C. Wei, Z. Ge, K. Zhang, G. Li, W. Song, M. A. Shehzad, L. Wu, T. Xu, *J. Membr. Sci.* **2021**, *634*, 119404.

[122] J. Fan, A. G. Wright, B. Britton, T. Weissbach, T. J. G. Skalski, J. Ward, T. J. Peckham, S. Holdcroft, *ACS Macro Lett.* **2017**, *6*, 1089.

[123] B. Lin, F. Xu, Y. Su, J. Han, Z. Zhu, F. Chu, Y. Ren, L. Zhu, J. Ding, *ACS Appl. Energy Mater.* **2020**, *3*, 1089.

[124] A. M. A. Mahmoud, K. Yoshimura, Y. Maekawa, *J. Membr. Sci.* **2021**, *620*, 118844.

[125] J. Fan, S. Willdorf-Cohen, E. M. Schibli, Z. Paula, W. Li, T. J. G. Skalski, A. T. Sergeenko, A. Hohenadel, B. J. Frisken, E. Magliocca, W. E. Mustain, C. E. Diesendruck, D. R. Dekel, S. Holdcroft, *Nat. Commun.* **2019**, *10*, 2306.

[126] a) K. M. Hugar, H. A. I. V. Kostalik, G. W. Coates, *J. Am. Chem. Soc.* **2015**, *137*, 8730; b) B. Lin, H. Dong, Y. Li, Z. Si, F. Gu, F. Yan, *Chem. Mat.* **2013**, *25*, 1858; c) K. M. Meek, Y. A. Elabd, *Macromolecules* **2015**, *48*, 7071.

[127] a) K. M. Hugar, W. You, G. W. Coates, *ACS Energy Lett.* **2019**, *4*, 1681; b) M. J. Pellerite, M. M. Kaplun, R. J. Webb, *J. Org. Chem.* **2019**, *84*, 15486.

[128] a) F. Gu, H. Dong, Y. Li, Z. Si, F. Yan, *Macromolecules* **2014**, *47*, 208; b) T. Weissbach, A. G. Wright, T. J. Peckham, A. Sadeghi Alavijeh, V. Pan, E. Kjeang, S. Holdcroft, *Chem. Mat.* **2016**, *28*, 8060.

[129] W. You, K. J. T. Noonan, G. W. Coates, *Prog. Polym. Sci.* **2020**, *100*, 101177.

[130] a) K. Yang, X. Chu, X. Zhang, X. Li, J. Zheng, S. Li, N. Li, T. A. Sherazi, S. Zhang, *J. Membr. Sci.* **2020**, *603*, 118025; b) H. Ono, T. Kimura, A. Takano, K. Asazawa, J. Miyake, J. Inukai, K. Miyatake, *J. Mater. Chem. A* **2017**, *5*, 24804.

[131] a) W. H. Lee, A. D. Mohanty, C. Bae, *ACS Macro Lett.* **2015**, *4*, 453; b) S. Miyanishi, T. Yamaguchi, *J. Mater. Chem. A* **2019**, *7*, 2219; c) T. H. Pham, J. S. Olsson, P. Jannasch, *J. Mater. Chem. A* **2019**, *7*, 15895.

[132] F. Xu, Y. Chen, B. Lin, J. Li, K. Qiu, J. Ding, *ACS Macro Lett.* **2021**, *10*, 1180.

[133] H. Zhang, W. Song, L. Sun, C. Yang, X. Zhang, M. Wu, L. Wu, X. Ge, T. Xu, *Membranes* **2024**, *14*, 121.

[134] a) H. Ono, J. Miyake, S. Shimada, M. Uchida, K. Miyatake, *J. Mater. Chem. A* **2015**, *3*, 21779; b) H. Ono, J. Miyake, K. Miyatake, *J. Polym. Sci. A Polym. Chem.* **2017**, *55*, 1442; c) A. M. A. Mahmoud, A. M. M. Elsaghier, K. Otsuji, K. Miyatake, *Macromolecules* **2017**, *50*, 4256; d) J. Miyake, K. Miyatake, *Sustain. Energy Fuels* **2019**, *3*. e) D. Koronka, A. Matsumoto, K. Otsuji, K. Miyatake, *RSC Adv.* **2019**, *9*, 37391; f) T. Kimura, A. Matsumoto, J. Inukai, K. Miyatake, *ACS Appl. Energy Mater.* **2019**, *3*, 469; g) A. M. Ahmed Mahmoud, K. Miyatake, *J. Mater. Chem. A* **2018**, *6*, 14400; h) A. M. Ahmed Mahmoud, K. Miyatake, *J. Membr. Sci.* **2022**, *643*, 120072.

[135] a) J. Varcoe, R. Slade, *Electrochem. Commun.* **2006**, *8*, 839; b) S. D. Poynton, J. R. Varcoe, *Solid State Ion* **2015**, *277*, 38; c) J. Ponce-González, D. K. Whelligan, L. Wang, R. Bance-Soualhi, Y. Wang, Y. Peng, H. Peng, D. C. Apperley, H. N. Sarode, T. P. Pandey, A. G. Divekar, S. Seifert, A. M. Herring, L. Zhuang, J. R. Varcoe, *Energy Environ. Sci.* **2016**, *9*, 3724; d) L. Wang, J. J. Brink, Y. Liu, A. M. Herring, J. Ponce-González, D. K. Whelligan, J. R. Varcoe, *Energy Environ. Sci.* **2017**, *10*, 2154; e) J. Ponce-González, I. Ouachan, J. R. Varcoe, D. K. Whelligan, *J. Mater. Chem. A* **2018**, *6*, 823; f) L. Wang, E. Magliocca, E. L. Cunningham, W. E. Mustain, S. D. Poynton, R. Escudero-Cid, M. M. Nasef, J. Ponce-González, R. Bance-Souahli, R. C. T. Slade, D. K. Whelligan, J. R. Varcoe, *Green Chem.* **2017**, *19*, 831; g) L. Wang, M. Bellini, H. A. Miller, J. R. Varcoe, *J. Mater. Chem. A* **2018**, *6*, 15404.

[136] a) L. Zhu, X. Yu, X. Peng, T. J. Zimudzi, N. Saikia, M. T. Kwasny, S. Song, D. I. Kushner, Z. Fu, G. N. Tew, W. E. Mustain, M. A. Yandrasits, M. A. Hickner, *Macromolecules* **2019**, *52*, 4030; b) M. Zhang, J. Liu, Y. Wang, L. An, M. D. Guiver, N. Li, *J. Mater. Chem. A* **2015**, *3*, 12284; c) M. Zhang, C. Shan, L. Liu, J. Liao, Q. Chen, M. Zhu, Y. Wang, L. An, N. Li, *ACS Appl. Mater. Interfaces* **2016**, *8*, 23321.

[137] a) W. You, E. Padgett, S. N. MacMillan, D. A. Muller, G. W. Coates, *Proc. Natl. Acad. Sci. U.S.A* **2019**, *116*, 9729; b) W. You, J. M. Ganley, B. G. Ernst, C. R. Peltier, H.-Y. Ko, R. A. DiStasio, R. R. Knowles, G. W. Coates, *Chem. Sci.* **2021**, *12*, 3898; c) H. Chen, K.-T. Bang, Y. Tian, C. Hu, R. Tao, Y. Yuan, R. Wang, D.-M. Shin, M. Shao, Y. M. Lee, Y. Kim, *Angew. Chem., Int. Ed.* **2023**, *62*, 202307690; d) C. R. Peltier, W. You, D. Fackovic Volcanjk, Q. Li, A. J. Macbeth, H. D. Abruña, G. W. Coates, *ACS Energy Lett.* **2023**, *8*, 2365; e) H. A. I. V. Kostalik, T. J. Clark, N. J. Robertson, P. F. Mutolo, J. M. Longo, H. D. Abruña, G. W. Coates, *Macromolecules* **2010**, *43*, 7147.

[138] a) W. Chen, M. Mandal, G. Huang, X. Wu, G. He, P. A. Kohl, *ACS Appl. Energy Mater.* **2019**, *2*, 2458; b) X. He, C. Cheng, S. Huang, F.

**ADVANCED
SCIENCE NEWS**

www.advancedsciencenews.com

**ADVANCED
MATERIALS**

www.advmat.de

Zhang, Y. Duan, C. Zhu, Y. Guo, K. Wang, D. Chen, *Polymer* **2020**, *195*, 122412; c) C. Wang, B. Mo, Z. He, Q. Shao, D. Pan, E. Wujick, J. Guo, X. Xie, X. Xie, Z. Guo, *J. Membr. Sci.* **2018**, *556*, 118.

[139] a) M. Mandal, G. Huang, P. A. Kohl, *J. Membr. Sci.* **2019**, *570–571*, 394; b) M. Mandal, G. Huang, P. A. Kohl, *ACS Appl. Energy Mater.* **2019**, *2*, 2447; c) M. Mandal, G. Huang, N. U. Hassan, W. E. Mustain, P. A. Kohl, *J. Mater. Chem. A* **2020**, *8*, 17568; d) D.-G. Kim, T. Takigawa, T. Kashino, O. Burtovyy, A. Bell, R. A. Register, *Chem. Mat.* **2015**, *27*, 6791.

[140] L. Zeng, Q. He, Y. Liao, S. Kuang, J. Wang, W. Ding, Q. Liao, Z. Wei, *Research* **2020**, *2020*, 4794706.

[141] L. Zeng, Y. Liao, J. Wang, Z. Wei, *J. Power Sources* **2021**, *486*, 229377.

[142] W. Yuan, L. Zeng, Y. Li, J. Wang, X. Wang, Q. Liao, L. Li, Z. Wei, *Small* **2022**, *18*, 2105691.

[143] a) J. Y. Jeon, S. Park, J. Han, S. Maurya, A. D. Mohanty, D. Tian, N. Saikia, M. A. Hickner, C. Y. Ryu, M. E. Tuckerman, S. J. Paddison, Y. S. Kim, C. Bae, *Macromolecules* **2019**, *52*, 2139; b) A. D. Mohanty, C. Y. Ryu, Y. S. Kim, C. Bae, *Macromolecules* **2015**, *48*, 7085; c) X. Gao, H. Yu, J. Jia, J. Hao, F. Xie, J. Chi, B. Qin, L. Fu, W. Song, Z. Shao, *RSC Adv.* **2017**, *7*, 19153; d) J. Hao, X. Gao, Y. Jiang, H. Zhang, J. Luo, Z. Shao, B. Yi, *J. Membr. Sci.* **2018**, *551*, 66.

[144] a) Y. Shi, Z. Zhao, W. Liu, C. Zhang, *Energy Fuels* **2020**, *34*, 16746; b) J. Huang, Y. Liang, R. Cai, X. Wei, U. Wahid, Z. Zhao, W. Liu, C. Zhang, *J. Power Sources* **2024**, *613*, 234853.

[145] X. Gao, H. Yu, F. Xie, J. Hao, Z. Shao, *Sustain. Energy Fuels* **2020**, *4*, 4057.

[146] a) Y. Ye, S. Sharick, E. M. Davis, K. I. Winey, Y. A. Elabd, *ACS Macro Lett.* **2013**, *2*, 575; b) M. Tanaka, K. Fukasawa, E. Nishino, S. Yamaguchi, K. Yamada, H. Tanaka, B. Bae, K. Miyatake, M. Watanabe, *J. Am. Chem. Soc.* **2011**, *133*, 10646; c) Y. Kim, Y. Wang, A. France-Lanord, Y. Wang, Y.-C. M. Wu, S. Lin, Y. Li, J. C. Grossman, T. M. Swager, *J. Am. Chem. Soc.* **2019**, *141*, 18152.

[147] G. Huang, M. Mandal, X. Peng, A. C. Yang-Neyerlin, B. S. Pivovar, W. E. Mustain, P. A. Kohl, *J. Electrochem. Soc.* **2019**, *166*, F637.

[148] a) Y. Wu, C. Wu, J. R. Varcoe, S. D. Poynton, T. Xu, Y. Fu, *J. Power Sources* **2010**, *195*, 3069; b) C.-C. Yang, S.-J. Chiu, W.-C. Chien, S.-S. Chiu, *J. Power Sources* **2010**, *195*, 2212; c) X. Li, Y. Yu, Y. Meng, *ACS Appl. Mater. Interfaces* **2013**, *5*, 1414; d) X. Liao, L. Ren, D. Chen, X. Liu, H. Zhang, *J. Power Sources* **2015**, *286*, 258; e) Y. Chu, Y. Chen, N. Chen, F. Wang, H. Zhu, *RSC Adv.* **2016**, *6*, 96768; f) B. Shi, Y. Li, H. Zhang, W. Wu, R. Ding, J. Dang, J. Wang, *J. Membr. Sci.* **2016**, *498*, 242; g) C. Gong, S. Zhao, W.-C. Tsen, F. Hu, F. Zhong, B. Zhang, H. Liu, G. Zheng, C. Qin, S. Wen, *J. Power Sources* **2019**, *441*, 227176; h) R. Narducci, E. Sgreccia, P. Knauth, M. L. Di Vona, *Polymers* **2021**, *13*, 3887.

[149] A. L. Clemens, B. S. Jayathilake, J. J. Karnes, J. J. Schwartz, S. E. Baker, E. B. Duoss, J. S. Oakdale, *Polymers* **2023**, *15*, 1534.

[150] Y. Liu, J. Zhou, J. Hou, Z. Yang, T. Xu, *ACS Appl. Polym. Mater.* **2018**, *1*, 76.

[151] a) L. Bai, L. Ma, L. Li, A. Zhang, X. Yan, F. Zhang, G. He, *ACS Appl. Energy Mater.* **2021**, *4*, 6957; b) X. Wu, N. Chen, H. A. Klok, Y. M. Lee, X. Hu, *Angew. Chem., Int. Ed.* **2022**, *61*, 202114892; c) L. Li, T. Jiang, S. Wang, S. Cheng, X. Li, H. Wei, Y. Ding, *ACS Appl. Energy Mater.* **2022**, *5*, 2462.

[152] Z. Yang, R. Guo, R. Malpass-Evans, M. Carta, N. B. McKeown, M. D. Guiver, L. Wu, T. Xu, *Angew. Chem., Int. Ed.* **2016**, *55*, 11499.

[153] a) S. Holdcroft, *Chem. Mat.* **2014**, *26*, 381; b) J. Peron, Z. Shi, S. Holdcroft, *Energy Environ. Sci.* **2011**, *4*, 1575.

[154] a) A. J. Steinbach, J. S. Allen, R. L. Borup, D. S. Hussey, D. L. Jacobson, A. Komlev, A. Kwong, J. MacDonald, R. Mukundan, M. J. Pejsa, M. Roos, A. D. Santamaria, J. M. Sieracki, D. Spernjak, I. V. Zenyuk, A. Z. Weber, *Joule* **2018**, *2*, 1297; b) G. S. Hwang, H. Kim, R. Lujan, R. Mukundan, D. Spernjak, R. L. Borup, M. Kaviany, M. H.

Kim, A. Z. Weber, *Electrochim. Acta* **2013**, *95*, 29; c) S. Favero, I. E. L. Stephens, M.-M. Titirci, *Adv. Mater.* **2024**, *36*, 2308238.

[155] A. M. Park, Z. R. Owczarczyk, L. E. Garner, A. C. Yang-Neyerlin, H. Long, C. M. Antunes, M. R. Sturgeon, M. J. Lindell, S. J. Hamrock, M. Yandrasits, B. S. Pivovar, *ECS Trans.* **2017**, *80*, 957.

[156] S. Gu, R. Cai, T. Luo, Z. Chen, M. Sun, Y. Liu, G. He, Y. Yan, *Angew. Chem., Int. Ed.* **2009**, *48*, 6499.

[157] A. L. Gonçalves Biancolli, D. Herranz, L. Wang, G. Stehlíková, R. Bance-Soualhi, J. Ponce-González, P. Ocón, E. A. Ticianelli, D. K. Whelligan, J. R. Varcoe, E. I. Santiago, *J. Mater. Chem. A* **2018**, *6*, 24330.

[158] a) D. Li, H. T. Chung, S. Maurya, I. Matanovic, Y. S. Kim, *Curr. Opin. Electrochem.* **2018**, *12*, 189; b) R. Chenitz, U. I. Kramm, M. Lefèvre, V. Glibin, G. Zhang, S. Sun, J.-P. Dodelet, *Energy Environ. Sci.* **2018**, *11*, 365; c) S. Maurya, J. H. Dumont, C. N. Villarrubia, I. Matanovic, D. Li, Y. S. Kim, S. Noh, J. Han, C. Bae, H. A. Miller, C. H. Fujimoto, D. R. Dekel, *ACS Catal.* **2018**, *8*, 9429; d) S. Maurya, S. Noh, I. Matanovic, E. J. Park, C. Narvaez Villarrubia, U. Martinez, J. Han, C. Bae, Y. S. Kim, *Energy Environ. Sci.* **2018**, *11*, 3283; e) I. Matanovic, S. Maurya, E. J. Park, J. Y. Jeon, C. Bae, Y. S. Kim, *Chem. Mat.* **2019**, *31*, 4195; f) D. P. Leonard, M. Lehmann, J. M. Klein, I. Matanovic, C. Fujimoto, T. Saito, Y. S. Kim, *Adv. Energy Mater.* **2023**, *13*, 2203488.

[159] I. Matanovic, H. T. Chung, Y. S. Kim, *J. Phys. Chem. Lett.* **2017**, *8*, 4918.

[160] a) X. Liang, M. A. Shehzad, Y. Zhu, L. Wang, X. Ge, J. Zhang, Z. Yang, L. Wu, J. R. Varcoe, T. Xu, *Chem. Mat.* **2019**, *31*, 7812; b) C. Hu, H. W. Kang, S. W. Jung, X. Zhang, Y. J. Lee, N. Y. Kang, C. H. Park, Y. M. Lee, *ACS Cent. Sci.* **2024**, *10*, 603.

[161] S. Turan, S. Park, C. Y. Ryu, D. Y. Ryu, C. Bae, *J. Membr. Sci.* **2024**, *700*, 122662.

[162] a) L. Zeng, T. S. Zhao, L. An, G. Zhao, X. H. Yan, *Energy Environ. Sci.* **2015**, *8*, 2768; b) N. Chen, C. Long, Y. Li, D. Wang, H. Zhu, *J. Membr. Sci.* **2018**, *552*, 51.

[163] J. Fan, H. Zhu, R. Li, N. Chen, K. Han, *J. Mater. Chem. A* **2014**, *2*, 8376.

[164] a) N. Chen, D. Wang, C. Long, Y. Li, C. Lu, F. Wang, H. Zhu, *Nanoscale* **2018**, *10*, 18680; b) X. Liu, N. Xie, J. Xue, M. Li, C. Zheng, J. Zhang, Y. Qin, Y. Yin, D. R. Dekel, M. D. Guiver, *Nat. Energy* **2022**, *7*, 329.

[165] T. Wang, L. Shi, J. Wang, Y. Zhao, B. P. Setzler, S. Rojas-Carbonell, Y. Yan, *J. Electrochem. Soc.* **2019**, *166*, F3305.

[166] a) R. B. Kaspar, Y. Yan, *J. Electrochem. Soc.* **2016**, *163*, F593; b) T. J. Omasta, Y. Zhang, A. M. Park, X. Peng, B. Pivovar, J. R. Varcoe, W. E. Mustain, *J. Electrochem. Soc.* **2018**, *165*, F710.

[167] F. Li, S. H. Chan, Z. Tu, *Chem. Rec.* **2024**, *24*, 202300067.

[168] J. Fan, M. Chen, Z. Zhao, Z. Zhang, S. Ye, S. Xu, H. Wang, H. Li, *Nat. Energy* **2021**, *6*, 475.

[169] a) G. Li, Y. Wang, J. Pan, J. Han, Q. Liu, X. Li, P. Li, C. Chen, L. Xiao, J. Lu, L. Zhuang, *Int. J. Hydrog. Energy* **2015**, *40*, 6655; b) M. R. Gerhardt, L. M. Pant, A. Z. Weber, *J. Electrochem. Soc.* **2019**, *166*, F3180; c) A. M. Kiss, T. D. Myles, K. N. Grew, A. A. Peracchio, G. J. Nelson, W. K. S. Chiu, *J. Electrochem. Soc.* **2013**, *160*, F994; d) J. A. Wrubel, A. A. Peracchio, B. N. Cassenti, T. J. Omasta, W. E. Mustain, K. N. Grew, W. K. S. Chiu, *J. Electrochem. Soc.* **2019**, *166*, F1047; e) A. G. Divekar, A. C. Yang-Neyerlin, C. M. Antunes, D. J. Strasser, A. R. Motz, S. S. Seifert, X. Zuo, B. S. Pivovar, A. M. Herring, *Sustain. Energy Fuels* **2020**, *4*, 1801.

[170] D. R. Dekel, M. Amar, S. Willdorf, M. Kosa, S. Dhara, C. E. Diesendruck, *Chem. Mat.* **2017**, *29*, 4425.

[171] J. Zhang, W. Zhu, T. Huang, C. Zheng, Y. Pei, G. Shen, Z. Nie, D. Xiao, Y. Yin, M. D. Guiver, *Adv. Sci.* **2021**, *8*, 2100284.

[172] a) A. C. Bhosale, P. C. Ghosh, L. Assaud, *Renew. Sust. Energy Rev.* **2020**, *133*, 110286; b) S. Mo, L. Du, Z. Huang, J. Chen, Y. Zhou, P.

Wu, L. Meng, N. Wang, L. Xing, M. Zhao, Y. Yang, J. Tang, Y. Zou, S. Ye, *Electrochem. Energy Rev.* **2023**, *6*, 28.

[173] J. Eon Chae, J. Choi, S. Lee, C. Park, S. Kim, *J. Ind. Eng. Chem.* **2024**, *133*, 255.

[174] a) A. Carlson, P. Shapturenka, B. Eriksson, G. Lindbergh, C. Lagergren, R. W Lindström, *Electrochim. Acta* **2018**, *277*, 151; b) Z. Turtayeva, F. Xu, J. Dillet, K. Mozet, R. Peignier, A. Celzard, G. Maranzana, *Heliyon* **2024**, e29622; c) S. Kim, M. Her, Y. Kim, C.-Y. Ahn, S. Park, Y.-H. Cho, Y.-E. Sung, *Electrochim. Acta* **2021**, *400*, 139439.

[175] R. B. Kaspar, M. P. Letterio, J. A. Wittkopf, K. Gong, S. Gu, Y. Yan, *J. Electrochem. Soc.* **2015**, *162*, F483.

[176] a) J. Hyun, J. Y. Jeon, G. Doo, J. Jung, S. Choi, D.-H. Lee, D. W. Lee, J. Kwen, W. Jo, C. Bae, H.-T. Kim, *Chem. Eng. J.* **2022**, *427*, 131737; b) A. Orfanidi, P. J. Rheinländer, N. Schulte, H. A. Gasteiger, *J. Electrochem. Soc.* **2018**, *165*, F1254.

[177] L. Shi, B. P. Setzler, K. Hu, C. M. Weiss, S. Matz, Y. Xue, Z. Xu, Z. Zhuang, S. Gottesfeld, Y. Yan, *J. Electrochem. Soc.* **2020**, *167*, 144506.

[178] X. Peng, D. Kulkarni, Y. Huang, T. J. Omasta, B. Ng, Y. Zheng, L. Wang, J. M. LaManna, D. S. Hussey, J. R. Varcoe, I. V. Zenyuk, W. E. Mustain, *Nat. Commun.* **2020**, *11*, 3561.

[179] a) S. Chempath, B. R. Einsla, L. R. Pratt, C. S. Macomber, J. M. Boncella, J. A. Rau, B. S. Pivovar, *J. Phys. Chem. C* **2008**, *112*, 3179; b) S. Chempath, J. M. Boncella, L. R. Pratt, N. Henson, B. S. Pivovar, *J. Phys. Chem. C* **2010**, *114*, 11977;

[180] M. Hu, Q. Li, H. Peng, H. Ma, L. Xiao, G. Wang, J. Lu, L. Zhuang, *J. Power Sources* **2020**, *472*, 228471.

[181] T. H. Wan, M. Saccoccio, C. Chen, F. Ciucci, *Electrochim. Acta* **2015**, *184*, 483.

[182] T. Kimura, Y. Yamazaki, *Electrochemistry* **2011**, *79*, 94.

[183] a) M. E. Tuckerman, D. Marx, M. Parrinello, *Nature* **2002**, *417*, 925; b) K. N. Grew, W. K. S. Chiu, *J. Electrochem. Soc.* **2010**, *157*, B327.

[184] a) M. Inaba, Y. Matsui, M. Saito, A. Tasaka, K. Fukuta, S. Watanabe, H. Yanagi, *Electrochemistry* **2011**, *79*, 322; b) U. Krewer, C. Weinzierl, N. Ziv, D. R. Dekel, *Electrochim. Acta* **2018**, *263*, 433; c) Y. Wang, L. Li, L. Hu, L. Zhuang, J. Lu, B. Xu, *Electrochem. Commun.* **2003**, *5*, 662.

[185] a) Y. Wang, B. Seo, B. Wang, N. Zamel, K. Jiao, X. C. Adroher, *Energy AI* **2020**, *1*, 100014; b) R. Ding, R. Wang, Y. Ding, W. Yin, Y. Liu, J. Li, J. Liu, *Angew. Chem., Int. Ed.* **2020**, *59*, 19175.
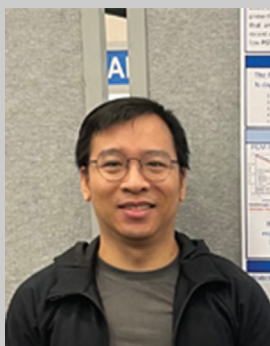
Huiyu Lei obtained his Master's degree in physical chemistry from South China University of Technology in 2019. He is currently a Ph.D. candidate in Prof. Shuhui Sun's group at the Institute National de la recherche Scientifique – Centre Énergie Matériaux Télécommunications (INRS-EMT), Varennes, Canada. His research interests focus on advanced electrocatalysts, atomic layer deposition, proton exchange membrane fuel cells, and anion exchange membrane fuel cells.

Gaixia Zhang is a Marcelle Gauvreau Engineering Research Chair Professor at École de Technologie Supérieure (ÉTS), University of Québec, Montréal, Canada. She received her Ph.D. degree from Polytechnique Montréal and then continued her research at Western University and INRS, Canada. Her research interests focus on advanced materials (catalysts, electrodes, and electrolytes) for sustainable energy conversion and storage applications, including batteries, fuel cells, hydrogen production, and CO_2 reduction. She is also interested in interface and device engineering, as well as *in-situ* characterizations and theoretical simulations.

ADVANCED
SCIENCE NEWS

www.advancedsciencenews.com

ADVANCED
MATERIALS

www.advmat.de

Ana C. Tavares is a Full Professor at Institute National de la recherche Scientifique – Centre Énergie Matériaux Télécommunications (INRS-EMT), Varennes, Canada. Her research interests cover the development of electrocatalysts for fuel cells and electrolyzes, as well as functional materials for electrochemical sensors.

Shuhui Sun is a Full Professor at Institute National de la recherche Scientifique – Centre Énergie Matériaux Télécommunications (INRS-EMT), Varennes, Canada. He is a Fellow of the Royal Society of Canada (FRSC), and a Fellow of the Canadian Academy of Engineering (FCAE). His current research interests focus on multifunctional nanomaterials for energy conversion and storage applications, including fuel cells, metal-ion (Li^+, Na^+, Zn^{2+}) batteries, lithium metal batteries, metal-air batteries, solid-state batteries, etc. He is also interested in nanostructured photo- and electro-catalysts for H_2 production, CO_2 reduction, and water treatment.